


Fall 11-17-2018

Nanoparticle Catalytic Enhancement of Carbon Dioxide Reforming of Methane for Hydrogen Production

Nicholas Groden

Follow this and additional works at: <https://digitalcommons.latech.edu/dissertations>

 Part of the [Nanoscience and Nanotechnology Commons](#), [Other Chemical Engineering Commons](#), and the [Other Materials Science and Engineering Commons](#)

Recommended Citation

Groden, Nicholas, "" (2018). *Dissertation*. 3.
<https://digitalcommons.latech.edu/dissertations/3>

This Dissertation is brought to you for free and open access by the Graduate School at Louisiana Tech Digital Commons. It has been accepted for inclusion in Doctoral Dissertations by an authorized administrator of Louisiana Tech Digital Commons.

**NANOPARTICLE CATALYTIC ENHANCEMENT OF CARBON
DIOXIDE REFORMING OF METHANE FOR
HYDROGEN PRODUCTION**

by

Nicholas Groden, M.S., B.S.

A Dissertation Presented in Partial Fulfillment
of the Requirements of the Degree
Doctor of Philosophy

COLLEGE OF ENGINEERING AND SCIENCE
LOUISIANA TECH UNIVERSITY

November 2018

LOUISIANA TECH UNIVERSITY
THE GRADUATE SCHOOL

JUNE 16, 2018

Date

We hereby recommend that the dissertation prepared under our supervision by
Nicholas Groden, M.S., B.S.

entitled **Nanoparticle Catalytic Enhancement of Carbon Dioxide Reforming of
Carbon Dioxide Reforming of Methane for Hydrogen Production**

be accepted in partial fulfillment of the requirements for the Degree of
Doctor of Philosophy in Engineering Micro and Nanoscale Systems

Supervisor of Dissertation Research

Head of Department

Department

Recommendation concurred in:

Advisory Committee

Approved:

Approved:

Director of Graduate Studies

Dean of the Graduate School

Dean of the College

ABSTRACT

The U.S. produces 5559.6 million metric tons of carbon dioxide annually, of which 21% is produced by industrial processes. Steam reforming, an industrial process that accounts for 95% of all hydrogen production in industry, produces 134.5 million metric tons of carbon dioxide or around 11% of the total carbon dioxide produced by industry. This carbon dioxide is then either emitted or goes through a sequestration process that accounts for 75% of the plant's operational costs. An alternative reaction to steam reforming is dry reforming, which utilizes carbon dioxide rather than emitting it and can be used in conjunction with current steam reforming to remove costs associated with sequestration. Dry reforming is not used in industry due to its higher energy requirements and lower catalyst life due to carbon deposition. To reduce energy requirements and extend the life of the dry reforming catalyst, nanostructured heterogeneous metals and ceramics made from an electrospinning process and graphene nanoscrolls made through a bulk electrochemical method are proposed as a catalyst and highly sensitive chemiresistive sensors to monitor precise gas quantities within the reaction without the need for extra energy supplied to them.

This dissertation explores the use of nanostructured heterogeneous metals and nonmetals as more resilient catalysts and supports for the dry reforming technique. To reduce the energy required for dry reforming, catalysts were fabricated through an electrospinning process and used nickel as the primary catalyst due to its high activity and

low cost. Iron was used within the nanofibers to create a redox side reaction to decrease the solid carbon formation on the surface of the catalysts showing higher reactivity after 15 hours of reaction. Electrospun magnesium aluminate spinels ceramics were studied as a support and found to have excellent stability and reactivity, achieving an 83% lower apparent activation energy than nickel catalysts alone. To reduce coking on the surface of the catalyst, graphene nanoscrolls were fabricated using a scalable electrochemical exfoliation technique and used as supports in the dry reforming reaction to nickel nanoparticles. They were found to have similar properties to carbon nanotube supports reported in previous literature and a 30% lower coking amount than traditional nickel catalysts after 15 hours and 12% lower apparent activation energy than traditional nickel catalysts. Finally, to be able to precisely monitor gas evolution, the electrospun metal nanofibers and graphene nanoscrolls were used as sensing elements in a polyaniline doped gas sensor. These sensors were tested at room temperature with methane, ethanol gas and acetone gas and found to have responses over 100% higher than polyaniline alone. Combined, catalytic nanofibers and graphene nanoscroll supports have been shown to lower the apparent activation energy requirements and resist carbon deposition induced deactivation on the catalyst while allowing for a passive sensing material, offering a pathway forward towards an economically viable dry reforming process.

APPROVAL FOR SCHOLARLY DISSEMINATION

The author grants to the Prescott Memorial Library of Louisiana Tech University the right to reproduce, by appropriate methods, upon request, any or all portions of this Dissertation. It is understood that “proper request” consists of the agreement, on the part of the requesting party, that said reproduction is for his personal use and that subsequent reproduction will not occur without written approval of the author of this Dissertation. Further, any portions of the Dissertation used in books, papers, and other works must be appropriately referenced to this Dissertation.

Finally, the author of this Dissertation reserves the right to publish freely, in the literature, at any time, any or all portions of this Dissertation.

Author _____

Date _____

DEDICATION

For my grandparents, who helped set me on this path, and my parents, who saw me through.

TABLE OF CONTENTS

ABSTRACT.....	iii
DEDICATION.....	vi
LIST OF TABLES.....	x
LIST OF FIGURES.....	xii
ACKNOWLEDGMENTS.....	xviii
CHAPTER 1 INTRODUCTION.....	1
1.1 Introduction.....	1
1.1.1 Motivation for Research.....	2
1.1.2 Objectives of Dissertation.....	8
CHAPTER 2 DRY REFORMING REACTION LITERATURE REVIEW.....	10
2.1 Introduction.....	10
2.2 History of Reforming.....	10
2.3 Reforming Reactions.....	14
2.3.1 Methane Reforming.....	15
2.3.2 Steam Reforming.....	16
2.3.3 Partial Oxidation.....	17
2.3.4 Autothermal Reforming.....	18
2.3.5 Dry Reforming.....	18
2.4 Coke Formation.....	22
2.5 Role of Support.....	25
2.6 Role of the Catalytic Material.....	28

2.6.1 Nanostructured Catalysts	31
CHAPTER 3 NANOFIBER METAL CATALYSTS.....	38
3.1 Introduction.....	38
3.2 Nanofiber Catalyst Fabrication.....	39
3.2.1 Electrospinning Theory.....	39
3.2.2 Electrospun Nanofiber Fabrication.....	43
3.3 Characterization of Nanofibers.....	45
3.4 Quantification of Reaction Efficiency	50
3.4.1 Nickel Catalyst Tests	54
3.4.2 Nickel Ferrite Nanofiber Catalyst Testing.....	64
3.4.3 Magnesium Aluminate Spinel Nanofiber Support Tests	82
3.5 Results and Discussion	90
3.6 Summary.....	98
CHAPTER 4 FABRICATION OF ELECTROCHEMICALLY EXFOLIATED GRAPHENE AND GRAPHENE NANOSCROLLS.....	100
4.1 Introduction.....	100
4.2 Graphene Background	101
4.3 Physical Properties of Graphene.....	103
4.4 Electronic Properties of Graphene.....	105
4.5 Edge Structures of Graphene	108
4.6 Graphene Production	113
4.7 Graphene Characterization	119
4.7.1 Graphene NanoSheet XRD Analysis	122
4.8 Graphene Nanoscrolls.....	125
4.8.1 Graphene Nanoscroll XRD Analysis	131
4.8.2 Raman Spectroscopy.....	134

4.8.3	Cyclic Voltammetry.....	137
4.8.4	UV-VIS Analysis	138
4.9	Loaded Graphene Nanoscroll Reactor Testing.....	139
4.10	Summary.....	157
CHAPTER 5 METAL OXIDE NANOFIBER GAS SENSORS.....		159
5.1	Introduction.....	159
5.2	Metal Oxide Gas Sensor Operational Theory.....	160
5.3	Metal Oxide Nanofiber Fabrication	161
5.4	Doped Polyaniline Gas Sensors	166
5.5	Summary.....	185
CHAPTER 6 CONCLUSIONS AND FUTURE WORK.....		186
6.1	Conclusions.....	186
6.2	Future Work.....	190
REFERENCES		192

LIST OF TABLES

Table 1-1: SRES scenarios and their implications for climate change due to CO ₂ emissions. (Produced by IPCC).	5
Table 2-1: Chemical reforming processes and associated energies.	16
Table 2-2: Reactions of dry reforming of methane and their free energies.	20
Table 2-3: Coke formation types.	24
Table 2-4: Catalytic activity per supports and supporting references.....	27
Table 2-5: Noble catalytic metal and supports based on reactant ration, conversion percentage, and temperature by reference.	29
Table 2-6: Noble catalytic metals in the dry reforming reaction based on feed ratio, conversion, and temperature by reference.	30
Table 3-1: Equations describing key properties of electrospun nanofibers.	41
Table 3-2: Apparent activation energies for nickel and nickel-iron.	45
Table 3-3: EDAX elemental distributions pre and post calcination.	50
Table 3-4: Nickel and carbon formation of traditional nickel catalyst on γ -alumina pellet After 3, 9, and 15 hours on stream.	63
Table 3-5: EDAX elemental analysis for nanofiber catalysts with traditional nickel catalyst as a baseline.	91
Table 3-6: Calculated apparent activation energies for the nanofiber catalysts in kJ mol ⁻¹ with traditional nickel catalyst as a baseline for the conversion of methane and the conversion of carbon dioxide.....	97
Table 4-1: Cost breakdown of electrolyte solutions.	115
Table 4-2: GM-10 isostatically pressed very fine grain graphite.....	118
Table 4-3: Elemental analysis of nickel loaded GNS on alumina pellet.	149
Table 4-4: Elemental analysis of GNS/Ni on pellet after 15 hours on stream.....	154

Table 5-1: Operation parameters of electrospinning setup.	162
Table 5-2: Calculated sensitivities for methane.	175
Table 5-3: Calculated sensitivity for acetone.	179
Table 5-4: Calculated sensitivities for ethanol.	182

LIST OF FIGURES

Figure 1-1: Energy production projections in quadrillion BTUs (produced by EIA).	3
Figure 1-2: a.) Energy trade (in quadrillion BTUs) and b.) net energy trade (in quadrillion BTUs) (produced by EIA).....	4
Figure 1-3: Peak oil estimations. (Produced by the DOE)	6
Figure 2-1: Schematic of a Chemical Energy Transmission System (CETS).	13
Figure 2-2: The Energy Transfer “Eva-Adam” process for CETS.....	14
Figure 2-3: Dry reforming reaction of CH ₄ and CO ₂ carried out at standard pressure and increasing temperature performed in GASEQ.	21
Figure 2-4: Gibbs free energy for Boudouard and CH ₄ dehydrogenation reactions.	23
Figure 3-1: 2d schematic of electrospun fiber creation.	40
Figure 3-2: Typical electrospinning setup.	44
Figure 3-3: Pre-calcination disordered nanofibers.....	46
Figure 3-4: Post-calcination nanofibers with diameters shown in nanometers.	47
Figure 3-5: Nanofiber distributions before calcination.....	48
Figure 3-6: Nanofiber distributions after calcination.	48
Figure 3-7: EDAX elemental analysis graph of pre-calcination nanofibers.....	49
Figure 3-8: EDAX elemental analysis graph of post-calcination nanofibers.	50
Figure 3-9: Schematic of reaction space with the GC system.	51
Figure 3-10: Thermal plug flow reactor (GSL-1500X MTI Corp.) with in-line GC (SRI 8610C, SRI Corp).....	51
Figure 3-11: Gas evolution over traditional Ni catalyst at 700 °C.	55

Figure 3-12: Gas evolution over traditional Ni catalyst at 800 °C.	56
Figure 3-13: Gas evolution over traditional Ni catalyst at 900 °C.	57
Figure 3-14: SEM of traditional Ni catalyst after 3 hours on stream with a.) nickel particles and b.) coke formation.....	58
Figure 3-15: EDAX of traditional nickel catalyst after 3 hours on stream.....	59
Figure 3-16: Traditional nickel catalyst after 9 hours showing carbide formation.	60
Figure 3-17: EDAX of traditional Ni catalyst after 9 hours on stream.....	61
Figure 3-18: SEM of traditional Ni catalyst after 15 hours on stream showing whisker formation.	62
Figure 3-19: EDAX of traditional Ni catalyst after 15 hours on stream.....	63
Figure 3-20: Visual inspection of the traditional nickel catalyst at (a.) 3, (b.) 9 and (c.) 15 hours on stream.....	64
Figure 3-21: Gas evolution over NiFe 2:1 nanofiber catalyst at 700 °C.	65
Figure 3-22: Gas evolution over NiFe 2:1 nanofiber catalyst at 800 °C.	66
Figure 3-23: Gas evolution over NiFe 2:1 nanofiber catalyst at 900 °C.	67
Figure 3-24: Nickel ferrite 1:1 ratio nanofiber catalyst gas evolution at 700 °C.	68
Figure 3-25: Nickel ferrite 1:1 nanofiber catalyst ratio catalyst gas evolution at 800 °C.	69
Figure 3-26: Nickel ferrite nanofiber catalyst 1:1 ratio catalyst gas evolution at 900 °C.	70
Figure 3-27: SEM image of NiFe nanofiber catalyst 2:1 before the reaction showing single nickel ferrite nanofibers and clusters (arrows).	71
Figure 3-28: EDAX analysis of NiFe 2:1 nanofiber catalyst before reaction.	72
Figure 3-29: SEM image of NiFe nanofiber catalyst 2:1 after 9 hours on stream showing nickel carbides (arrows) and clusters of nanofibers (circle).....	73
Figure 3-30: EDAX analysis of NiFe nanofiber catalyst 2:1 after 9 hours on stream....	73
Figure 3-31: SEM image of NiFe nanofiber catalyst 2:1 after 15 hours on stream.....	74
Figure 3-32: EDAX analysis of NiFe nanofiber catalyst 2:1 after 15 hours on stream... 75	75

Figure 3-33: Visual inspection of NiFe 2:1 nanofiber catalyst.....	76
Figure 3-34: SEM imaging of NiFe 1:1 nanofiber catalyst before reaction showing nickel ferrite nanofiber clusters (circles).	77
Figure 3-35: EDAX analysis of NiFe 1:1 nanofiber catalyst before reaction.	77
Figure 3-36: SEM imaging of NiFe 1:1 nanofiber catalyst after 9 hours of reaction showing nickel carbides (arrows) and nanofibers connecting the carbides (circles).....	78
Figure 3-37: EDAX analysis of NiFe 1:1 nanofiber catalyst after 9 hours of reaction. ..	79
Figure 3-38: SEM imaging of NiFe 1:1 nanofiber catalyst after 15 hours of reaction showing nickel carbides (arrows) and nanofiber clumps (circle).	80
Figure 3-39: EDAX analysis of NiFe 1:1 nanofiber catalyst after 15 hours of reaction.....	80
Figure 3-40: Visual inspection of NiFe 1:1 nanofiber catalyst showing samples a.) before reaction, b.) after 9 hours on stream and c.) after 15 hours on stream.	81
Figure 3-41: Gas evolution of MgAl ₂ O ₄ /Ni nanofiber catalyst at 700 °C.....	83
Figure 3-42: Gas evolution of MgAl ₂ O ₄ /Ni nanofiber catalyst at 800 °C.....	84
Figure 3-43: Gas evolution of MgAl ₂ O ₄ /Ni nanofiber catalyst at 900 °C.....	85
Figure 3-44: SEM imaging of MgAl ₂ O ₄ /Ni nanofiber catalyst sample before reaction with nanofiber formation visible.....	86
Figure 3-45: EDAX analysis of MgAl ₂ O ₄ /Ni nanofiber catalyst sample before reaction.....	86
Figure 3-46: SEM imaging of MgAl ₂ O ₄ /Ni nanofiber catalyst sample after 9 hours on stream, showing nickel nanoparticles (arrows).....	87
Figure 3-47: EDAX analysis of MgAl ₂ O ₄ /Ni nanofiber catalyst sample after 9 hours on stream.....	88
Figure 3-48: SEM imaging of MgAl ₂ O ₄ /Ni nanofiber catalyst sample after 15 hours on stream, with a.) graphene bundles and b.) carbon whiskers	89
Figure 3-49: EDAX analysis of MgAl ₂ O ₄ /Ni nanofiber catalyst sample after 15 Hours on stream.	89
Figure 3-50: Visual inspection of MgAl ₂ O ₄ /Ni nanofiber catalyst at a.) before reaction, b.) after 9 hours of reaction and c.) after 15 hours of reaction.....	90

Figure 3-51: Average conversion percentages of methane of the nanofiber catalysts and the traditional nickel catalyst.	93
Figure 3-52: Average carbon dioxide conversion percentages of the nanofiber catalysts and the traditional nickel catalyst.....	93
Figure 3-53: Natural log of rate vs 1/T for methane of the nanofibers catalysts and the traditional nickel catalyst.	96
Figure 3-54: Natural log of rate vs 1/T for carbon dioxide of the nanofiber catalysts and the traditional nickel catalyst.	96
Figure 4-1: Graphene bond structure and lengths.....	104
Figure 4-2: Energy spectrum of resistivity vs. gate voltage, with the Dirac Cone shown as an illustration of the energies as they pass through the structure.....	107
Figure 4-3: Example of zig-zag edge structure on graphene nanoribbon.....	110
Figure 4-4: Example of armchair edge structure on graphene nanoribbon.	111
Figure 4-5: Graphene fabrication electrochemical setup.....	114
Figure 4-6: Graphene formation during the exfoliation process.....	119
Figure 4-7: Single graphene flake imaged via TEM.....	121
Figure 4-8: Graphene flakes produced by electrochemical exfoliation after drying.	122
Figure 4-9: Bragg diffraction model.....	123
Figure 4-10: XRD data collected from lab produced graphene, A0-3 graphene from a third party, and graphite.....	124
Figure 4-11: Dual carbon nanoscroll feedstock production.....	129
Figure 4-12: Morphological analysis with electron spectroscopy.	130
Figure 4-13: XRD analysis showing the crystallinity of the carbon nanostructures from the conversion of graphite to graphene nanosheets to graphene nanoscrolls.....	132
Figure 4-14: XRD comparison of the graphene nanoscrolls with as bought single wall and multi-wall carbon nanotubes.	133
Figure 4-15: Raman spectroscopy of graphene nanosheets.....	135
Figure 4-16: Raman spectra after peak fitting and baseline removal.	136

Figure 4-17: Cyclic voltammetry for a.) 0.1M SDS only, b.) with suspended graphene nanosheets 10V potential, c.) at 17.5V, and d.) at 25V potential.....	138
Figure 4-18: UV-VIS analysis at potentials of 10V, 17.5V, and 25V.....	139
Figure 4-19: Potassium decorated graphene in the process of scrolling.....	140
Figure 4-20: Graphene nanoscroll loaded with potassium nanoparticles.....	141
Figure 4-21: Gas evolution at 700°C for nickel loaded graphene nanoscrolls.....	142
Figure 4-22: Gas evolution at 800°C for nickel loaded graphene nanoscrolls.....	143
Figure 4-23: Gas evolution at 900°C for nickel loaded graphene nanoscrolls.....	144
Figure 4-24: Average methane conversion percentage of select catalysts.....	145
Figure 4-25: Average carbon dioxide conversion percentages for graphene nanoscrolls and other catalysts.....	145
Figure 4-26: Graphene nanoscrolls on the surface of the alumina pellet.....	146
Figure 4-27: EDAX of loaded graphene nanoscroll cluster.....	147
Figure 4-28: EDAX of the area without GNS clusters.....	148
Figure 4-29: SEM of GNS/Ni pellet at 9 hours on stream.....	150
Figure 4-30: EDAX of GNS/Ni pellet after 9 hours on stream.....	151
Figure 4-31: GNS/Ni pellet after 15 hours on stream.....	152
Figure 4-32: EDAX of GNS/Ni pellet after 15 hours on stream.....	153
Figure 4-33: EDAX of GNS/Ni cluster after 15 hours on stream.....	153
Figure 4-34: Visual inspection of pellets (a.) before reaction, (b.) after 9 hours, and (c.) after 15 hours.....	155
Figure 4-35: Natural log of reaction rates of methane.....	156
Figure 4-36: Natural log of reaction rates of carbon dioxide.....	156
Figure 5-1: Model of metal oxide sensor theory.....	160
Figure 5-2: Theoretical wire diameters of different iron oxides.....	163
Figure 5-3: Fiber diameter examples pre- and post- calcination.....	164

Figure 5-4: Experimental-based average fiber diameters of iron oxide nanofibers.	165
Figure 5-5: Operational steps for fabrication of MEMS gas sensor	168
Figure 5-6: MEMS interdigital array, gold on chrome digits are 200 μm wide and spaced 200 μm apart.	170
Figure 5-7: Height measurements of the thin film using the laser confocal microscope.	170
Figure 5-8: 3D height mapping of the sensor/thin film surface using the laser confocal microscope.	171
Figure 5-9: Methane response for nanofibers in PANI sensor.	172
Figure 5-10: Methane response for GNS in PANI sensor.	173
Figure 5-11: Methane response for nanofiber/GNS in PANI sensor.	174
Figure 5-12: Response for acetone on nanofiber in PANI sensor.	177
Figure 5-13: Response for acetone on GNS in PANI sensor.	178
Figure 5-14: Response for acetone on nanofiber and GNS in PANI sensor.	178
Figure 5-15: Response for ethanol on nanofiber sensor.	180
Figure 5-16: Response for ethanol on GNS sensor.	181
Figure 5-17: Response for ethanol on nanofiber/GNS sensor as resistance change.	181
Figure 5-18: Sensitivities of the sensors at different methane concentrations.	183
Figure 5-19: Sensitivities of sensors at different concentrations of acetone.	183
Figure 5-20: Sensitivities of sensors at different concentrations of ethanol.	184

ACKNOWLEDGMENTS

First, I would like to thank my parents and the rest of my family for their continued support of my journey at Louisiana Tech University. They have helped me keep my eyes on the path of graduation even if I myself have strayed once or twice. I would also like to thank my friends for always listening, even if I didn't always make sense and for keeping me sane during the crazy times. Especially to my fiancé Amy Doan, who has been a wonderful source of support during my time finishing my degree.

I'd like to also thank my advisory committee, Dr. Ramu Ramachandran, who was the first person to welcome me to Louisiana Tech University, Dr. James Palmer, whose insight into chemical process helped me think critically about my research and who gave me insight into the inner workings of the college through the graduate studies office, Dr. Randal Null, who helped me find a voice as a student representative of the College of Engineering and Science graduate student body, and Dr. Prabhu Arumugam, who has graciously stepped in at the last minute to help me across the final steps of my degree, and all of whom have given me your time and guidance.

A big thank you to Dr. William Clower, who stayed around the lab many a night working on research with me and has worked with me for countless hours to shape this research. I'd also like to thank the IFM staff Debbie Wood and Davis Bailey for keeping the Institute for Micromanufacturing labs running and providing me with assistance in fabricating testing apparatus. And finally, I'd especially like to thank my advisor, Dr.

Chester Wilson, who has been a source of encouragement for my research and provided me with all the materials and tools I needed for my crazy ideas, and for putting up with me for so long. You have challenged me to become more than just a lab rat.

CHAPTER 1

INTRODUCTION

1.1 Introduction

Synthesis gas, or syngas, is a product gas that is useful intermediate in the chemical processing industry. Stoichiometrically, it is defined as “a mixture of carbon monoxide (~45%), hydrogen gas (~33%) and carbon dioxide (~15%) with other trace gases” [1]. Syngas is primarily produced from methane which makes up 90% of natural gas [2]. Besides accounting for 95% of all hydrogen consumed today, syngas is an important chemical precursor for ammonia-based fertilizers, where it is used as a hydrogen source and fixed to nitrogen to create ammonia [3,4]. It is also used in plastic manufacturing, where syngas is used in methanol, ethylene, and olefin production which are basic building blocks for most polymers today [5]. Additionally, syngas is used as the basis gas for gas-to-liquid (GTL) processes, which use the syngas to create higher-order hydrocarbon chains for use in liquid fuels for automobiles and airplanes [6]. In all of these processes, syngas forms the basis of the reaction as its collection of hydrogen, carbon, and oxygen make it a flexible reactant.

Syngas is produced primarily through steam methane reforming (SMR), which creates syngas by using high temperature, high-pressure steam to break the hydrogen bonds on the methane. Steam reforming also produces excess carbon dioxide, a greenhouse gas,

that must be sequestered in a costly technique that accounts for 75% of a reforming plant's operational costs [7]. Catalytic “dry” reforming of methane (DRM) utilizes carbon dioxide to produce syngas, named such as it does not require steam to run, is proposed as one of the most promising technologies to be used in conjunction with steam reforming to utilize these greenhouse gases rather than sequestering them, which would save money and produce more usable syngas [8]. Dry reforming, however, requires more energy than steam reforming and quickly deactivates the catalyst used in its process due to solid carbon formations on the catalyst [9].

To address these issues, research has been focused on the exploration of promoters, supports and more recently, nanostructuring [10]. This research is focused on the use of nanostructures produced via low-cost scalable methods such as electrospinning and electrochemistry to act as catalytic material and supports to lower the required reaction energy and decrease carbon deposition-based deactivation. Additionally, to meet the needs of low-cost gas sensing in the reforming industry the nanomaterials produced will be used as passive chemiresistive gas sensors for use with a variety of organic gases.

1.1.1 Motivation for Research

America is currently having a boom in natural gas production. The total verified natural gas reserves in the U.S. is estimated to be more than 300 trillion cubic feet, with shale gas expected to increase this number [11]. Shale gas itself is growing quickly as a natural gas source rising from 1% in 2000 to 20% in 2010 with Louisiana's Haynesville field having an estimated amount of 75 trillion cubic feet of shale natural gas. Other sources of methane such as biomass gasification make for an attractive source of energy for the future.

As natural gas use is expected to increase, other sources of energy are expected to decrease. Natural gas is currently projected to account for 40% of energy production by 2040. Other sources such as crude oil level off as their resources are depleted while coal declines to 12% by 2040. The Energy Information Administration (EIA) projects the US to be a primary energy exporter by 2026 using current projections with natural gas being our primary export. **Figure 1-1** is reproduced via the EIA's Annual Energy Outlook for 2017. These projections highlight the importance of natural gas research in the United States [12]. Of importance is the rate of growth is noted based on current trends, the data does not consider scientific advances that may open up new avenues of natural gas utilization. This means that the factor could be much higher with an appropriate amount of research and development into the utilization of natural gas, such as dry reforming.

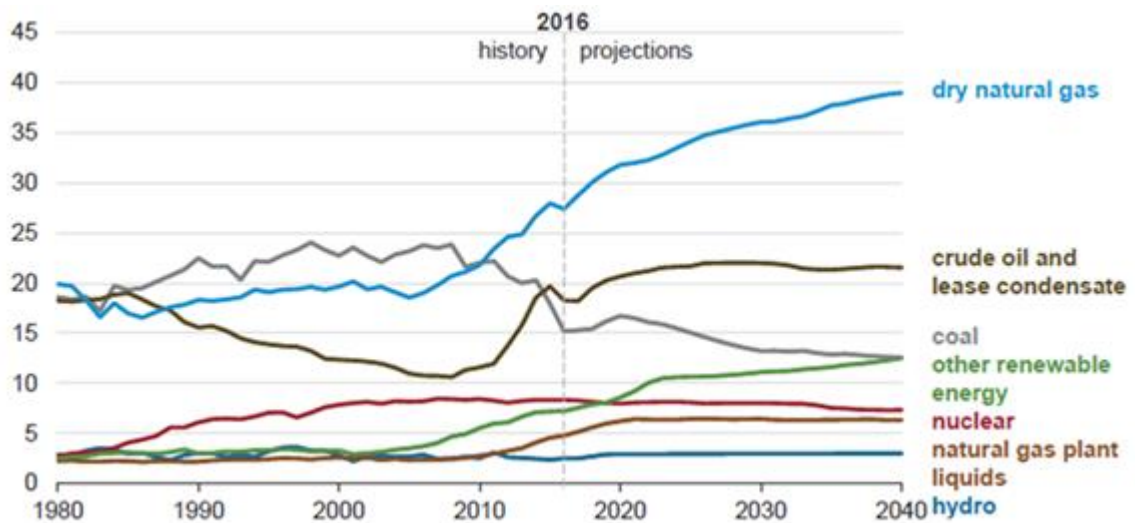


Figure 1-1: Energy production projections in quadrillion BTUs (produced by EIA).

Figure 1-1 highlights the decline of coal based on current usage and implementation of clean power plans, while crude oil is seen as leveling off in 2025 as oil recovery tapers off. Like natural gas, its projections can change drastically with changes via research and development of new technology. **Figure 1-2** shows projected energy trade as a reference case based on current projections of production and technology. As the United States continues to develop its natural energy resources, it is projected to be a net exporter of energy by 2026. Currently, petroleum and crude oil account for most of the U.S. energy trade. Coal has been an export of the U.S. for some time, but it is expected to decline as other markets become available worldwide. As natural gas reforming and liquefaction technologies continue to improve, these are expected to dominate our exports by 2020 [12].

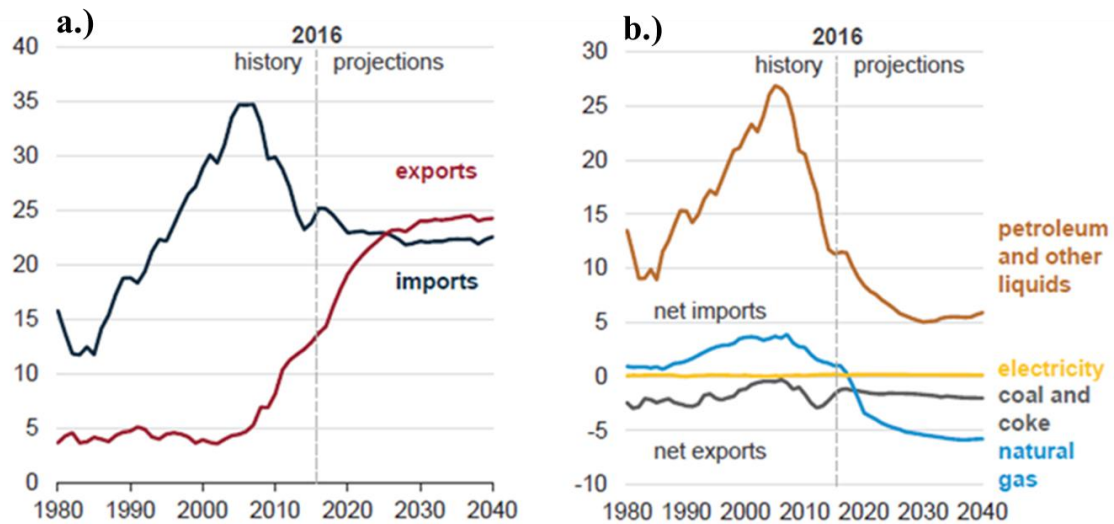


Figure 1-2: a.) Energy trade (in quadrillion BTUs) and b.) net energy trade (in quadrillion BTUs) (produced by EIA).

With current technologies, CO₂ emissions are expected to increase continuously through the next century rising to up to 970 ppm in the atmosphere [13]. As the world's population continues to rise, so too do CO₂ levels associated with the use of fossil fuels for energy heat and industry. **Table 1-1** shows population, GDP and CO₂ emission growth over the course of the next 100 years according to the Intergovernmental Panel on Climate Change's (IPCC) Special Report on Emissions Scenarios (SRES).

Table 1-1: SRES scenarios and their implications for climate change due to CO₂ emissions. (Produced by IPCC).

Date	Global Pop (Billions)	Global GPD (10 ¹² USD /yr)	Per Capita Income Ratio	Ground-Level O ₃ Conc (ppm)	CO ₂ Conc (ppm)	Global Temp Change (°C)	Global Sea-Level Rise (cm)
1990	5.3	21	16.1	--	354	0	0
2000	6.1-6.2	25-28	12.3-14.2	40	367	0.2	2
2050	8.4-11.3	59-187	2.4-8.2	~60	463-623	0.8-2.6	5-32
2100	7.0-15.1	197-550	1.4-6.3	>70	478-1099	1.4-5.8	9-88

As shown by **Table 1-1**, the possibility exists to limit global temperature increase to 2 °C by 2100, preventing the more catastrophic effects of an increase in temperatures up to 2.7 °C or higher, including long drought, extreme weather, food shortages and spread of infectious diseases [14].

As demand for energy continues to grow exponentially with population, we must look into alternatives sources than fossil fuels. This is particularly true for crude oil and oil sands, as oil reserves are finite and have been predicted to peak as soon as 2021-2046. This potential peaking is shown in **Figure 1-3**, taken from a report prepared by Oak Ridge National Laboratory for the Department of Energy and presented in the Journal of the Transportation Research Board in 2004 [17]. If plans for the transition from oil are not made now, the potential for a devastating impact on the future economy is possible. This is particularly true for transportation, as reliance on liquid fuels continues primarily in this sector. As growing nations continue to develop, their use of vehicles will see a similar exponential growth, furthering the use of oil and gas. It is essential to begin a transition into more stable sources of fuel in order to support this growth.

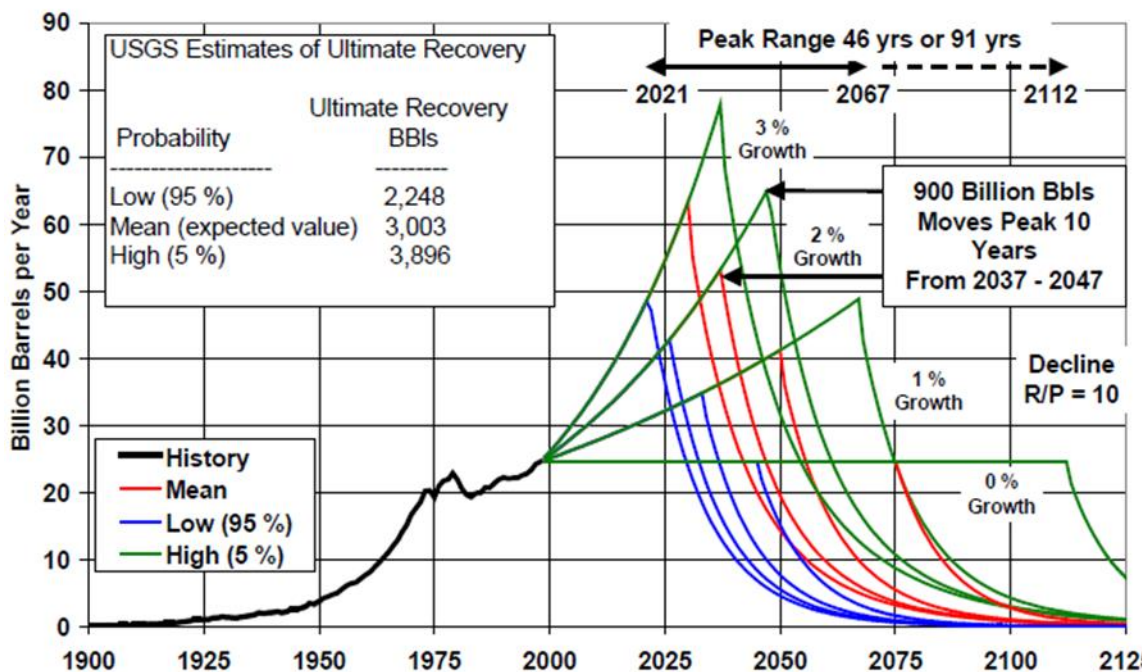


Figure 1-3: Peak oil estimations. (Produced by the DOE)

One such avenue is the use of biomass for fuel production. Biomass is defined as an organic material, typically waste products, from plants and animals. This can include anything from yard clippings or inedible parts of animals that might be thrown out during food processing to human sewage. One current technology utilizes corn husks to produce ethanol as an energy-rich fuel source. Unfortunately, ethanol contains less energy to be released by combustion than gasoline does, typically taking 1.5 gallons of ethanol to put out the same amount of energy as 1 gallon of gas. Biomass, however, can also be used as a fuel source in fluidized bed reactors, and gasification can produce component mixtures that can be used in dry reforming. This offers a valuable avenue for producing syngas from biomass without emission of carbon dioxide into the atmosphere [9,10].

Hydrogen is also a focus of the energy industry due to its high energy density and abundance as well as being clean to burn. Though abundant, hydrogen is not found in a gaseous diatomic form on earth due to its low mass and is typically recovered from hydrogen-rich chemicals such as methane or paraffin. This recovered hydrogen can then be used to create fuel hydrogen-rich materials that can be used as fuel cells. While current technologies are being developed for the efficient storage and retrieval of hydrogen within fuel cells, development should also focus on efficient ways to recover hydrogen from other chemicals while capturing carbon from being released into the atmosphere [17].

Dry reforming has the potential to provide useful products from methane without the emission of CO₂. Initial coupling with current steam reforming plants would allow for a dramatic reduction on emissions of greenhouse gases. Use of DRM to reduce CO₂ emissions would be done in several steps. First, SMR would produce a syngas CO₂ water

mix. Secondly, the syngas, CO₂, and water mixture would be separated via a CO₂ membrane into CO₂ and syngas/water. The syngas/water mix would be heated to remove the water, while the syngas would be fed into the dry reforming mechanism along with the dry CO₂. Finally, the DRM mechanism would utilize an additional methane feed with the carbon dioxide produced by steam reforming to produce more syngas. While this process has the potential to lower SMR's global warming potential (GWP), the additional heat required to power the DRM systems reduces its impact and using current technology was deemed too low of an impact on the climate with regards to current industry waste reduction algorithm (WAR) standards. It was noted that for the environmental impact of an SMR+DRM system to be maximized, more advanced catalysts for dry reforming were required to lower operational temperatures. Collection of deactivating carbon on the current dry reforming catalysts was also noted as a hurdle to this process [9].

Dry reforming offers a solution to the production of a liquid gas precursor (syngas) while lowering environmental greenhouse gas emissions by capturing carbon and transforming it into useful chemicals through other industrial processes. Due to its ability to use multiple feedstocks and the requirements of an ever-growing hydrogen economy, advances into dry reforming catalysts are sure to have a large impact on energy for the next century.

1.1.2 Objectives of Dissertation

For the dry reforming reaction to become economically viable, three problems will be addressed by this dissertation. The first problem is that dry reforming utilizes more energy than the current industrial process, steam reforming, making coupling of dry reforming with existing steam reforming technology unviable. Second, the dry reforming

reaction creates solid carbon deposition on the surface of the catalyst, deactivating active catalytic sites. Third, sensing mechanisms for industrial gas reactions give broad reaction data and are not useful for determining intermediates reaction species. To meet these three problems, nanofiber ceramic catalysts were fabricated and tested in the dry reforming reaction to increase reactivity by increasing surface area and reducing coking by introducing side reactions through promoters. Due to the unique electronic structure of graphene, it was used tested as a support structure for loaded nanoparticle catalysts to reduce carbon deposition on the surface of the catalyst. Finally, sensors were made and tested for real-time responses to organic species utilizing the same nanofiber and graphene synthesis techniques for the sensing material.

As an overview of this dissertation, chapter 2 will review literature detailing the current state of syngas manufacturing techniques as well as the state of the art in reforming methods. Chapter 3 will detail heterogeneous and homogeneous metal nanofiber catalyst synthesis, characterization and testing of the nanofiber catalysts in the dry reforming reaction. Chapter 4 will discuss nanoparticle metal loaded graphene catalyst fabrication, characterization, and testing in the dry reforming reaction. Chapter 5 will detail the use of catalytic nanofibers in gas sensing mechanisms. Chapter 6 draws conclusions from the work presented and discusses the future state of this body of research.

CHAPTER 2

DRY REFORMING REACTION LITERATURE REVIEW

2.1 Introduction

This chapter acts as a review of the research into the dry reforming process. First, to better understand the impact of dry reforming on the chemical processing industry and the world, the history of methane reforming will be discussed. Then, the various reforming processes being explored will also be discussed to show how dry reforming fits within the reforming industry. The mechanisms of solid carbon formation on the surface of the catalyst and the research being done to prevent and reduce this process will also be discussed along with the role of catalytic supports in preventing and reducing carbon formation while promoting the dry reforming reaction. Next, the mechanisms of different catalytic material will be discussed as well as different synthesis procedures for catalysts. Finally, a review of recent nanostructuring techniques and their effects on the reactivity of catalytic materials will be explored in this chapter.

2.2 History of Reforming

Syngas reforming has a long history in the chemical engineering industry and the world. The creation of synthetic fuels using syngas began before World War I in Germany, with the Bergius process developed by Friedrich Bergius being patented in 1913, which

used a direct conversion of coal to synthetic fuels. Using this process, dried coal is mixed with oil and a catalyst into a reactor at temperatures of 400-500 °C and pressures of 20-70 MPa. Using this process produces heavy oils and gasoline as well as large amounts of carbon dioxide. Due to technical difficulties associated with constructing high-pressure processing facilities and inflation after World War 1, Bergius sold the patent to the Baden Aniline and Soda Factory (BASF) where the process was refined by Carl Bosch. This process eventually won Bergius and Bosch the Nobel prize in 1931 for introducing the world to high-pressure chemical engineering [15].

In 1923, Franz Fischer and Hans Tropsch were the next to experiment with indirect coal conversion into synthetic fuels, a process that first gasifies coal into water gas, which is a product of syngas that has undergone a water-gas shift reaction, a side reaction of methane reforming where hydrogen from methane combines with the oxygen from carbon monoxide and creates water. Carl Bosch, the man who eventually worked on Bergius's coal liquefaction process, initially began his work at BASF with Fritz Haber, and together made an industrial-level high-pressure process to fix nitrogen using syngas into ammonia known as the Haber-Bosch process. These discoveries have since been used to produce ammonia using syngas as a hydrogen source [5].

During World War II, synthetic fuels via these early processes were widely used in Nazi Germany due to lack of natural oil reserves and the Allied Forces cutting off their paths to oil. Reactor facilities were constructed in Germany and occupied countries and run by the Nazis which were used not only as fuels for their vehicles but also powered their industrial plants. These plants became such a powerhouse that during the war the Allies conducted a strategic air campaign against these factories and in hundreds of bombing

strikes to disable the energy infrastructure of the Nazis, dealing a significant blow to their armaments programs and was one of the major victories of the Allied Nations.

After World War II, high-pressure reactions with coal and natural gas became the subject of research in America. Starting in 1945, the US Army transferred an ammonia production factory in Louisiana, Missouri over to synthetic fuels via coal hydrogenation. During this time, natural gas became a staple of American energy and heat, accounting for 17% of the energy consumption in the mid-1940s to 1950s and increasing to 30% in the 1960s, a period known as the “Golden Age” of natural gas. Due to this increasing usage, the US began funding research into coal mechanization. This funding increased during the 1970s as the oil crisis hit, increasing joint research between the US, Germany, and Britain. The process most used in the 1960s-1970s was the Lurgi-Ruhrgas process, which utilized the work of Lurgi Gesellschaft für Wärmetechnik G.m.b.H. and Ruhrgas A.G., who worked during the 1940s on low-temperature coal liquefaction. This process was used during this time because it was the only commercially viable process due to building material constraints. This process utilizes solid coal and two adiabatic reactors in the fixed bed setup to cut costs in running the process. Eventually, however, oil prices began to lower and as the oil economy globalized, government funding for synthetic fuel research dwindled [16,17].

In the last decade, there has been a renewed focus on the reduction of greenhouse gases using alternative reactions and chemical sequestration [13]. With this information and the renewed focus on lowering carbon emissions and hydrogen storage, it becomes clear that refining the methods used to produce syngas becomes paramount to the chemical production industry and the emerging hydrogen-based economy. Dry reforming can

eliminate the need for costly carbon dioxide sequestration by being used in conjunction with current steam reforming technology, taking the carbon dioxide produced by the reaction and turning it into syngas [9]. Additionally, due to the dry reforming reaction's endothermic nature makes it a potential for a chemical energy storage system utilizing solar, wind, or nuclear energy [16]. The system allows for the transmission of clean energy to efficiently be stored and converted into chemical fuels or other forms of chemical energy. A diagram of such a storage system is shown in **Figure 2-1**. This system would utilize dry reforming to act as the thermochemical reaction taking place. This reversible endothermic reaction is pushed to equilibrium utilizing clean energy such a solar/wind power or nuclear power. The syngas then is used to store the energy given to the reaction, which can be saved and transported for later use or be utilized to create fuels that release the stored energy in exothermic reactions.

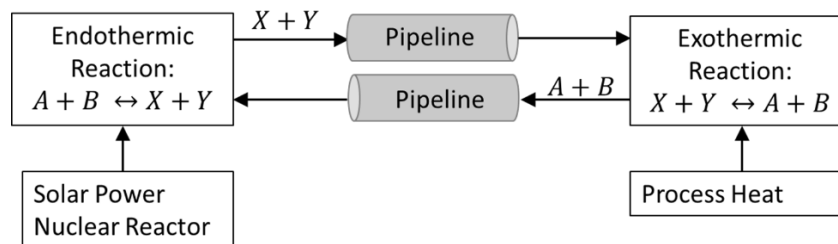


Figure 2-1: Schematic of a Chemical Energy Transmission System (CETS).

Indeed, one such reaction pathway, known as the Eva-Adam process, has found use in Germany, Israel, the United States and Russia. The Eva-Adam process uses steam reforming of methane as the forward reaction and a methanation process as a reverse reaction. The products of the steam reforming reaction; carbon monoxide and hydrogen

gas, are then sent by pipeline to a facility where a reverse reaction forms methane and sends it back to the initial plant via pipeline. For this process, water produced is removed during the methanization process. **Figure 2-2** shows the Eva-Adam process. Dry reforming offers a superior alternative to the Eva-Adam process, as dry reforming has a better energy difference for this. Additionally, all reactants and products would be gaseous (as opposed to liquid in steam reforming) making transport less expensive [10].

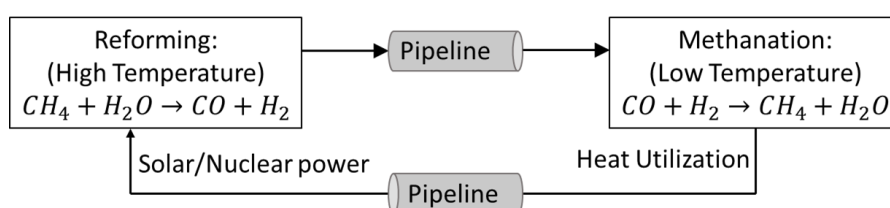


Figure 2-2: The Energy Transfer “Eva-Adam” process for CETS.

As the depletion of natural oil sources continues and alternative fuels and cleaner energy gain traction, synthetically produced hydrocarbons offer one of the few potential alternatives to traditional fuel sources. As research continues into synthetic processes the commercialization cost of these processes become lower and more viable. Additionally, advances in nanomaterials offer the potential to lower commercialization costs even further.

2.3 Reforming Reactions

To understand the current fuel economy, it’s important to understand the processes associated with refinement and compare these to the research into synthetic fuels. This

section will explore the different reforming techniques currently employed by industry as well as research techniques that are the subject of this dissertation.

2.3.1 Methane Reforming

Several methods exist for the reformation of methane into not only syngas but a variety of other precursor chemicals. These methods vary based on the desired result, typically expressed in the amount of hydrogen as a ratio to other products in the end results but are also dependent on other factors such as the size of the plant, the energy required to maintain the plant's systems or geographical region. Process steps for different reforming methods are listed in **Table 2-1**. These different processes will be explored below.

Table 2-1: Chemical reforming processes and associated energies.

Relevant reaction:	Enthalpy of reaction:
Steam Reforming:	
$\text{CH}_4 + \text{H}_2\text{O} \rightarrow \text{CO} + 3\text{H}_2$	$\Delta H_r = 206 \text{ kJ / mol}$
$\text{CO} + \text{H}_2\text{O} \rightarrow \text{CO}_2 + \text{H}_2$	$\Delta H_r = -41 \text{ kJ/mol}$
Partial Oxidation:	
$\text{CH}_4 + \frac{1}{2} \text{O}_2 \rightarrow \text{CO} + 2\text{H}_2$	$\Delta H_r = -38 \text{ kJ/mol}$
Auto-Thermal Reforming:	
$\text{CH}_4 + \frac{1}{2} \text{O}_2 \rightarrow \text{CO} + 2\text{H}_2$	$\Delta H_r = -38 \text{ kJ/mol}$
$\text{CH}_4 + 2\text{O}_2 \rightarrow 2\text{H}_2\text{O} + \text{CO}_2$	$\Delta H_r = -802 \text{ kJ/mol}$
$\text{CH}_4 + \text{H}_2\text{O} \rightarrow 3\text{H}_2 + \text{CO}$	$\Delta H_r = 206 \text{ kJ/mol}$
$\text{CO} + \text{H}_2\text{O} \rightarrow \text{H}_2 + \text{CO}_2$	$\Delta H_r = -42 \text{ kJ/mol}$
Dry Reforming:	
$\text{CH}_4 + \text{CO}_2 \rightarrow 2\text{H}_2 + 2\text{CO}$	$\Delta H_r = 247 \text{ kJ/mol}$

2.3.2 Steam Reforming

The steam methane reforming method was the first to be used to reform methane into syngas and its constituents. This process is governed by two equations, first the conversion of methane and steam into carbon monoxide and hydrogen gas, and the second known as the water gas shift that adds more steam to create carbon dioxide and hydrogen gas which allows for as much hydrogen to be freed as possible from the reaction. Carbon dioxide is then separated from hydrogen via pressure swing adsorption [6].

For natural gas to be used in steam reforming, it first must be desulfurized to prevent sulfur typically found in natural gas deposits from poisoning the catalysts. This is accomplished by heating the gases and flowing them through molecular sieves, or through a process called hydrodesulfurization (HDS) which uses hydrogen gas and a catalyst (such as CoMo) and heat to produce a hydrogen sulfide by-product which can then be used to make sulfuric acid or any other sulfur-containing by-product. After the HDS step, steam is added at high temperature and pressure to begin the reforming process. Reforming typically takes place using a nickel-containing catalyst in the presence of steam at a temperature of 700-800 °C and 3-5MPa. This produces syngas and CO₂ as a by-product. As development on the reaction continues, further sub reactions are promoted to achieve a more desirable final product. The water gas shift is one of them and utilizing metal oxide catalysts, is used to drive a higher hydrogen and carbon dioxide ratio. This process is carried out using dual reactors with different catalyst types, the first one is less selective toward hydrogen. Finally, steam reforming shares similar thermodynamics with dry reforming but due to larger CO₂ levels is less prone to coking which is one of the major reasons why steam reforming has been favored in industry [18].

2.3.3 Partial Oxidation

Partial oxidation refers to both thermal partial oxidation (TPOX) or catalytic partial oxidation or (CPOX), both of which partially combust the methane using air in a high temperature reforming reactor to produce more hydrogen. TPOX uses extremely high temperatures nearing 1500 °C to produce hydrogen-rich syngas. CPOX uses a catalyst to

bring the temperature down to nearly 800 °C, and the ratios of reactants become more important during this reaction type [19].

2.3.4 Autothermal Reforming

Autothermal reforming is a method that uses an air inlet as an oxygen source. Utilizing oxygen from air in dry reforming allows for combustion of methane, providing heat to help drive the reaction. This process encompasses a large number of reactions within it. Because of this, control over reaction conditions can lead to varying products. At lower temperatures, carbon dioxide and water with small amounts of hydrogen and carbon monoxide are produced, while at higher temperatures the ratio shifts more towards hydrogen and carbon monoxide as the dry and steam reforming reactions become dominant. At higher temperatures, the water-gas shift reaction will overtake the production of hydrogen and carbon monoxide. For this process, ruthenium is used, as nickel will oxidize due to the presence of oxygen which deactivates the catalyst [20].

2.3.5 Dry Reforming

Dry Reforming is an endothermic reaction that typically uses catalysts such as cobalt, nickel, and rhodium to produce syngas. Dry reforming also produces side reactions, and thus increasing selectivity to hydrogen and carbon monoxide is important when considering catalyst choice. Nickel is often used as a catalyst for dry reforming because of its lower cost compared to ruthenium, but nickel tends to deactivate due to carbon deposition quicker than rhodium. Carbon formation on nickel typically begins at the interface between the nickel metal and its support, creating whiskers of carbon branching out from the interface. The support of choice for dry reforming is typically gamma alumina (Al_2O_3) due to its inherent basicity and stability [21].

Wei *et al* studied the kinetics of dry reforming, showing that the only kinetically relevant step on a catalyst was the activation of the first C-H bond within methane on both rhodium and nickel with various supports [22]. Within this kinetic mechanism, methane completely decomposes in a stepwise dehydrogenation process which spreads chemisorbed reactants (denoted by a * next to the chemical name) carbon and hydrogen (denoted by C* and H*) across the catalyst with very little CH_x. Oxygen from carbon dioxide then reacts with the C* producing carbon monoxide. The H* reacts to form hydrogen gas or with the oxygen to form OH groups, which eventually react with another hydrogen to produce water. In this model, the co-reactant, CO₂, is only used to remove surface carbon and hydrogen, allowing the catalyst to have vacant active sites for more reactions. When the surface has sufficient active sites, the C-H activation becomes the rate-determining step and thus the reaction is proportional only to the methane and not the carbon dioxide [23].

Different kinetic studies focus more on the activation of CO₂ as kinetically relevant, using Ni as their catalyst. These focused on several different temperature regimes. Due to carbon formation on the catalyst, there was difficulty in determining how important the carbon dioxide was to the kinetics of the reaction, except that it was necessary for the mechanism of keeping surface interactions proceeding [24, 25].

There are several side reactions that occur during the dry reforming process that take place within the reactor under various conditions. **Table 2-2** introduces these reactions and their associated free energies.

Table 2-2: Reactions of dry reforming of methane and their free energies.

Dry Reforming Reaction	$\text{CH}_4 + \text{CO}_2 \rightarrow 2\text{H}_2 + 2\text{CO}$	$\Delta H_r = 247 \text{ kJ mol}^{-1}$ $\Delta G^\circ = 61770 - 67.32 T$
Reverse Water Gas Shift	$\text{CO}_2 + \text{H}_2 \leftrightarrow \text{CO} + \text{H}_2\text{O}$	$\Delta H_r = 41.2 \text{ kJ mol}^{-1}$ $\Delta G^\circ = -8545 + 7.84 T$
Dehydrogenation	$\text{CH}_4 \leftrightarrow \text{C}(\text{solid}) + 2\text{H}_2$	$\Delta H_r = 75 \text{ kJ mol}^{-1}$ $\Delta G^\circ = 21960 - 26.45 T$
Boudouard Reaction	$2\text{CO} \leftrightarrow \text{C}(\text{solid}) + \text{CO}_2$	$\Delta H_r = -171 \text{ kJ mol}^{-1}$ $\Delta G^\circ = -39810 + 40.87 T$
Hydrocarbon Reactions	$2\text{CH}_4 \leftrightarrow \text{CH}_3\text{CH}_3 + \text{H}_2$ $2\text{CH}_4 \leftrightarrow \text{CH}_3\text{CH}_3 + \text{H}_2$	$\Delta H_r = 64.4 \text{ kJ mol}^{-1}$ $\Delta H_r = 201.5 \text{ kJ mol}^{-1}$

With these side reactions, it can be shown that the reverse water gas shift does not take place above 800 °C and the Boudouard reaction takes place below 700 °C [26]. From these equations, it can be further intuited that the standard lower limit to the reaction is 640 °C to activate the carbon dioxide reforming reaction and the reverse water-gas shift reaction. Due to the presence of the reverse water gas shift reaction, water vapor will always be present in the reaction area. The amount of water is determined by the ratio of reactants, with higher ratios of CO_2/CH_4 leading to larger amounts of water and lower hydrogen gas yield.

Figure 2-3 compares the mole fraction of reactants and products over a range of reaction temperatures for the dry reforming reaction in a simulation carried out in the

software GASEQ. The reactant gases, CH₄ and CO₂, are at a 1:1 ratio and the simulation was carried out at standard pressure (1 atm). The water gas shift reaction is shown here to be active at all temperatures below 900 °C, leading to a reduced hydrogen yield compared to carbon monoxide. As the reaction is highly endothermic, a full conversion of the reactants is shown to happen at 900 °C, and a 1:1 ratio of reactants is shown to be an ideal mixture for synthesis gas production.

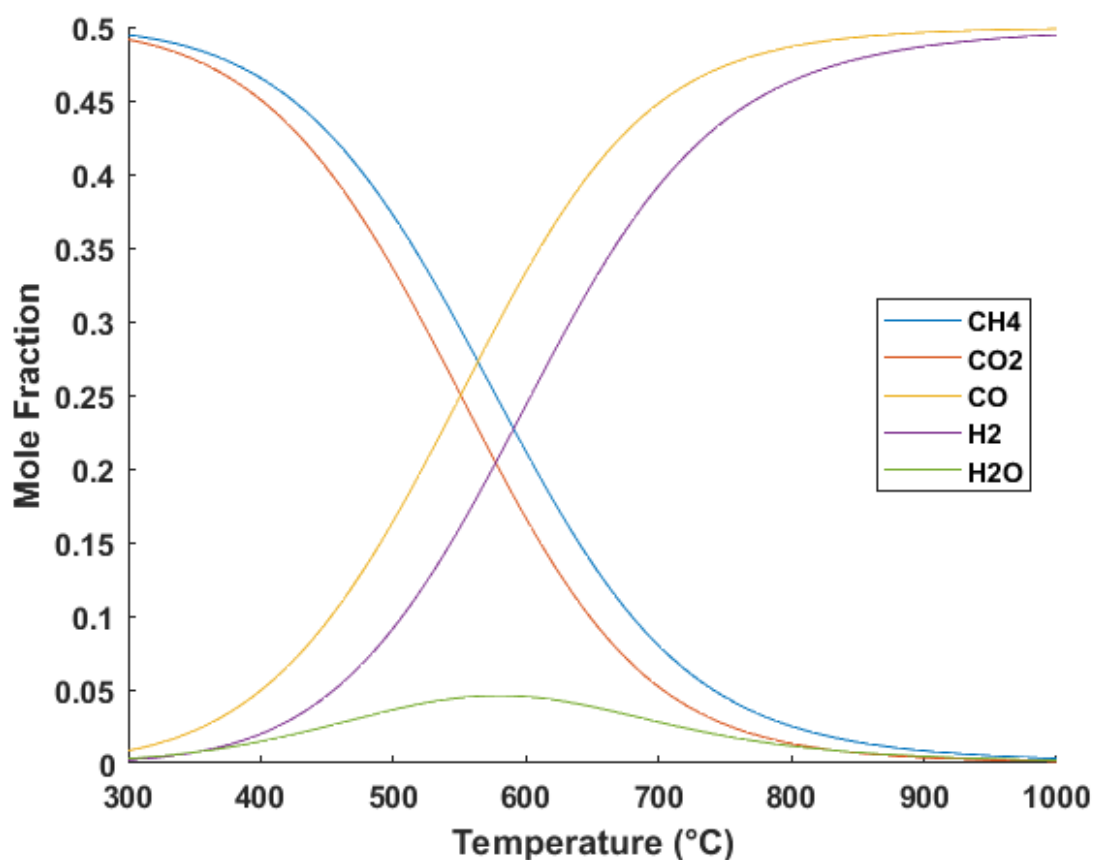


Figure 2-3: Dry reforming reaction of CH₄ and CO₂ carried out at standard pressure and increasing temperature performed in GASEQ.

Maestri *et al* proposed a microkinetic mechanism for dry reforming which also shows the CH₄ activation as the kinetically relevant step, additionally narrowing down the step between CH₃ and CH₂ as the rate-determining step, with the other reactions quasi-equilibrated [27]. The dry reforming reaction proceeds from the dehydrogenation of CH₄ to chemisorbed surface C* and it was determined that it is then oxidized by OH* groups, not O*, to form CO. OH* has shown to come from H₂O activation or from CO₂ activation with surface H*. The reaction of CO₂* with H* acts as the step that produces CO from CO₂ and oxidizes carbon within methane. While active, the reverse water gas shift reaction produces some H₂O utilizing the OH* and H* on active sites but most hydrogen reacts to form H₂. Within this microkinetic mechanism, hydrogen mobility on the catalytic surface is very important for the activation of CO₂ and CH₄.

2.4 Coke Formation

Carbon deposition during dry reforming is known as coke formation, based on the high carbon fuels made using high heat. The formation of coke on the surface of the catalyst deactivates active sites on the catalyst, decreasing overall conversion of reactant gases. Coke forming carbon is available from both reactants, and two chemical paths exist for the formation of coke; one involving coke formation from the carbon in carbon dioxide (the Boudouard reaction), and one from the carbon found in methane (methane dehydrogenation). According to Erdöhelyi *et al*, who tested carbon formation on palladium via IR spectroscopy, carbon dioxide disassociation has the largest impact on coke formation and occurs at all temperatures. This was established by feeding oxygen and carbon dioxide into a reactor to study the decomposition of carbon dioxide. Afterward,

methane was fed into the reactor with oxygen to establish its contribution to the coking effect as it disassociated. Additionally, adding both carbon dioxide and methane to the reaction caused less carbon formation than carbon dioxide alone, suggesting that methane surface reactions impeded carbon formation [28].

Figure 2-4 shows the Gibbs free energy over a range of operational temperatures for the Boudouard and dehydrogenation of methane reactions. As shown by the graph, The Boudouard reaction is favorable during lower temperatures up to 650 °C, while the dehydrogenation reaction becomes more favorable from 650 °C upward. This indicates that coke formation happens at all operational temperatures. Additionally, there is research to suggest that the reduction of carbon monoxide by hydrogen gas could produce water and solid carbon in a back reaction during the reforming process [29].

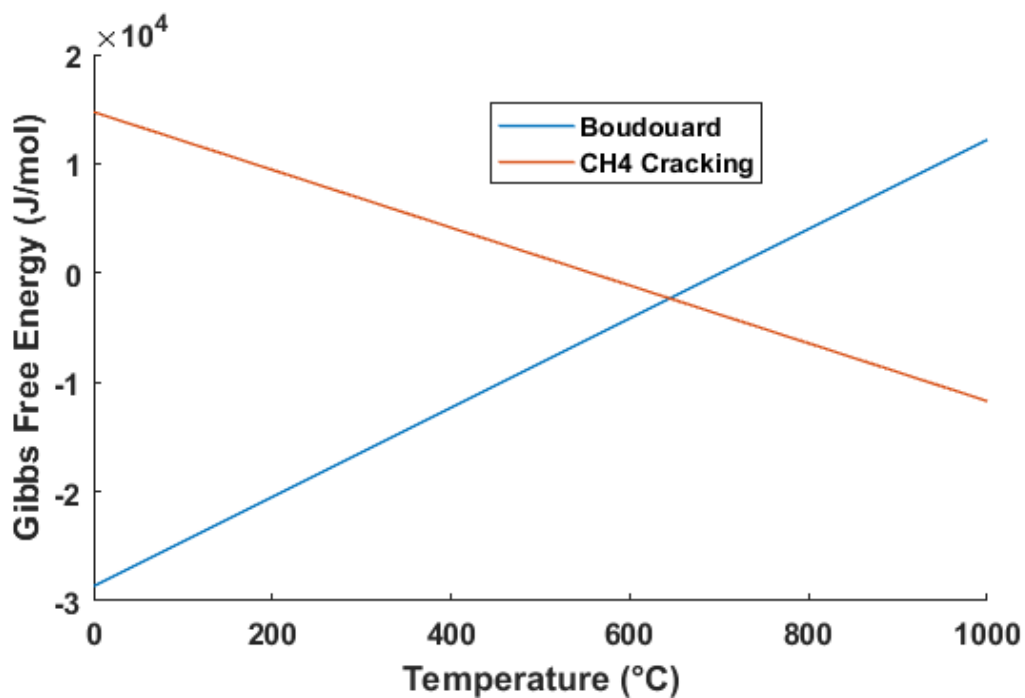


Figure 2-4: Gibbs free energy for Boudouard and CH₄ dehydrogenation reactions.

Via Ginsburg *et al.*, coke formation was modeled to show deactivation of catalytic sites via carbon whisker formation. Carbon whiskers form through diffusion of carbon from the reactions through nickel crystal structure causing carbon nucleation sites to occur. Ginsburg *et al.* further defines coke formation into 5 main types of carbon coking which are shown in **Table 2-3**. These five carbon formations are found in varying amounts depending on temperature, space velocity and total pressure within the reactor system [30].

Table 2-3: Coke formation types.

Classification	Description	Type
1: C_{α}	Adsorbed atomic carbon	Dispersed as surface carbide
2: C_{β}	Polymeric film and filaments	Amorphous carbon
3: C_{ν}	Vermicular whiskers or filaments	Polymeric or amorphous carbon
4: C_{γ}	Nickel carbide	Bulk in crystal
5: C_c	Graphene platelets or films	Crystalline carbon formation

Carbon formation is typically reported to be mostly C_{ν} and C_c under typical dry reforming temperatures 700-850 °C [31]. Both forms are typically the same or similar diameters to the catalyst particle, due to their growth on the active sites of the catalyst. Whisker growth happens as carbon is diffused through the catalytic crystals and is dependent on the concentration of carbon in the crystals. It was found that coking was strongly dependent on having three adjacent active sites free. The first two sites absorb carbon monoxide which causes the creation of CO_2 on site 1 and coke on site 2. CO_2 is

released into the reaction area and carbon monoxide is again absorbed on site 1 and 3, and the same reaction takes place, with carbon dioxide being formed and coking to happen on site 3. This would indicate the major reaction to contribute to coking is the Boudouard reaction, and the rate of coking is given by the following:

$$r_c = \frac{\vec{k}K_{CO}^2 p_{CO}^2 - \bar{k}K_{CO_2}K_C^2 p_{CO_2}}{(1 + K_C + K_{CO}p_{CO} + K_{CO_2}p_{CO_2})^3} \quad Eq\ 2.1$$

where \vec{k} , and \bar{k} are the forward and reverse rate constants of the reaction between site 1 and 2, K_{CO} , K_{CO_2} , and K_C is the absorption constants for carbon monoxide, carbon dioxide and coke respectively. The p_{CO} and p_{CO_2} terms are partial pressures for carbon monoxide and carbon dioxide. After this was determined, regression analysis was used to find that the $K_{CO}p_{CO}$ term was much greater than the $1 + K_C + K_{CO_2}p_{CO_2}$ term, allowing for the simplification of the previous equation to:

$$r_c = k_{app} \frac{\left(p_{CO}^2 - \frac{p_{CO_2}}{K_{eq}}\right)}{p_{CO}^3} \quad Eq\ 2.2$$

where $k_{app} = \vec{k}/K_{CO}$ is a ratio of the forward rate constant and the absorption of CO onto an active site and K_{eq} is the equilibrium constant for the Boudouard reaction in partial pressure terms. This equation shows that the rate of coking is very dependent on the partial pressure of the carbon monoxide within the reaction system and the configuration of active sites in the catalyst [32].

2.5 Role of Support

The role the support plays in dry reforming has been the subject of debate [21,33-38,44,45]. Studies have searched for rate changes between oxide supports, with discussions

on irreducible oxides vs reducible oxides finding that irreducible oxides seemingly have a higher rate of reaction. Others, however, found no impact from the reducibility of the oxides. Perhaps predictably, dispersion of catalytic material over the supports seems to have the greatest effect on reforming rates with uniform dispersion being the most important influencing factor. Another important factor in supports seems to be their basicity, as CO_2 is an acidic gas, meaning the absorption of CO_2 by a basic support may be the deciding factor in activity. As such, aluminum oxide is one of the strongest supports for the dry reforming reaction. **Table 2-4** lists tested supports in literature and their strengths based on catalyst.

Table 2-4: Catalytic activity per supports and supporting references.

Metal by activity	Metal loading (wt%)	Temperature (K)	Ref
Al ₂ O ₃			
Rh > Pd > Ru > Pt > Ir	1	823	33
Rh > Pd > Pt >> Ru	0.5-1	823-973	34
Ir > Rh > Pd > Ru	1	1050	44
Ni > Co >> Fe	9	773-973	34
Ni > Co >> Fe	10	1023	35
Ru > Rh	0.5	873	36
MgO			
Rh > Ru > Ir > Pt > Pd	0.5	1073	37
Ru > Rh > Ni > Pd > Pt	1	973	38
Ru > Rh ~ Ni > Ir > Pt > Pd	1	823	21
Ru > Rh > Pt > Pd	1	913	45
NaY			
Ni > Pd > Pt	2	873	42
SiO ₂			
Ru > Rh > Ni > Pt > Pd	1	973	37
Ni > Ru > Rh > Pt > Pd >> Co	0.5	893	37

Aluminum oxide (Al₂O₃), or alumina, is an amphoteric oxide commonly used as a support for catalysts in reforming reactions [39]. Alumina is produced through bauxite ore found in weathered aluminum-rich stones. Bauxite ore is purified to alumina using the Bayer process, developed by Carl Josef Bayer in 1887 as a method to supply alumina to the textile industry. This ore also typically contains other oxides such as iron, titanium, and silicon which are often still found as trace elements in alumina supports. After purification through the Bayer process, the alumina is calcined in air to remove water [40]. The surface area of alumina is determined by calcination conditions such as inlet gas and temperature.

The two main alumina isotopes are differentiated as γ - and α -alumina. γ -alumina (γ - Al_2O_3) is calcinated at 800°C and has surface areas around $100\text{ m}^2/\text{g}$ while α -alumina (α - Al_2O_3) is calcinated at 1200°C and has a surface area of around $5\text{ m}^2/\text{g}$. γ -alumina has a cubic spinel structure with the oxygen in a stacking structure of ABCABC, while α -alumina has a triagonal structure, with oxygens stacking in its c direction. Due to its high surface area, γ - Al_2O_3 is considering the most useful as a support for catalytic reactions.

Studies have been done on the acidity of the support with respect to its effects on the oxidation states of the catalyst [41]. Temperature programmed desorption was done using an atmosphere consisting of ammonia over a nickel catalyst. It was found that the acidity of the support strongly affected the reduction effects of nickel oxide to nickel metal, making lower acidity supports the clear winners for the reduction of catalysts. A highly reduced catalyst allows for more active sites and increases conversion.

The introduction of promoters to the support further enhance the role of the support. Promoters are materials that assist the reaction in some way, either by offering an alternative reaction path or by enhancing selectivity. For the dry reforming process, promoters can assume several functions such as; increasing the absorption of CO_2 onto the support, decreasing the rate of the methane dehydrogenation reaction, or enhancing the rate of the surface interactions. Promoters, in this case, can be metals, metal oxides or a combination of the two. Additionally, the crystalline structure of the promoter can play a role in its promotion of the reaction by changing the surface of the catalyst [42].

2.6 Role of the Catalytic Material

Typically, dry reforming catalysts are either made of a noble metal or a nickel/nickel composite. While costs of noble metal catalysts are higher, but they are more

resistant to coking overall, while nickel is less expensive but cokes quickly. Noble metal catalysts have different coking and conversion rates from nickel-based catalysts. Information about noble catalytic metals on different supports and their conversion rates are listed in **Table 2-5** [43-49].

Table 2-5: Noble catalytic metal and supports based on reactant ration, conversion percentage, and temperature by reference.

Catalyst/Support	CO ₂ :CH ₄ Ratio	Conversion %	Temperature (K)	Ref:
Palladium and Platinum				
Pd/NaY	1:1	29.2	873	43
Pd/Al ₂ O ₃	1:1	70-75	1050	45
Pd/MgO	1:1	84	963	45
Pt/NaY	1:1	156.3	873	43
Pt/MgO	1:1	85	963	45
Rhodium and Ruthenium				
Rh/TiO ₂	1:1	88.2	893	46
Rh/SiO ₂	1:1	5.1	893	46
Rh/Al ₂ O ₃	1:1	85.1	893	46
Rh/MgO	1:1	88	963	45
Ru/Al ₂ O ₃	1:1	60-70	1050	44
Ru/Eu ₂ O ₃	1:1	75	923	47
Ru/MgO	1:1	90	963	45
Iridium and Cobalt				
Ir/Al ₂ O ₃	1:1	85-90	1050	47
Ir/Eu ₂ O ₃	1:1	88	1000	48
Co/MgO/C	1:1	65-75	923	49

Most research into dry reforming uses the transition metal nickel as its main catalytic material due to its low cost and high activity [50]. Nickel is an important metal in reforming reactions, described in 1922 as a “spirited horse” with an “excessive activity and a maximum alterability” [51]. This activity is coupled with a noted low sustainability due

to carbon deactivation as the traits most associated with nickel catalysts. With the development of nanotechnology, nickel has shown itself to be able to strongly shift π bonds in carbon nanostructures. This can lead to the incorporation of nickel nanoparticles into graphene grown via CVD. It is due to this affinity for carbon structures that makes nickel a good catalyst for dry reforming, yet it is also why carbon deactivates nickel as quickly as it does [52]. Due to the importance of nickel metal as a catalyst for the dry reforming reaction, it is separated from the noble metals in **Table 2-5** into its own table. **Table 2-6** lists conversion rates for various nickel catalysts over different supports based on feed ratios, conversion percentages, and temperature by reference [41,42,48,49].

Table 2-6: Noble catalytic metals in the dry reforming reaction based on feed ratio, conversion, and temperature by reference.

Catalyst/Support	CO ₂ :CH ₄ Ratio	Conversion %	Temperature (K)	Ref:
Ni/NaY	1:1	84.0	873	41
Ni/Al ₂ O ₃	1:1	36.3	873	41
Ni/SiO ₂	1:1	14.9	873	41
Ni/Al ₂ O ₃	1:1	80-90	1050	42
Ni/CaO-MgO	1:1	80	1123	48
Ni/Al ₂ O ₃	2.38:1	100	1213	49
Ni/MgO-Al ₂ O ₃	2.38:1	86	1211	49
Ni/CaO-Al ₂ O ₃	2.01:1	88	1211	49
Ni/CaO-TiO ₂ -Al ₂ O ₃	2.01:1	100	1223	49

Rostrup-Nielsen *et al* studied various nickel catalysts in the dry reforming reactions for coke formation via methane and carbon monoxide decomposition, the two most widely accepted coke forming reactions, from 450 to 750 °C [53]. Equilibrium constants for both reactions were influenced by the configuration of nickel active sites which increases concentrations of carbon monoxide and methane versus the absence of the nickel, which

was tested with graphite as a stand-in for the nickel. The equilibrium concentrations were found to increase with smaller nickel crystal sizes. Lower temperatures showed higher variation between the graphite and nickel catalyst equilibrium concentrations. The reactions changed at different rates, with the carbon monoxide decomposition rate varying more than the methane decomposition. Supports and promoters had less of an effect than the size of the nickel crystal particles, however, the addition of sulfur on the surface of the catalyst slowed coke growth. Experimental deviations between reaction equilibrium between nickel catalysts and graphite control tests were observed to be based on coke growth on the nickel catalyst, particularly whiskers (C_v), which were found to be the exact same diameter as the nickel crystals. The addition of the surface sulfur is useful then for deactivate sites, leading to less carbon deposition due to the separation of active sites on the catalyst as described in section 2.4 and section 2.5.

2.6.1 Nanostructured Catalysts

Nanostructured catalysts offer an exciting avenue of research for the dry reforming reaction due to their higher surface area per gram, control of particle dispersion and, by adding nanoparticle dopants, precise control of the selectivity of the catalysts [54-65]. There are several techniques explored for the fabrication of nanostructured catalysts, all with the aim to increase the reactivity of the catalyst by increasing surface area and reducing bulk material.

Using co-precipitation or wetness impregnation, metal salts such as nickel nitrate can be loaded into mesoporous supports and sintered to create nanoparticle nickel crystals that are dispersed within the mesopores of the support. For an example of a wetness impregnation technique, nanocasting was used for the creation of metal catalysts in a solid

mesoporous silica and was found to be useful with heterogeneous catalysts in instances when heavy sintering may change the desired crystal structure. In de Sousa *et al.*, mesoporous silica was purchased and added to an organic solvent. Then, an aqueous metal nitrate solution was added dropwise to the supports under stirring. After loading the solution, it was heated and then the top layers of the silica were removed using acid to expose the nickel-cobalt nanocrystals. This catalyst was shown to shift the growth of coke from whisker types to graphene types, which suggests nanostructuring can control surface-coking interactions [54].

Research into synthesizing mesoporous supports falls into two main categories based on methodology – surfactant-assisted synthesis and template-assisted synthesis. Surfactant-assisted synthesis uses a surfactant to disperse alumina in a solution which is then dried of solvent to allow the nanoparticles to form a solid which is then heated and washed. This is shown by Cabrera *et al.*, who utilizes the surfactant triethanolamine in an ethanol solvent to produce mesoporous alumina for use as a nickel nanoparticle support [56]. Template assisted synthesis uses a nanoparticle template precursor such as alkyl carboxylate that is loaded into an aluminum-containing solution and then sintered, causing the aluminum to form into a solid alumina. Then, the template is removed either through a chemical method or through heating, leaving voids in the alumina that can be utilized as mesopores for loading of nanoparticles through a traditional wetness impregnation technique [57].

Zeolites have also been tested as a support for metal catalysts in the dry reforming reaction. Zeolites, a formation of aluminosilicate minerals, are well known for their molecular sieve properties and mesoporous nature which makes them an attractive support

for nanoparticle catalysts. A zeolite support known as Zeolite Socony Mobil-5 (ZSM-5) was studied as a support for nickel nanoparticle-based catalyst by creating a colloidal suspension of nickel in ethylene glycol and sodium hydroxide. This was mixed with the prepared ZSM-5, stirred for 24 hours and then dried at 160 °C. After drying it was crushed into a powder and calcinated. 5 wt% nickel catalysts in ZSM-5 were found to have a high conversion of methane at 96.2% at 800 °C, with activity constant for 5 hours. Carbon buildup was shown to be formed after 5 hours of testing, with the acidity of the support though to be one of the influencing factors in coke formation [58].

Nanostructures made using more unique templating methods have also been tested for dry reforming. González *et al.* used a hydrotalcite, or a layered double hydroxide, in a mixture of nickel magnesium and aluminum to create nanospheroids for use as a coke resistant catalyst in dry reforming. Nanospheroids made of a nickel magnesium aluminum were fabricated by first creating the aluminum precursor by adding the aluminum tri-sec-butoxide with a refluxed ethanol and after mixing, adding nitric acid dropwise to the solution to form a gelatinous solution. Then, acetic acid was added and mixed and the sol-gel was cooled to 0 °C, after which the magnesium methoxide was added dropwise with stirring, which created a Mg-Al hydrotalcite. Nickel acetate in ethanol was added to the Mg-Al hydrotalcite at different wt% and the sol-gel was raised to room temperature and dried. After drying the mixture was calcinated at 500 °C and 650 °C, creating nanospheroids approximately 5nm in diameter. These nanospheroid catalysts were tested in a microreactor at 800 °C for 8 hours of testing time. It was found that there was a higher conversion of methane than carbon dioxide by these catalysts with methane conversion being close to 94% for the 15 wt% catalyst. Additionally, it was found that the majority of

the coking on the catalyst was in the form of polymeric and amorphous type, which did not reduce conversion as much as whisker type coking might. This was attributed to the pore volume and stability of the hydrotalcite structure [59].

Porous nanorods of ceria supported platinum were used in high temperature dry reforming reactions by Zhang *et al.* and found to have high activity and dispersion over the surface of the nanorod. The nanorods were synthesized by mixing an aqueous solution of cerium nitrate in an aqueous solution with sodium hydroxide and autoclaving the solution at 100 °C and 1.2 atm for 24 hours. The resultant precipitate was washed and dried, and then hydrothermally treated at 160 °C for 12 hours to create the nanopores. To load the nanorods, a wetness impregnation method was used and the nanorods were dispersed in a solution of chloroplatinic acid and ethanol. This dispersion was stirred at 60 °C until the ethanol was evaporated and then dried at 100 °C and calcinated at 500 °C. The loaded nanorods were run in a dry reforming reaction under a temperature range of 500 °C to 800 °C at a rate of 5 °C per minute, while stability was tested for the catalyst at a reaction temp of 800 °C for 72 hours. The nanorods exhibited conversion rates as high as 77.3% for methane that fell only to 74.2% over the course of the stability test, while coking was determined to happen at a rate of 0.1 mg of coke per gram of catalyst per hour. This was attributed to the nanostructuring of platinum and the stability and porosity of the ceria nanorods [60].

Multiwall carbon nanotubes (MWCNT) were used as supports for a cobalt-molybdenum bimetallic catalyst for dry reforming. To create these catalysts, a sol-gel was made of cobalt nitrate, ammonium molybdate and magnesium nitrate with citric acid. The sol-gel was baked at 120 °C until dry then calcinated at 700 °C to create the catalytic

material. Then, chemical vapor deposition was used to produce MWCNTs on top of the catalytic material that then pulled the catalyst into the MWCNTs. The catalysts were tested at 850 °C for 100 hours and found to maintain a stable conversion rate of 85% for methane and 82% for carbon dioxide. This indicated a low coking on the surface of the catalytic material, due to the confinement of the nanoparticles within the MWCNTs [61].

Nanofiber meshes were used as supports for a wetness impregnation method. Dong *et al.* used an eggshell material as a nanofibrous template to create nanofibrous nickel oxide and ceria supports using a one-step process of immersing the eggshell template into a nickel and cerium nitrate solution and then heating the loaded medium to 1000 °C for 2 hours. The metal was sintered and retained the porous structure of the eggshell medium because of the medium's strong protein/metal bonding properties. This nanofiber catalyst was tested in a CPOM reaction and found to have a conversion of 98.3% for methane with a selectivity toward hydrogen of 86% [62].

More recently, electrospinning has also been used to create mesoporous supports for nanoparticle catalysts. The electrospinning process is the subject of this dissertation and is discussed in depth in chapter 3. Polyvinylpyrrolidone was used as the polymer and mixed with an organic solution of dimethylformamide and dimethyl sulfoxide as well as the silica precursor tetraethyl orthosilicate and a nickel nitrate metal precursor. The resulting sol-gel was electrospun at 15kV with an air gap of 25 cm to a grounded rotating metal drum. The nanofibers were collected from the drum and calcinated at 800 °C for 4 hours. This process led to a nanoconfined nickel nanoparticle in silica nanofibers that showed higher resistance to coking on the surface of the catalyst but only slightly higher activity than traditional nickel catalysts, with a methane conversion of 64% at 800 °C and 45% at 900 °C. This

resistance to coking was attributed to the greater level of dispersion of nickel in the catalyst [63].

Pure nickel nanofibers have also been created using an electrospinning process. In Barakat *et al.*, which studied the nickel nanofibers for their magnetic properties, polyvinyl alcohol (PVA) and nickel acetate were mixed in an aqueous solution and the resulting sol-gel was placed in a plastic capillary tube and a voltage of 20 kV was applied to the sol-gel using a copper metal pin. The sol-gel was spun onto a grounded rotating drum target. Afterward, the nanofibers were collected and dried under vacuum, and then calcinated to 800 °C under argon, yielding high purity nickel nanofibers with average diameters of 120 nm. Argon was shown to be useful to keep hydrogen from diffusing through the nickel nanofibers which would affect their magnetic properties and operational efficiency. While calcinating the nanofibers, thermal gravimetric analysis was taken of the nanofibers to determine the temperature ranges that experienced the largest loss of mass. The largest drop of mass was during the transition from 240 °C, which corresponded to an initial decomposition of PVA, with later peaks indicating decomposition of the linked acetate at 370 °C and the reduction of nickel oxide to nickel at 585 °C [64].

Nanostructured catalysts fabricated through electrospinning offer enhanced surface area and dispersion, with nanofibers made from silica showing an increased resistance to coke through the nanoconfinement of the catalytic material within the fiber. Electrospinning also offers a low cost, scalable nanomaterial synthesis technique. Many review papers have been written on the excellent properties of nanofibers synthesized through electrospinning and their applications, but while the electrospinning technique has

been used widely in fields such as biotechnology, electronics, and sensors, it is only recently being researched to create nanostructured catalysts [68-77].

CHAPTER 3

NANOFIBER METAL CATALYSTS

3.1 Introduction

Research into the dry reforming of methane is primarily focused on the refinement of catalysts due to the hurdles involved with the advancement of dry reforming as an industrial process, either as a stand-alone process or used in conjunction with other methods of reforming. These hurdles are a higher energy requirement than the industrial steam reforming reaction and the development of coke on the surface of the catalyst. To meet these needs, an electrospinning technique was used to fabricate nanofibers of nickel and nickel ferrite to act as catalysts, and magnesium aluminate to act as a catalytic support for nickel nanoparticles.

This chapter discusses the choices made in the fabrication of the nanofiber catalysts, the electrospinning technique, and the fabrication of the heterogeneous metal nanofibers. After fabrication techniques, this chapter discusses the characterization and testing done using the nanofiber catalysts in the dry reforming reaction with data gathered from an in-line gas chromatograph (GC). From the GC data, the evolution of gases at 3 different temperatures and fixed flow rates were determined and used to show reactant conversion for each catalyst at different temperatures and ultimately to determine apparent activation energies of the reactant intermediates per catalyst. Additionally, coking on the surface of

the catalyst was investigated using scanning electron microscopy to observe surface morphology of different coking types and electron dispersive x-ray spectroscopy was used to observe the changes in carbon percentages on the surface of the catalyst. Finally, the results of the coke formation tests and apparent activation energies were used to determine which nanofiber catalyst was the best for the dry reforming reaction.

3.2 Nanofiber Catalyst Fabrication

Electrospinning was chosen as a nanofiber production process for this research due to its flexibility in loading materials, in the formation of its nanofibers, and because it produces nanomaterials on an economically viable platform that has the potential to be scaled to a bulk, industrial process. The solutions can consist of any combination of materials that are needed such as metal nitrates or metal oxide nanoparticles in a polymer to create a colloidal suspension known as a sol-gel. A large amount of versatility exists in this technique. By varying parameters such as electrical charge, ambient humidity, air gap distance, and viscosity of the solution, the nanofiber's physical properties can be altered. In addition, the process is easily scalable by adding more metal nozzles and a conveyor belt-style system as the grounded target to provide a larger number of nanofibers. Due to the electrospinning process's scalability, it is the perfect technique for providing large amounts of specifically tailored catalyst on the industrial scale for use in any reaction.

3.2.1 Electrospinning Theory

First discovered in the 1960s, electrospinning has advanced as a process for the bulk production of nanofibers. A diagram of the electrospinning process is shown in **Figure 3-1**. As shown, a metal nitrate is doped into a polymer to form a sol-gel (1.) and is loaded

into a charged metal syringe (2.). A positive charge (3.) is applied by a high voltage source to the syringe tip which causes nitrates used in the metal nitrate salts to be drawn to the sidewalls of the tip (4.) while ejecting the metal ions along with the sol-gel. As the electronic forces fight the surface tension of the sol-gel, a cone forms at the tip of the syringe known as the Taylor cone (5.). From the Taylor cone, the solution is drawn out into a nanofiber straight jet (6.), and eventually the jet devolves into a whipping motion due to the chaotic forces applied by the drying of the solvent and the viscous stresses of the sol-gel (7.). Finally, the nanofibers produced from the random whipping motion are collected on a flat grounded metal surface (8.) where they can be collected [77,78].

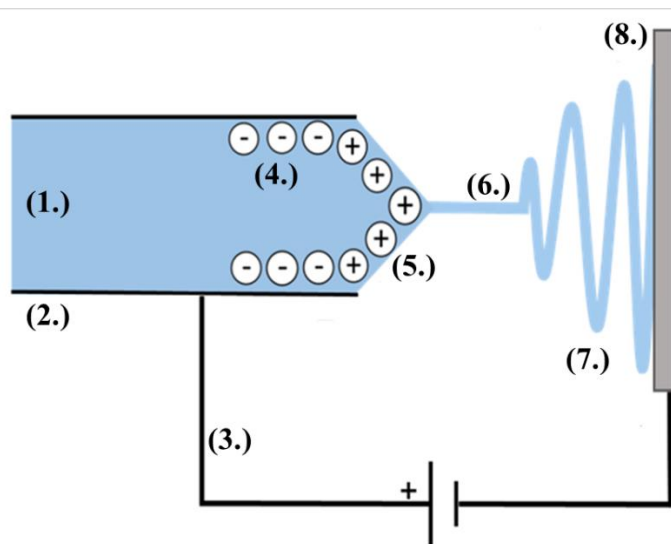


Figure 3-1: 2d schematic of electrospun fiber creation.

Electrospinning has several factors that control nanofiber growth from the syringe tip. The surface tension of the polymer fluid keeps the fluid droplets held in the Taylor cone area despite high voltages. Once the field gradient reaches a critical level at the tip of the droplet, the droplet is pulled into a straight jet from the tip of the Taylor cone. During

the straight jet mode, viscoelastic stress, surface tension, air drag, and Coulombic forces all exert themselves on the fiber, eventually causing an erratic whipping motion that is present in the whipping jet portion of the model. The parameters affecting electrospinning have been described mathematically in Angammana *et al.* as a set of equations shown in **Table 3-3**. With Q being the volume flow rate (in m/s), L is the length of the fiber, K is the conductivity of the solution (in S/m), and η_0 being the viscosity of the solution at a zero-shear rate [79].

Table 3-1: Equations describing key properties of electrospun nanofibers.

Velocity of fiber:	$v_0 = \frac{Q}{\pi L^2}$	Eq 3.1
Electrical Field:	$E_0 = \frac{I}{\pi L^2 K}$	Eq 3.2
Surface Charge Density:	$\sigma_0 = \epsilon_{air} E_0$	Eq 3.3
Viscous Stress:	$\tau_0 = \frac{\eta_0 v_0}{L}$	Eq 3.4

Other factors that influence electrospinning have been described by T. Subiah *et al.* and include; distance from the charged syringe to the collector, flow rate, humidity and other environmental characteristics around the electrospinning setup, and volatility of the solvent in the solution [80].

Efforts have been made to predict electrospun nanofiber diameter. The use of measured current from the ground target has been studied for its use in determining the diameter of the fibers during the electrospinning process [81]. Electrospun nanofibers were propelled using a DC power supply to a grounded electrode. Current measured from the electrospinning apparatus was measured from the voltage drop across a resistor in series

with the grounded plate being used as a fiber collector. This was compared to the diameter of the nanofibers being produced to determine the relationship between the current and the diameter of the nanofibers. Charge balance on the electrospun jet was determined to be:

$$I = \pi h^2 K E_1 + (2\sigma_0 Q/h) \quad Eq\ 3.5$$

where I is the total current, h is the local radius of the cross-section of the jet, K is the conductivity of the fluid, E_1 is the local electrical field strength, Q is the flow rate and σ is the surface charge density. The equation can be split into 2 parts – the conduction term and the surface charge advection term. The surface charge term becomes smaller with the smaller radius of the jet, and the advection term becomes dominant, following an ideal and linear relationship between I and Q which can be expressed as:

$$I \sim EQ^{0.5} \quad Eq\ 3.6$$

During this research, a secondary collector was placed within the electric field but shielded to not collect fibers and a current was observed on this collector. This current suggested a second polymer-free electro spray mode occurs, which contains mostly solvent implying a partial de-mixing of polymer and solvent during the extreme conditions of electrospinning. The opposite was observed to be true as well, as some areas exhibited more solvent within the nanofibers, typically seen as “beads” within the nanofibers [82].

Once deposited, electrospun nanofibers form a mesh network of randomly aligned nanofibers unless features are added to the grounded collection target. This mesh contains micro and nanopores between the nanofibers arranged, and mesopores within the nanofibers themselves. Porosity within the nanofiber mesh allows it to act as an effective platform for inclusion of catalytic material and the micropores allow the mesh to control the flow rate over the catalyst, like pores within traditional catalyst supports. The

permeance through the nanofiber mesh is a ratio of the permeability over its thickness. This permeance can be expressed via mass transfer equations and Darcy's law:

$$Q = -\frac{\kappa A(p_b - p_a)}{\mu L} \quad \text{Eq 3.7}$$

where Q is total discharge in m³/s, κ is the intrinsic permeability of the medium in m², A is the cross-sectional area, and the pressure drop before and after the mesh ($p_b - p_a$) in pascals, μ is the viscosity of the gas or liquid flowing through the mesh and L is the length of the pressure drop or in the case of a nanofiber mesh, its thickness [83].

3.2.2 Electrospun Nanofiber Fabrication

The electrospinning technique used in this research requires only a few devices for the synthesis of catalytic nanofibers. First, a polymer is loaded with catalytic and support materials made from metal or nonmetal and is then pumped at a very low but continuous rate through a charged metal syringe. The nanofibers are then electrospun across an air gap onto a stationary grounded collector where the nanofibers can then be obtained as a mesh.

Figure 3-2 shows a schematic of the electrospinning setup used in this research.

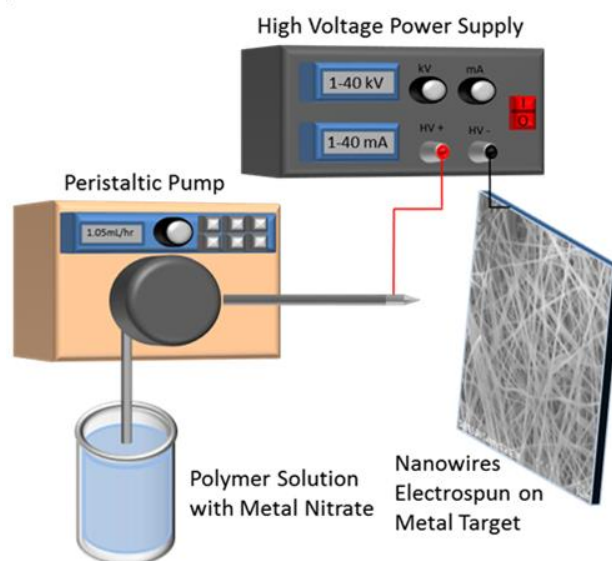


Figure 3-2: Typical electrospinning setup.

To create metal nanofibers, metal nitrate salts were mixed with aqueous polyvinyl alcohol to create a sol-gel solution. For nickel nanofibers, 5% wt nickel nitrate was added to a 15 wt% aqueous PVA solution. For magnesium aluminate oxide nanofibers, nanoparticles of magnesium aluminate were first made through a coprecipitation method and then added to the PVA solution to create a sol-gel. The sol-gel was then loaded into a peristaltic pump and pumped at a steady rate of 0.06 ml/min while a voltage of 20 kV was applied to the metal tip. The sol-gel was spun onto a grounded flat metal collector with dimensions 15 cm x 15 cm with a 12 cm air gap. The nanofibers were spun as a randomly arranged mat on the surface of the grounded metal collector. Nanofibers were then calcinated to remove the polymer medium and create a heterogeneous metal nanostructure.

In addition to nickel, nickel-iron heterogeneous nanofibers were synthesized and studied. Kim *et al* showed a reduction in coke formation due to the presence of ferrite within the nickel catalyst. The nickel ferrite catalysts have similar initial apparent

activation energies for the reactions, the main downside is the requirement of slightly more energy to begin the splitting of methane. However, the nickel-iron catalyst makes up for this initial higher apparent activation energy by cutting the energy required to split CO₂ in half compared to nickel only shown in **Table 3-4**. Not only does the nickel-iron help reduce some of the apparent activation energies for splitting carbon dioxide and the C-H bond but it can help lower the amount of carbon coke being deposited onto the catalyst surface. The iron catalyst doesn't form as much carbon coke due to its low activity with methane. By incorporating nickel with iron, the carbon formation is lowered while producing similar amounts of syngas as a product [84].

Table 3-2: Apparent activation energies for nickel and nickel-iron.

Reactions	Nickel Activation Energy	Ni-Fe Activation Energy
$\text{CH}_4(\text{g}) \rightarrow \text{CH}_3^* + \text{H}^*$	82 kJ/mol	91 kJ/mol
$\text{CH}_2^* \rightarrow \text{CH}^* + \text{H}^*$	34 kJ/mol	36 kJ/mol
$\text{CO}_2(\text{g}) \rightarrow \text{CO}^* + \text{O}^*$	58 kJ/mol	31 kJ/mol
$\text{CH}^* \rightarrow \text{O}^* + \text{HCO}^*$	142 kJ/mol	139 kJ/mol
$\text{HCO}^* \rightarrow \text{CO}^* + \text{H}^*$	21 kJ/mol	46 kJ/mol

3.3 Characterization of Nanofibers

Homogenous and heterogeneous metal nanofibers produced via electrospinning were characterized to determine their physical and chemical characteristics. To do this, the metrology lab was utilized. The Hitachi S-4800 field emission scanning electron microscope (SEM) was used for fine structure surface imaging and energy dispersive x-ray emission (EDAX) elemental composition. It was observed that the nanofibers random layering formed a tight mesh indistinguishable from a solid sheet on the macro scale. SEM

images such as **Figure 3-3** show that the nanofibers bundle together, producing a series of nanopores between the nanofibers, and mesopores within the nanofibers themselves.



Figure 3-3: Pre-calcination disordered nanofibers.

Pre-calcination, the fibers present a very smooth surface. Grains and mesopores are observed within calcinated nanofibers. **Figure 3-4** shows the grain boundaries of the crystal formation of the post-calcination nanofibers.

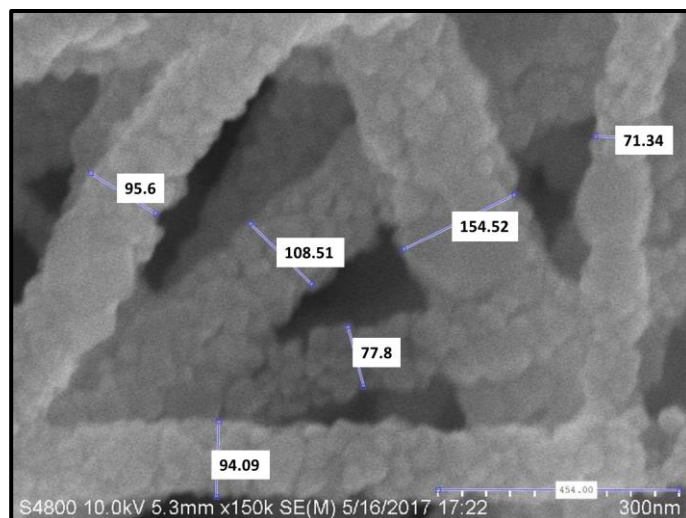


Figure 3-4: Post-calcination nanofibers with diameters shown in nanometers.

Various SEM images were used to gain more data on the nanofiber diameters both pre and post-calcination. First, images of nanofibers before calcination were taken and determinations were made on their diameter. The nanofibers were then calcinated, and SEM images were again taken and studied to determine diameter. This data was compared to the frequency of the fibers studied within several ranges. Nanofiber diameter vs appearance frequency before calcination shown in **Figure 3-5** and after calcination in **Figure 3-6** below.

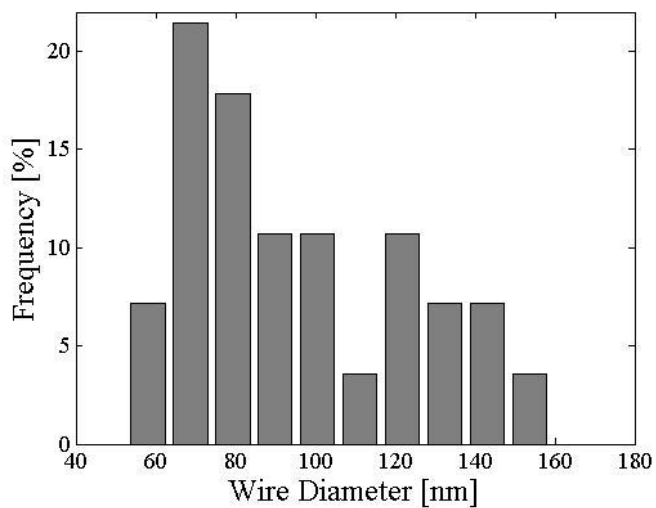


Figure 3-5: Nanofiber distributions before calcination.

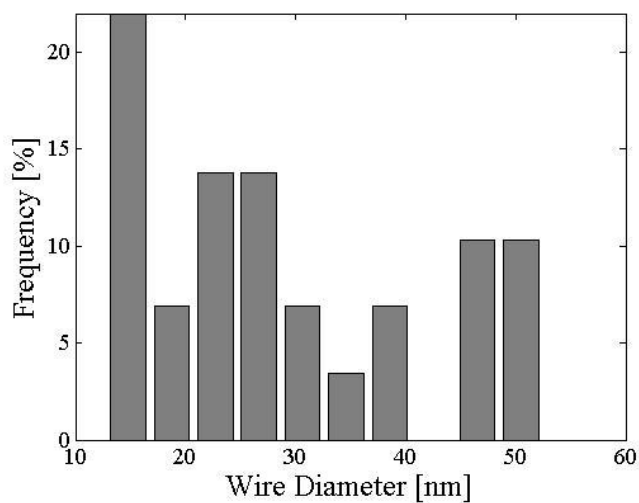


Figure 3-6: Nanofiber distributions after calcination.

Using this data, a weighted average based on fiber diameter appearing on the SEM can be determined. Average diameters from these graphs were determined to be 105 ± 32 nm before calcination and 32 ± 12 nm after calcination. The data in **Figures 3-5** and **3-6**

was compiled using several SEM images of the fibers taken at different areas of the same sample.

EDAX readings were carried out post-calcination for a determination of chemical composition. **Figure 3-7** shows the EDAX elemental analysis in graphical form, taken at 15 keV. Here, two peaks of Ni are shown while carbon and oxygen only have one. These are the $K\alpha$ and $K\beta$ lines corresponding to the K shell of nickel.

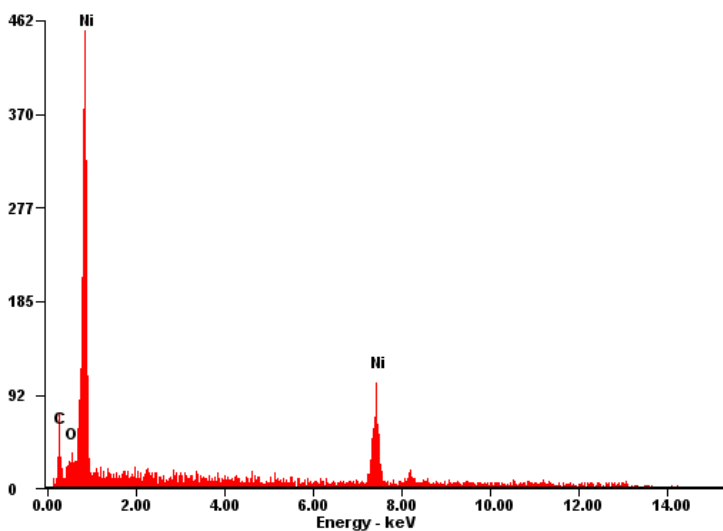


Figure 3-7: EDAX elemental analysis graph of pre-calcination nanofibers.

Here it can be seen there is a level of carbon still after the initial drying of the sample due to the polymer content. After EDAX of the sample, it was calcinated at 550 °C and then measured again. **Figure 3-8** shows post-calcination of the nanofibers.

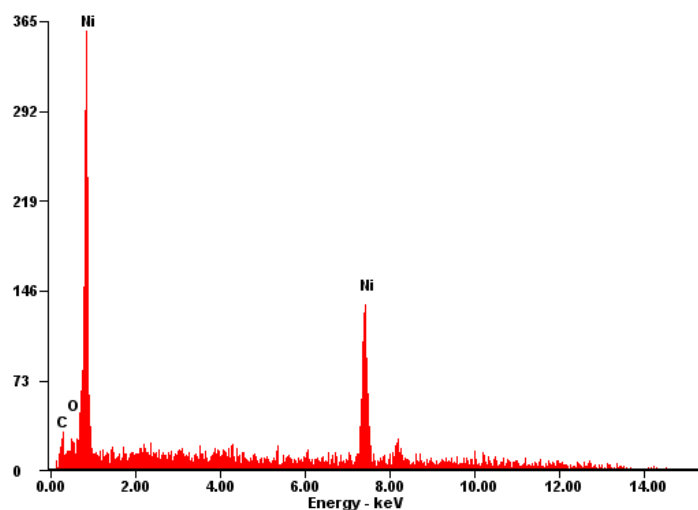


Figure 3-8: EDAX elemental analysis graph of post-calcination nanofibers.

Table 3-5 shows the numerical distribution of the elements detected through the EDAX process for the figures. Post-calcination, the nanofibers were determined to have nearly 95 wt% as nickel oxide or pure nickel.

Table 3-3: EDAX elemental distributions pre and post calcination.

Element	Pre Cal Wt%	Post Cal Wt%	Pre Cal At%	Post Cal At%
C	22.32	5.62	55.49	16.2
O	3.69	17.86	6.88	38.66
Ni	73.99	76.52	37.63	56.88

3.4 Quantification of Reaction Efficiency

Gas chromatography is a method that measures the time taken by test gases to travel through a chemically active medium. This test is primarily for testing the amount of analyte in a mixture. A schematic of the setup is shown in **Figure 3-9**. The device used for this purpose was an SRI 8610C in line to the thermal plug flow reactor from MTI Corp (**Figure**

3-10). This setup allows for direct analysis of products on stream from the reaction space. The gas chromatograph (GC) is useful because it allows us to quantify the gas created in the reactor and analyze products from reactions that have taken place within the reaction space.

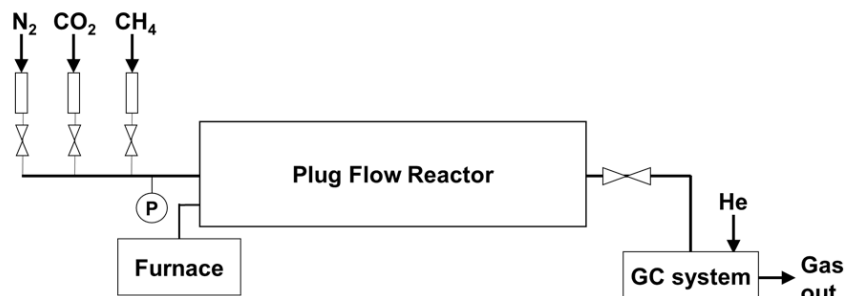


Figure 3-9: Schematic of reaction space with the GC system.



Figure 3-10: Thermal plug flow reactor (GSL-1500X MTI Corp.) with in-line GC (SRI 8610C, SRI Corp).

The plug flow reactor requires a build up to reach set temperatures with 20-minute intervals at 200 °C, 600 °C and 800 °C in order to keep from inducing thermal stress on the reactor tube. This necessitates a ramp-up time of at least 140 minutes. Additionally, the cooldown of the reactor must not exceed 5 degrees per minute so the ramp down time also

typically takes 130 minutes. When the reactor is initially activated, an inert gas is flowed through the reactor such as nitrogen or argon to keep the pressure in the reactor stable.

Products are analyzed by the GC and are read as peaks on the software accompanying the GC. Peaks are based on elution time, or amount of time it takes for the gas to pass through the active material in the GC column, as the X-axis and response factor measured in the Y axis. To translate response factor from the GC into an amount of product (ie, quantitation), analysis of the data uses the area of the peak or height of the peak to determine amount from response factor. Simple area analysis assumes that the GC itself responds identically to all analyte gases and thus is only used for rough estimation. There are two ways to accurately determine the amount, the first using an external standard, and the second using an internal standard. External standards use a sample of known amounts to the analyte to record the response factor from this known. The response factor of the external standard is then compared to the analyte needing to be analyzed to determine the amount of analyte. The two basic equations associated with external standards are:

$$\text{response factor} = \frac{\text{peak area}}{\text{analyte amount}} \quad \text{Eq 3.8}$$

$$\text{analyte amount} = \frac{\text{peak area}}{\text{response factor}} \quad \text{Eq 3.9}$$

External standards are useful if the analysis is using similar conditions for each sample.

Internal standards are useful for testing samples across multiple conditions and use a specific standard that has a predictable performance. An internal standard is a gas that does not interact with the reaction and is available in a known amount during the entire measurement period. This internal standard is then compared against all other analytes.

Like the external standard method, this can be done with multiple analytes but does not need multiple knowns for analysis. The equations associated with this method are:

$$\text{response factor} = \frac{\text{Area of I.S.} \times \text{amount of analyte}}{\text{Amount of I.S.} \times \text{area of analyte}} \quad \text{Eq 3.10}$$

$$\text{Amount of analyte} = \frac{\text{amount of I.S.} \times \text{area of analyte} \times \text{R.F.}}{\text{Area of I.S.}} \quad \text{Eq 3.11}$$

where I.S. is internal standard and R.F. is response factor. Analysis of specific products and reactants of the DRM reaction was done using an external standard, which used calibration gas mixtures provided in known quantities (Gasco) as standards. These analytes were tested by flowing the gas through the heated reactor for the most accurate readings.

After the internal standards are quantified, the same equation can be used to find the unknown amounts of products and reactants from the GC. Internal standards are more accurate than external standards due to the small discrepancies in gas amounts associated with the gas sampling mechanism in the gas chromatographs, which external standards cannot account for. This makes the use of an internal standard optimal when volume errors can occur unknowingly. In this research, nitrogen was used to control the flow rate and create an internal standard that was used in the calculation of concentration, conversion, and apparent activation energy. Space velocity was also calculated by the generally accepted equation:

$$\text{GHSV} = \frac{Q}{V} \quad \text{Eq 3.12}$$

where GHSV is the gas hourly space velocity, Q the total volumetric flowrate and V the bulk volume of the catalyst bed. As initial mass flow was kept constant during all testing, the space velocity was found to be 658.8 /hr or 10.98 /min. To study the dry

reforming reaction using a variety of nanostructured catalysts, an internal standard was used based on the inert gas nitrogen.

Average conversion rates for the reactant gases were calculated based on the percent difference between the inlet flow and the measured outlet flow for each of the catalysts [87]. To determine the conversion percentage, equations 3.13 3.14 and 3.15 were used:

$$\chi_{CH_4} \% = \frac{(F_{CH_4in} - F_{CH_4out})}{F_{CH_4in}} \times 100 \quad Eq\ 3.13$$

$$\chi_{CO_2} \% = \frac{(F_{CO_2in} - F_{CO_2out})}{F_{CO_2in}} \times 100 \quad Eq\ 3.14$$

where F_i is the flow rate of each component gas determined by

$$F_i = F_{total} \chi M f_i \quad Eq\ 3.15$$

where F_{total} is the total flow rate and Mf_i is the molar fraction of component i .

3.4.1 Nickel Catalyst Tests

To test a traditional nickel crystal catalyst, a 6 ml aqueous solution of 20% wt nickel nitrate hexahydrate (Alfa Aesar) was added to 3.5 grams of γ -alumina support pellets that have a pore volume of 0.77 cc/g and a median pore diameter of 130 Å. These were then heated to 100° C and allowed to dry. Once dry, the pellets were calcinated in a burnout furnace that built up to 500° C in 1 °C/min increments until 100° C and then 0.5 °C increments from 100° to 500° C and then allowed to cool naturally. To prepare the nanofiber catalysts, the nanofibers were crushed in their calcinated state and water was added to create a paste which was then coated onto γ -alumina support pellets. This method was used to eliminate loss of lightweight nanofibers and to keep any background the same between catalytic materials. These pellets were then dried and re-calcinated. After this,

they were loaded into the reactor and tested at different temperatures. The setpoint temperatures were 700 °C, 800 °C and 900 °C, and each run was held at these setpoints for between 2 and 3 hours a piece. Before the setpoint was reached, the reaction gases CH₄ and CO₂ were introduced into the reactor. The evolution of gases for a pure nickel catalyst can be seen in **Figure 3-11** below. Gas chromatograph measurements were taken at 15 to 30-minute intervals.

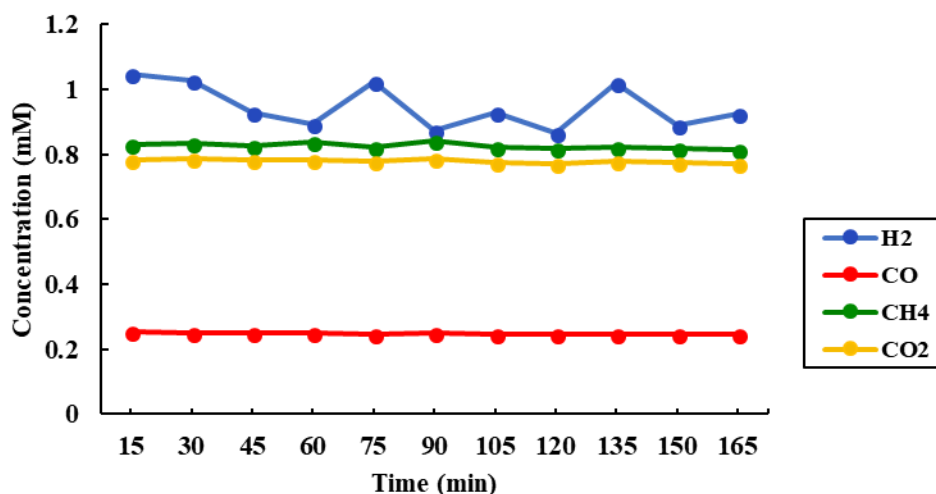


Figure 3-11: Gas evolution over traditional Ni catalyst at 700 °C.

As shown in **Figure 3-11**, the conversion ratio for methane is 58.28% and carbon dioxide is lower at 50.63%. Production of carbon monoxide was a steady 2.48 mM on average. The ratio of reactant gases for testing of nickel catalyst was set at 1.5:1 for CO₂:CH₄. First, the catalyst was tested at 700 °C and then afterward it was tested at 800 °C, and the evolution of the reaction and product gases can be seen in **Figure 3-12**.

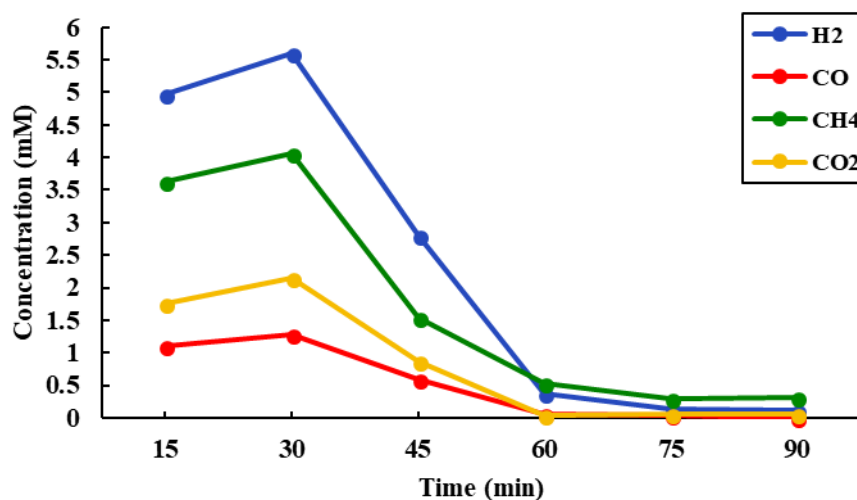


Figure 3-12: Gas evolution over traditional Ni catalyst at 800 °C.

As can be seen in **Figure 3-12**, the reactant gases both drop significantly during the measurement period: methane was shown to be reduced from 4 mM to 0.3 mM and carbon dioxide was shown to be reduced from 2.1 mM to 0.05 mM while the product gases are also reduced. This indicates the introduction of coke onto the catalyst, deactivating nickel sites in the alumina pellet which reduced the output of reactant gases by 97.6% for hydrogen and 99% for carbon monoxide. **Figure 3-13** below shows reactant and product gases at 900 °C.

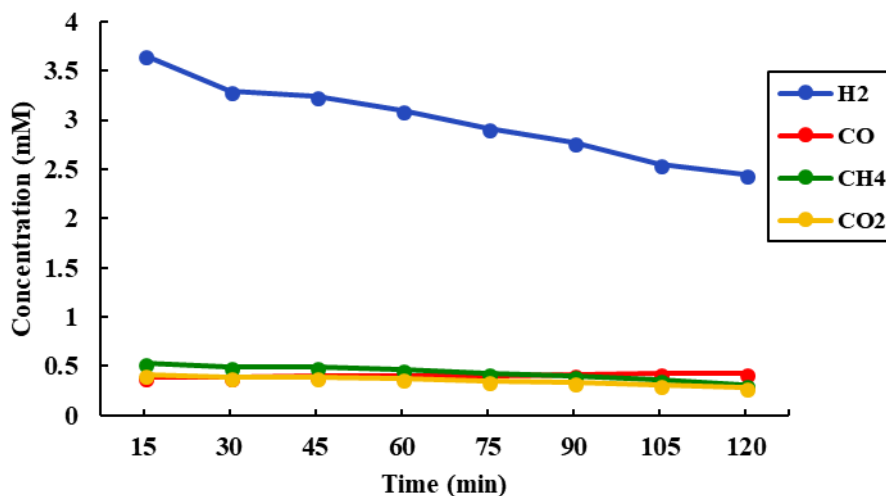


Figure 3-13: Gas evolution over traditional Ni catalyst at 900 °C.

As shown in **Figure 3-13**, hydrogen gas begins at 4.26 mM but falls over time to 2.75 mM, about 0.5 mM less hydrogen produced than at the beginning of the 800 °C run. Carbon monoxide production increases much more slowly with a difference of 11% from beginning to end, suggesting a slow shift towards deactivation. To study the carbon formation on the surface of the catalyst, the scanning electron microscope was used along with energy dispersive spectroscopy to determine carbon morphology and wt% of carbon on the surface of the catalyst. **Figure 3-14** shows the surface of the catalyst after 3 hours of reaction.

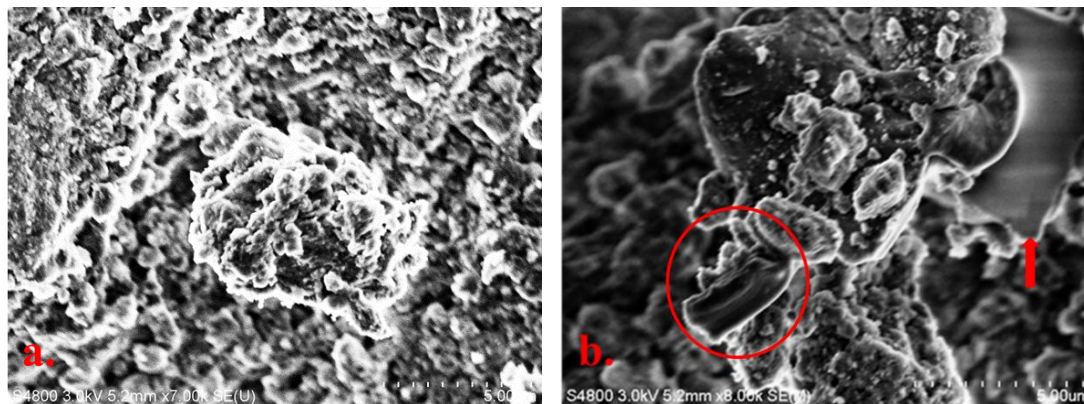


Figure 3-14: SEM of traditional Ni catalyst after 3 hours on stream with a.) nickel particles and b.) coke formation.

Shown in **Figure 3-14**, the nickel is quite visible on the surface of the catalyst as small dots along the surface. There is some carbon on the surface of the catalyst, but it is a small amount and only visible in the second image as dark glassy amorphous structures seen in **Figure 3-14 b**. The 3-hour on stream sample was then analyzed with electron dispersive spectroscopy to determine the amount of carbon coking that occurred on the surface of the catalyst. This is shown in **Figure 3-15**.

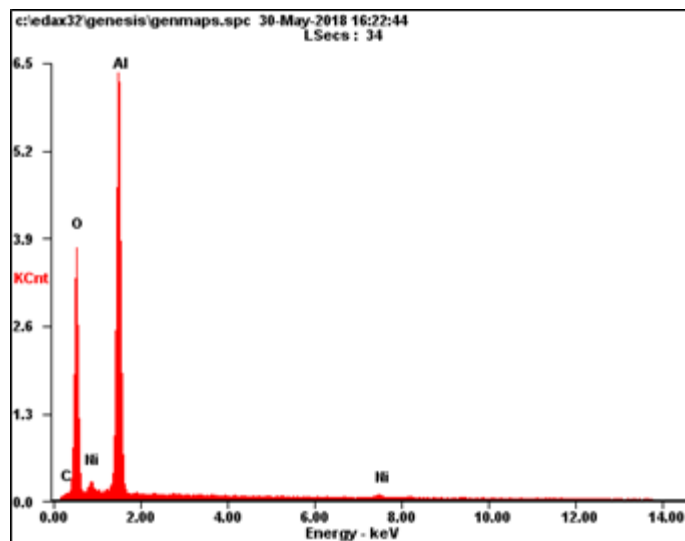


Figure 3-15: EDAX of traditional nickel catalyst after 3 hours on stream.

Here, carbon is only at 3.97 %wt while the aluminum and oxygen peaks dominate. The at% ratio for aluminum and oxygen is 2:3, (36.55 at% to 55.12 at%) and as the support is made of γ -alumina in the form of Al_2O_3 , this means the pellet accounts for all the aluminum and oxygen in the sample. Nickel content within the sample was 5.48 %wt.

To better explore the effects of coking on the catalysts, the pellets were further studied at 9 hours on stream and 15 hours on stream studied under SEM and EDAX methods were used to determine carbon content of. **Figure 3-16** shows nickel carbide buildup on the pellet surface after 9 hours.

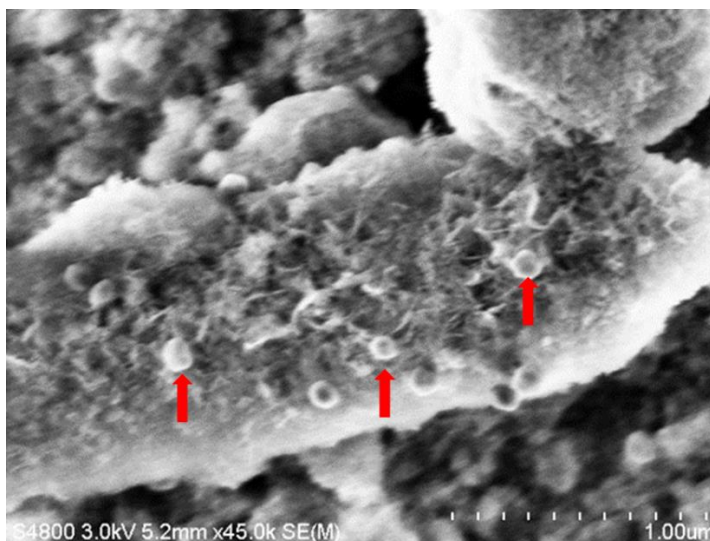


Figure 3-16: Traditional nickel catalyst after 9 hours showing carbide formation.

Here it can be seen that there are small nodules on the surface which are nickel carbide clumps on the surface of the catalyst. The difficulty in getting a direct close image is due to a combination of the carbon buildup and the magnetic nature of pure nickel. Elemental analysis using EDAX spectra was obtained for the 9-hour to determine carbon content and is shown in **Figure 3-17**.

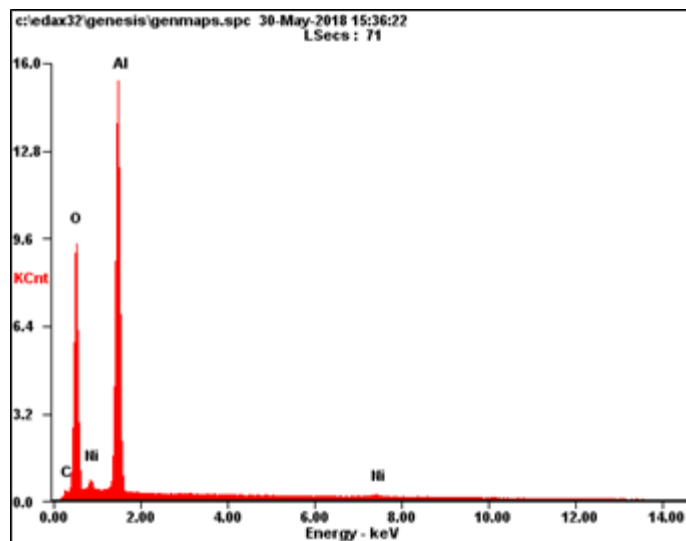


Figure 3-17: EDAX of traditional Ni catalyst after 9 hours on stream.

As can be seen, the carbon buildup on the surface of the catalyst has increased by 36.58% from the 3-hour on stream sample. The EDAX also picks up a large amount of aluminum and oxygen, which is due to the γ -alumina pellet that is the support. In order to continue the study of coke formation on the Ni catalyst, the pellets were run for 6 more hours at 800 °C at the same space velocity, and mass flow of reactants. After 6 hours, the catalyst was again studied under the SEM and EDAX. **Figure 3-18** shows the surface of the pellet after 15 hours on stream.

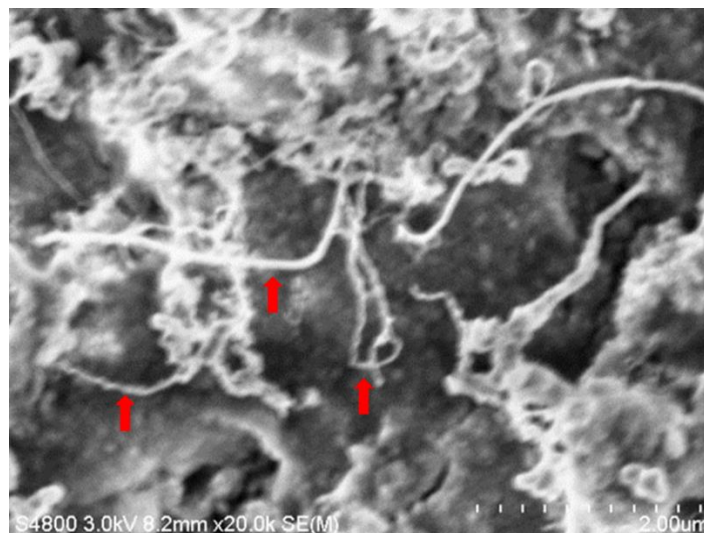


Figure 3-18: SEM of traditional Ni catalyst after 15 hours on stream showing whisker formation.

As shown in **Figure 3-18**, coking has covered most of the metal particles visible on the surface as dark sheets. Additionally, carbonaceous whisker formation can be seen on the surface of the catalyst as bright tangled ribbons in the SEM image, highlighted by the red arrows. After SEM imaging, the catalyst was measured under EDAX. The results are displayed below in **Figure 3-19**.

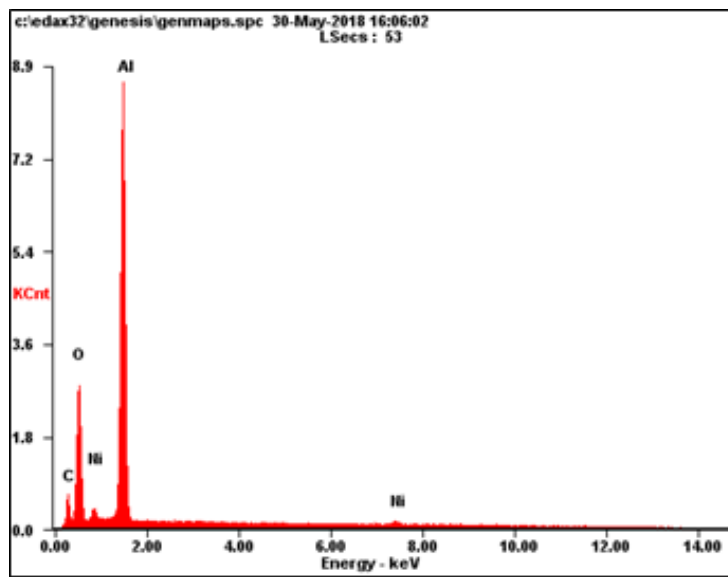


Figure 3-19: EDAX of traditional Ni catalyst after 15 hours on stream.

The 15-hour EDAX of the nickel catalyst shows much more carbon growth on the surface of the pellet. The atomic ratio of carbon to nickel has become very high, with almost 18 times as much carbon on the surface of the pellet as nickel. The atomic percent and weight percent of nickel and carbon for each of the three tested run times are listed below in **Table 3-6**.

Table 3-4: Nickel and carbon formation of traditional nickel catalyst on γ -alumina pellet After 3, 9, and 15 hours on stream.

Element	3 Hours wt%	3 Hours at%	9 Hours wt%	9 Hours at%	15 Hours wt%	15 Hours at%
Nickel	5.28	1.85	5.52	1.92	5.91	1.89
Carbon	3.97	6.75	6.26	10.27	21.03	32.92

As seen in **Table 3-6**, the measured nickel remains nearly constant across the pellets with only 3.71 at% change over the different samples, while carbon buildup increases. The

atomic percent change between in carbon on the surface of the pellet from 3 hours and 15 hours is a startlingly 387.7%, suggesting severe coking of the catalysts after 15 hours. A visual inspection of the pellets taken at 3, 9 hours and 15 hours shows the buildup of coke on the surface of the catalyst. This is shown in **Figure 3-20** below. The visual inspection of the pellets shows the increasingly darker colors of the pellet indicating carbon growth.

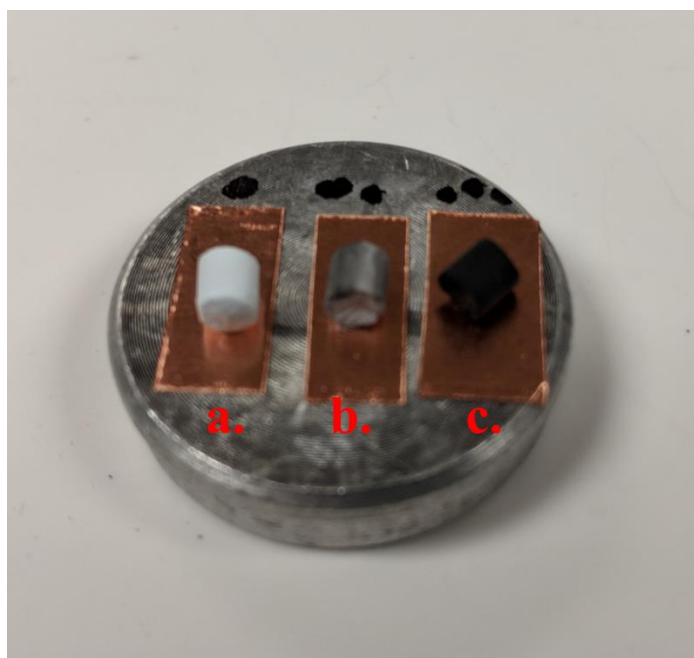


Figure 3-20: Visual inspection of the traditional nickel catalyst at (a.) 3, (b.) 9 and (c.) 15 hours on stream.

3.4.2 Nickel Ferrite Nanofiber Catalyst Testing

After nickel catalysts were prepared and tested, nickel ferrite nanofiber catalysts were prepared and tested. Nickel ferrite heterogeneous catalysts were prepared using an electrospinning technique. The catalyst was made by adding nickel nitrate and ferric nitrate to an aqueous PVA solution at two different amounts, with the total mass of the metal

nitrates included in the solution set at 5 grams. This solution was mixed for 5 hours until a sol-gel was formed and then electrospun at 20 kV and 12 cm between the syringe tip and the target. The first nickel ferrite catalyst had amounts set at 80% Ni and 20% Fe after calcination, while the second used a formulation of 50/50 nickel and iron. The NiFe nanofiber catalyst was tested by crushing the calcinated nanofibers and adding a small amount of water to create a slurry and coating the γ -alumina pellet support with the slurry. The slurry was then placed in an oven at 100 °C under vacuum until dry. This catalyst was tested in a similar manner to the nickel catalyst, first at 700 °C, then 800 °C then 900 °C. The evolution of gases over time was measured at each set point. **Figure 3-21** shows the evolution of gases over the NiFe nanofiber catalyst at 700 °C.

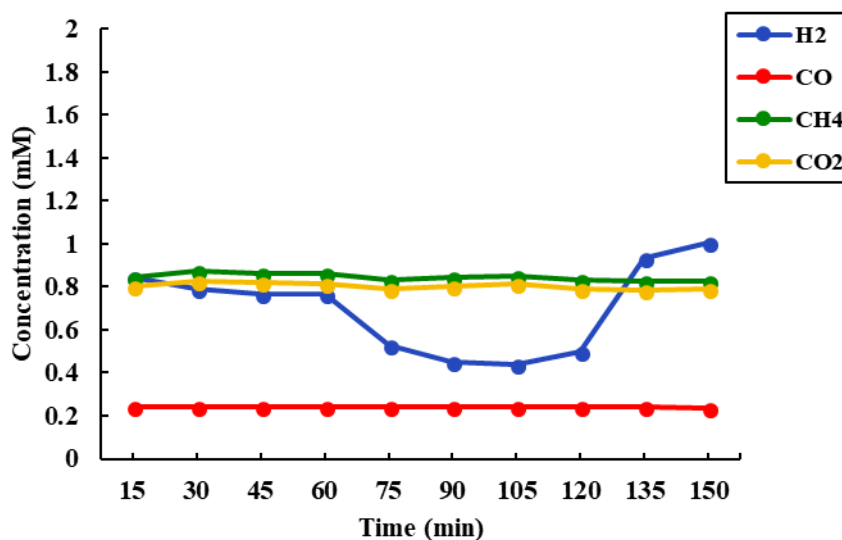


Figure 3-21: Gas evolution over NiFe 2:1 nanofiber catalyst at 700 °C.

Like the pure nickel catalyst at 700 °C, the concentration of carbon dioxide is higher than carbon monoxide and hydrogen, with methane at an average concentration of 0.845

mM and at a conversion of 57.35 % on average which is only .93 % lower than the average conversion of methane over the pure nickel catalyst. **Figure 3-22** shows the evolution of gases over time at 800 °C.

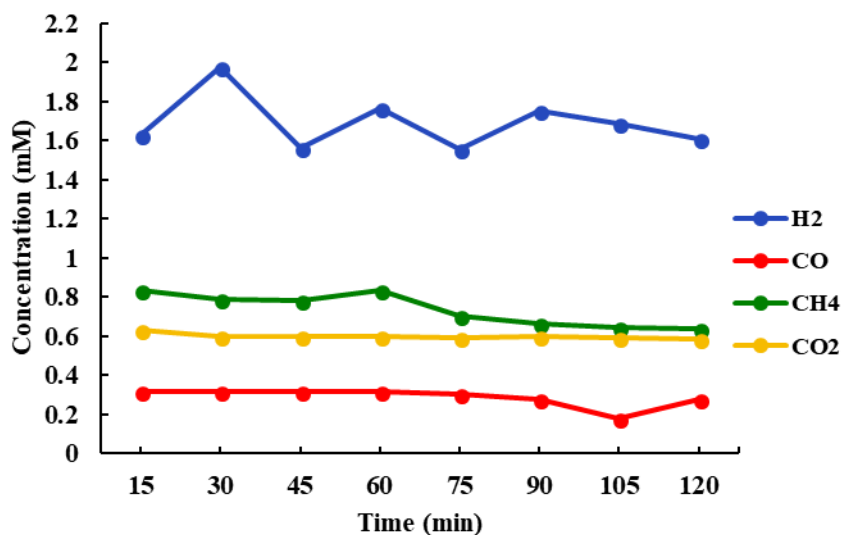


Figure 3-22: Gas evolution over NiFe 2:1 nanofiber catalyst at 800 °C.

At 800 °C, methane conversion is an average of 7.54 % higher than at 700 °C, with the concentration of methane falling after an hour of run time by 0.13 mM, indicating a shift towards methane consumption or a replenishment of the nickel active sites on the catalyst. A difference in average concentration of carbon dioxide between the 700 °C run and the 800 °C of 0.21 mM which shows a higher consumption of carbon dioxide at this temperature for this catalyst. Hydrogen production is also much higher, by an average of 1 mM from the 700 °C run, which is partially due to the higher temperatures lowering the hydrogen consumed by the water gas shift reaction. **Figure 3-23** shows the gas evolution over the same NiFe nanofiber catalyst at 900 °C.

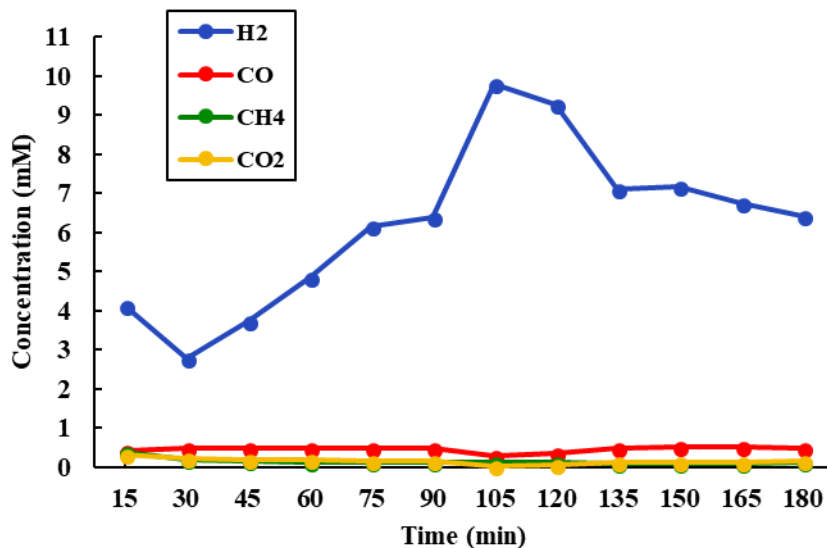


Figure 3-23: Gas evolution over NiFe 2:1 nanofiber catalyst at 900 °C.

As shown in **Figure 3-23**, the conversion percentage of methane is almost complete at an average of 92.88% conversion and a difference from the inlet flow and an average concentration of 0.11 mM. Hydrogen sees a jump in concentration from 6.36 mM to 9.78 mM briefly which then falls to 6.4 mM at the end of the test period. These increases and decreases in hydrogen production are accompanied by a carbon dioxide concentration decrease during the same period from 0.154 mM to 0.0285 mM. Due to the decrease of carbon monoxide concentration from 0.475 mM to 0.272 mM, while the methane concentration increases by only 0.02 mM, it is assumed that this is due to the deactivation and redox reaction loop between the nickel and the iron active sites.

For the 1:1 ratio nickel ferrite, reaction tests followed the same procedure as nanofibers were crushed in made into a slurry using water and then absorbed onto the

surface of 3.5 grams of γ -alumina pellets. The first reaction test at 700 °C for the 1:1 ratio of nickel and iron is shown below in **Figure 3-24**.

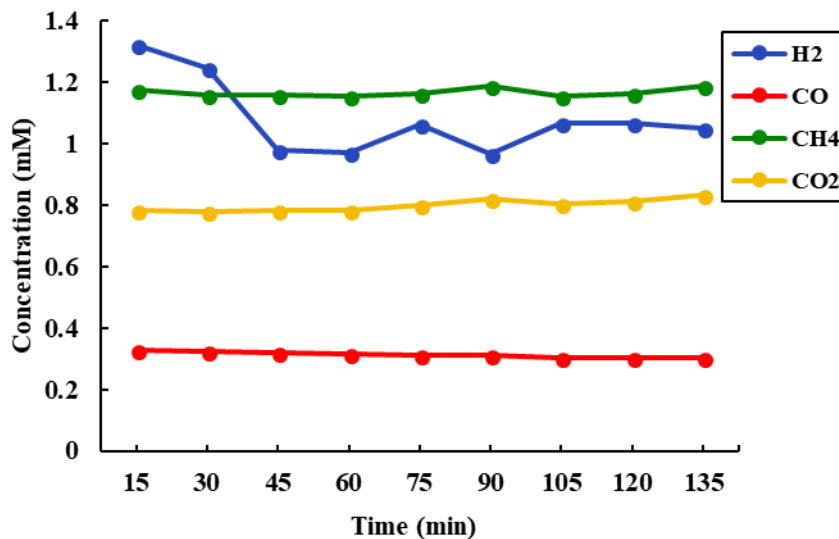


Figure 3-24: Nickel ferrite 1:1 ratio nanofiber catalyst gas evolution at 700 °C.

As seen in **Figure 3-24**, average concentration for methane is 0.345 mM higher while carbon dioxide is 0.04 mM lower than the average for the 2:1 NiFe catalyst at the same temperature, indicating a slight preference towards carbon dioxide due to the larger amount of iron in the catalyst. Carbon monoxide production correspondingly higher for the 1:1 NiFe catalyst with an average concentration measured of 0.31 mM as opposed to 0.24 mM. As carbon monoxide is the product of the iron redox reaction, this shows the effect of the additional iron on the nickel catalyst at a lower temperature. Next, the gas evolution for NiFe 1:1 catalysts are shown at 800 °C in **Figure 3-25**.

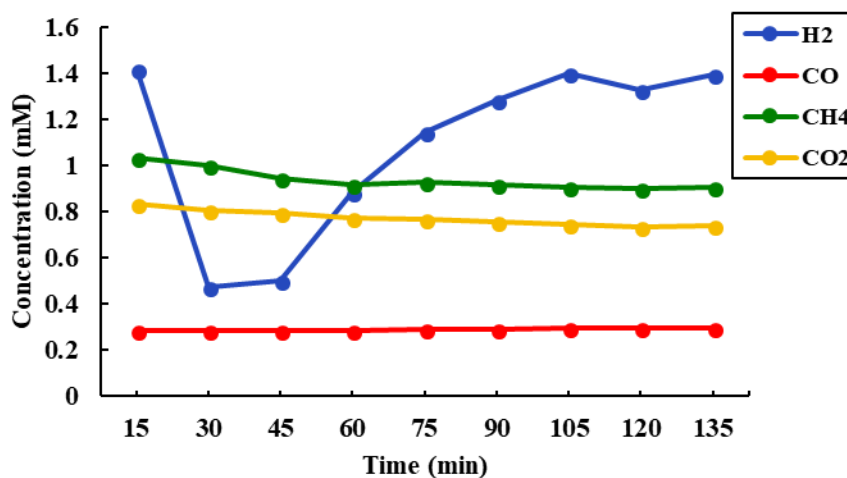


Figure 3-25: Nickel ferrite 1:1 nanofiber catalyst ratio catalyst gas evolution at 800 °C.

As shown in **Figure 3-25**, as time progresses the methane and carbon dioxide show a small decrease in concentration while hydrogen initially starts at 1.42 mM but drops in concentration to 0.475 mM and then climbs up to 1.4 mM over the course of the testing period. This recovery indicates that the iron is replenishing the nickel catalyst through the redox side reactions. This can be shown by the fact that the carbon monoxide product slowly increases by 5.44% during the runtime due to the carbon monoxide produced by the redox reaction from the iron. Finally, **Figure 3-26** shows the evolution of gases at 900 °C for the Ni:Fe 1:1 catalyst.

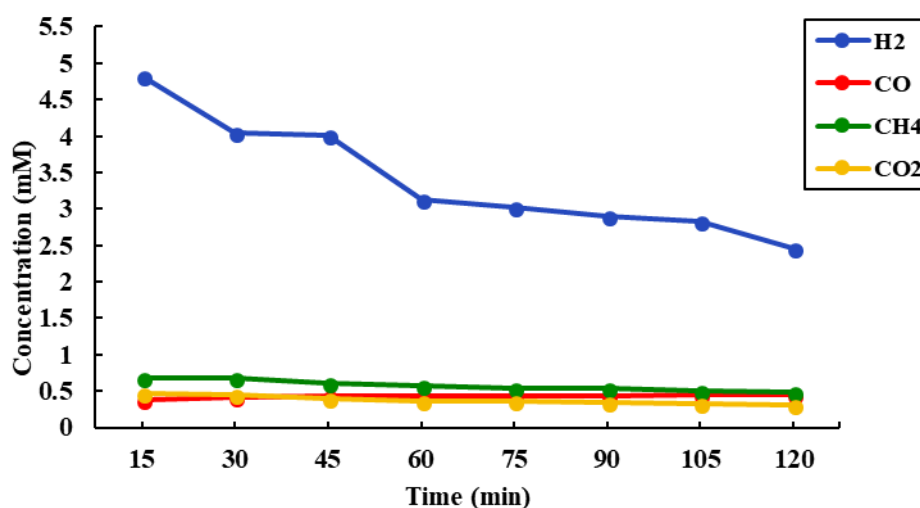


Figure 3-26: Nickel ferrite nanofiber catalyst 1:1 ratio catalyst gas evolution at 900 °C.

During this testing period, the hydrogen production started extremely high at 4.82 mM and fell slowly over the course of the run to 2.45 mM. This was accompanied by a rise in the CO production by 20% over the course of the run. Both methane and carbon dioxide follow similar paths of decline each losing 0.236 mM of methane and 0.148 mM of carbon dioxide over the course of the testing period, both close to a 30% loss of reactant. While the decrease in hydrogen indicates a deactivation of the nickel active sites on the catalyst, the small increase in the carbon monoxide indicates that there are many active iron sites still on the catalyst.

In order to examine the coking of the nickel ferrite nanofiber catalysts, they were studied under SEM and EDAX. To do this, the pellets were cut to produce a flat side to assist with the adhesion to the SEM imaging platform. The nickel ferrite catalysts were studied before reaction, and at the 9-hour and 15-hour marks. The SEM image (**Figure 3-**

27) shows the nickel ferrite 2:1 catalyst before being placed in the reactor while the EDAX of the initial sample is shown in **Figure 3-28**.

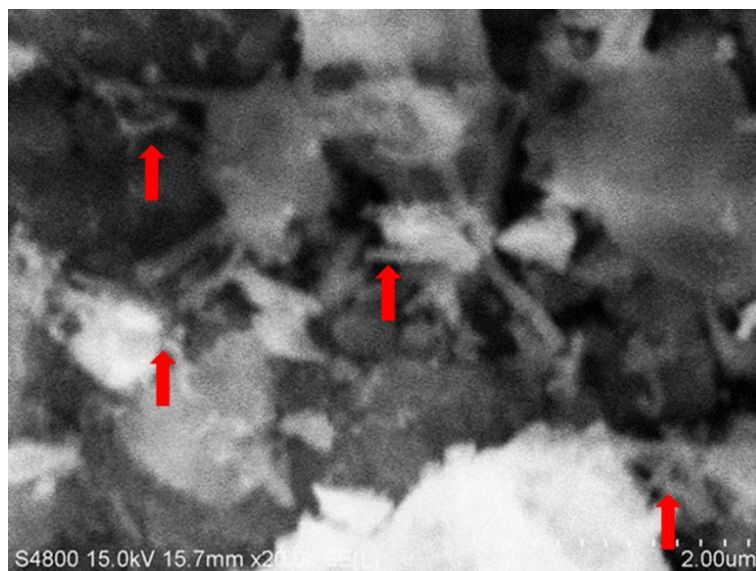


Figure 3-27: SEM image of NiFe nanofiber catalyst 2:1 before the reaction showing single nickel ferrite nanofibers and clusters (arrows).

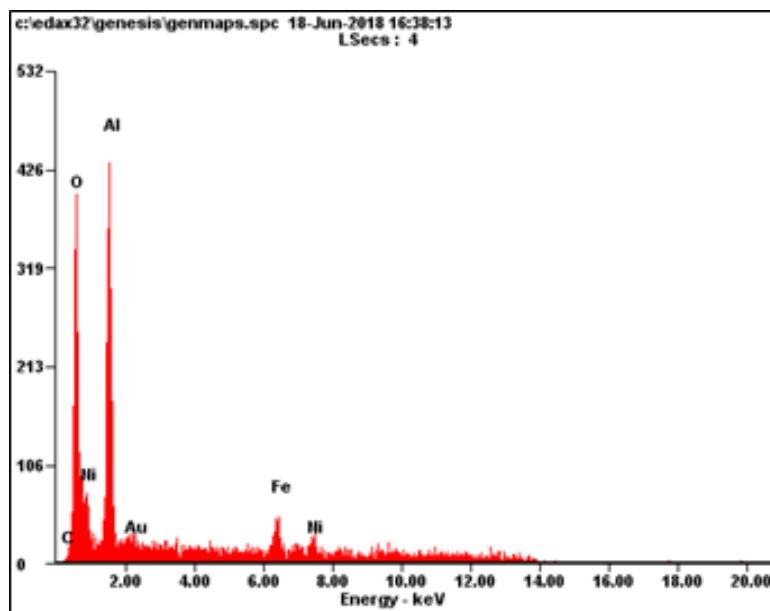


Figure 3-28: EDAX analysis of NiFe 2:1 nanofiber catalyst before reaction.

Shown in **Figure 3-28**, the nanofiber catalyst has been broken up and loaded into the alumina pellet, with the nanofibers visible on the surface of the pellet as shown by the red arrows. The EDAX shows a Ni L peak close to the oxygen peak and K and Kb peaks after the Fe K peak, with an initial at% of nickel is detected as 11.77 for this area. Here, the carbon in the analysis is low and due to the calcination process of the nanofibers. After 9 hours of reaction time, a sample was taken from the pellets and SEM imaging and EDAX analysis were performed on that sample. **Figure 3-29** and **Figure 3-30** show the SEM imaging and EDAX analysis of the 9-hour sample.



Figure 3-29: SEM image of NiFe nanofiber catalyst 2:1 after 9 hours on stream showing nickel carbides (arrows) and clusters of nanofibers (circle).

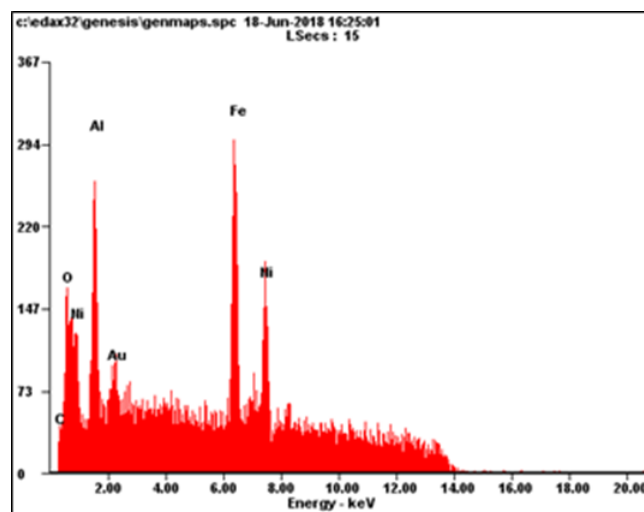


Figure 3-30: EDAX analysis of NiFe nanofiber catalyst 2:1 after 9 hours on stream.

Due to coking, individual nanofibers are difficult to detect under scanning electron microscope imaging after 9 hours. The nickel ferrite can still be seen as bright clusters on the surface of the pellet, shown by the red circle, with carbides showing up as spherical bright spots on the surface of the catalyst as seen by the red arrow. Additionally, due to the magnetic field coming from the nickel and iron blend, gold was introduced to assist FESEM imaging, however, there was still noise in the EDAX for the 9 and 15-hour catalyst images. After 15 hours of runtime, a sample was taken and imaged under SEM and EDAX. This is shown in **Figure 3-31** and **Figure 3-32**.

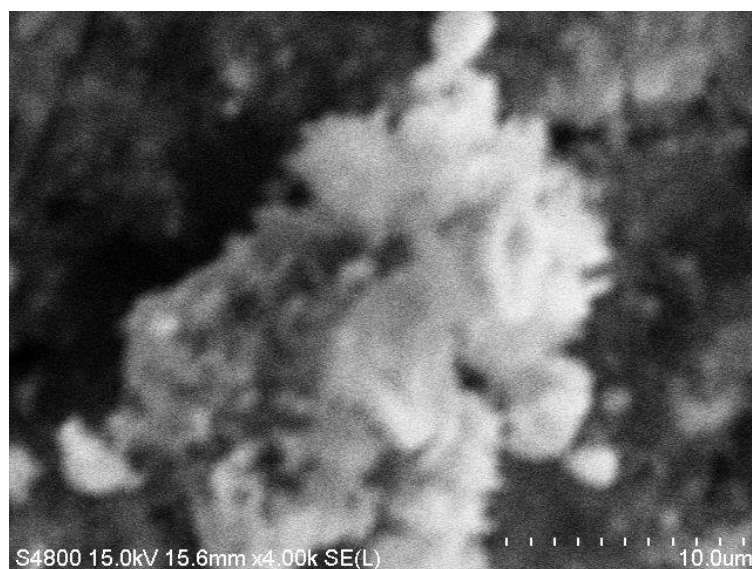


Figure 3-31: SEM image of NiFe nanofiber catalyst 2:1 after 15 hours on stream.

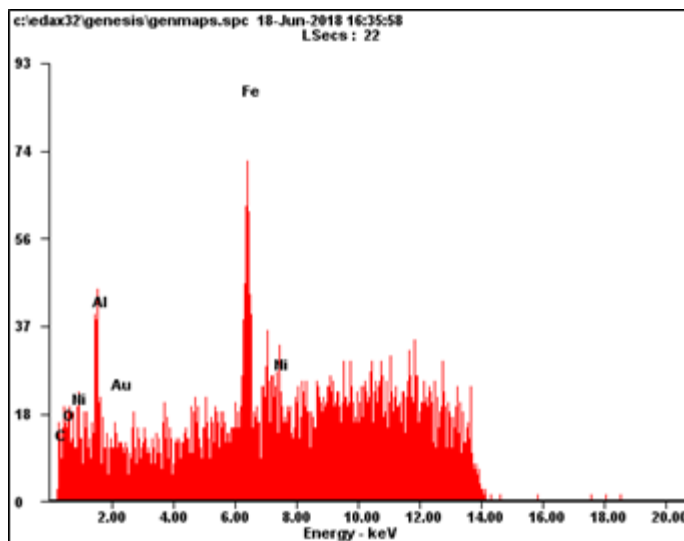


Figure 3-32: EDAX analysis of NiFe nanofiber catalyst 2:1 after 15 hours on stream.

After 15 hours, clusters of nickel ferrite nanofibers are still seen on the surface of the pellet. The bright spheres are indicative of nickel carbide while there was no whisker growth found. Carbon growth is shown in the darker area to the left of the catalyst cluster.

Figure 3-33 shows a visual inspection of the catalysts before they were studied. The progressive darkening of the catalyst shows the increased coking at each stage.

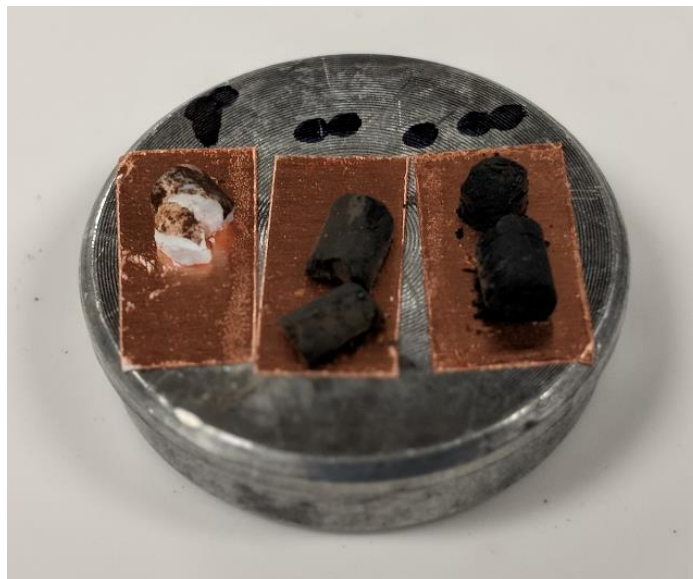


Figure 3-33: Visual inspection of NiFe 2:1 nanofiber catalyst.

The NiFe 1:1 nanofiber catalysts were run studied in a similar process to the NiFe 2:1 nanofiber catalysts. First, the initial pellet was image and studied under EDAX elemental analysis. These images are shown in **Figure 3-34** and **Figure 3-35**.

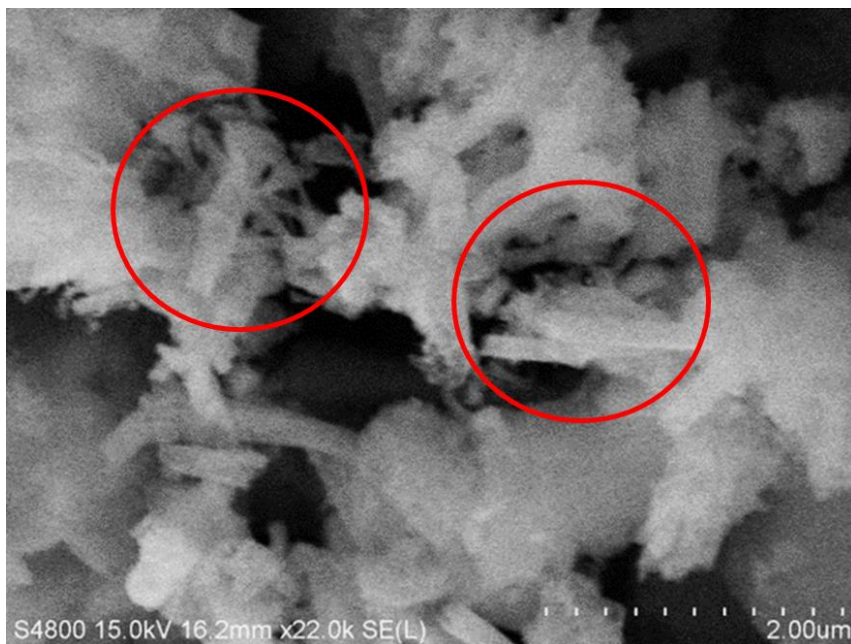


Figure 3-34: SEM imaging of NiFe 1:1 nanofiber catalyst before reaction showing nickel ferrite nanofiber clusters (circles).

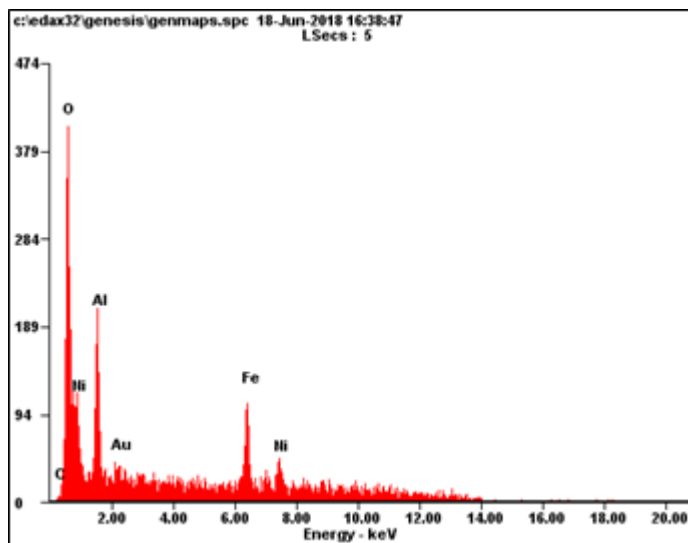


Figure 3-35: EDAX analysis of NiFe 1:1 nanofiber catalyst before reaction.

As with the NiFe 2:1 nanofiber catalyst, the NiFe 1:1 nanofibers were crushed and made into a slurry with water. Afterward, they were coated onto the pellet through a wetness impregnation method. This SEM image shows a multitude of fibers that have been broken up from their pre-calcinated states as shown by the red circles. Carbon is measured at 2.54 wt% while nickel was measured in the clusters as 21.63 wt%. SEM and EDAX analysis were taken at the 9-hour mark for the NiFe 1:1 nanofiber catalysts as well. These images are shown in **Figure 3-26** and **Figure 3-27**.

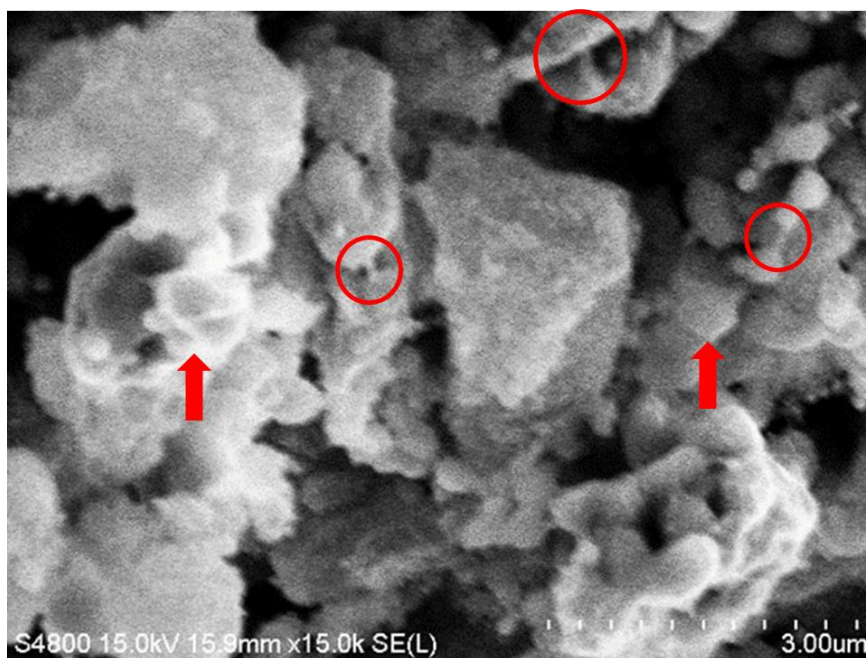


Figure 3-36: SEM imaging of NiFe 1:1 nanofiber catalyst after 9 hours of reaction showing nickel carbides (arrows) and nanofibers connecting the carbides (circles).

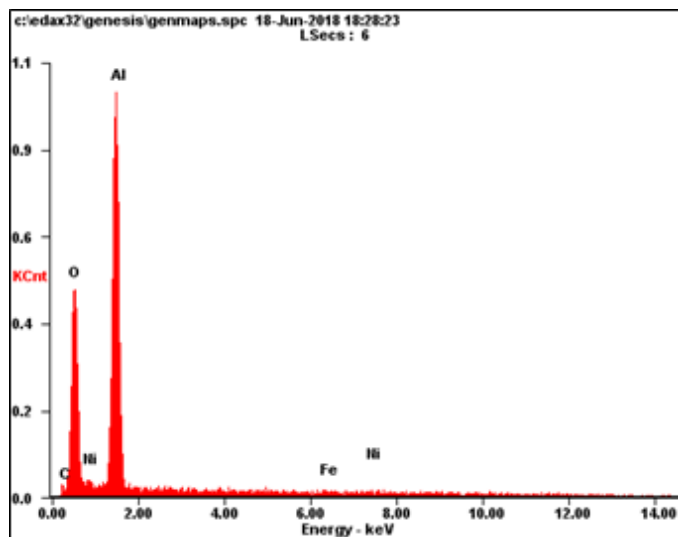


Figure 3-37: EDAX analysis of NiFe 1:1 nanofiber catalyst after 9 hours of reaction.

Shown in **Figure 3-36**, spherical nickel carbides have appeared on the surface of the pellet as shown by the red arrows. There are fibers connecting several spheres in the SEM image and increased carbon growth compared to the NiFe 2:1 nanofiber catalyst at the 9-hour mark as shown in the red circles in **Figure 3-36**. The EDAX in **Figure 3-37** shows a higher carbon level of 8.24 wt% and lower nickel and iron at 4.76 wt% and 3.61 wt% (1.7 at% and 1.36 at%). After 15 hours of reaction time, a NiFe 1:1 nanofiber pellet was prepared and studied under SEM and EDAX to determine surface morphology and elemental percentages. This is shown in **Figure 3-38** and **Figure 3-39** below.



Figure 3-38: SEM imaging of NiFe 1:1 nanofiber catalyst after 15 hours of reaction showing nickel carbides (arrows) and nanofiber clumps (circle).

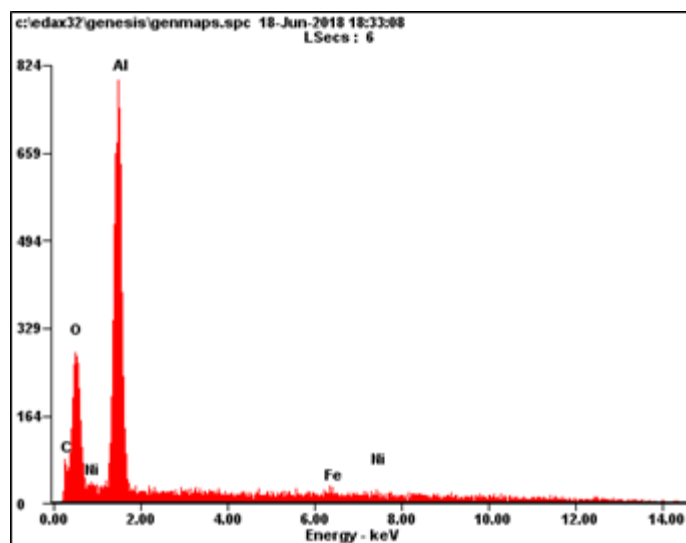


Figure 3-39: EDAX analysis of NiFe 1:1 nanofiber catalyst after 15 hours of reaction.

The 15-hour reaction sample shows an intense coking of the surface of the pellet. Carbide spheres are much larger now as shown by the red arrows in **Figure 3-38** and

smaller clusters of catalyst rest on a darker amorphous carbon surface which is circled in **Figure 3-38**. Carbon's elemental peak is at 24.16 wt%, which is 15.74 wt% higher than the 9-hour sample indicating significant carbon buildup. Nickel and iron peaks have stayed similar to the 9-hour run positions at 3.82 wt% and 3.01 wt% (1.19 at% and 0.98 at% respectively) which is an increase from nickel by 0.05 at% from the 9-hour run. This carbon buildup is also shown in the visual inspection of the catalyst shown in **Figure 3-40** below. The center of the 15-hour reaction sample is dark with coking while the initial samples look similar to the NiFe 2:1 nanofiber sample and the middle samples core has not completely coked up.

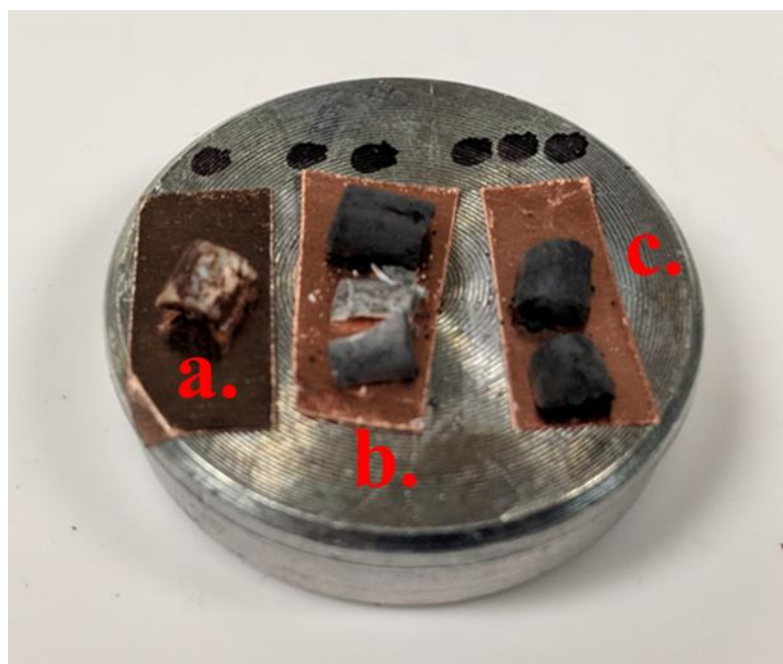


Figure 3-40: Visual inspection of NiFe 1:1 nanofiber catalyst showing samples a.) before reaction, b.) after 9 hours on stream and c.) after 15 hours on stream.

3.4.3 Magnesium Aluminate Spinel Nanofiber Support Tests

Finally, a spinel-type catalyst was fabricated. Magnesium aluminate was chosen as a spinel type support for the creation of spinel containing heterogeneous metal oxide nanofibers due to its high stability and recent adoption into industrial processes [85,86]. These nanofibers were made as supports to be seeded with a nickel catalyst through wetness impregnation to test the loading capability of nanofibers through traditional catalyst loading techniques. To create the magnesium aluminate supports, magnesium nitrate and aluminum nitrate were mixed together, and the pH of the aqueous solution was adjusted until it reached 9.5 using ammonium hydroxide. The solution was stirred for 1 hour and a white precipitate formed. The precipitate was allowed to settle and then the solution was decanted, and the precipitate was allowed to dry. The precipitate was then added to a solution of 10% wt PVA and electrospun at 20 kV and 12 cm between the syringe tip and the target. The resulting film was collected and calcinated at 500 °C in a burnout furnace. After this, 3 ml of a 20% wt nickel solution was added to the nanofiber dropwise until saturated, then dried under vacuum at 100 °C. After crystallization of the nickel, the catalyst was placed in the reactor without modification. The testing temperatures within the reactor were at 700 °C, 800 °C and 900 °C, similar to the previous studies. The first run was at 700 °C, **Figure 3-41** shows the evolution of gases during the runtime.

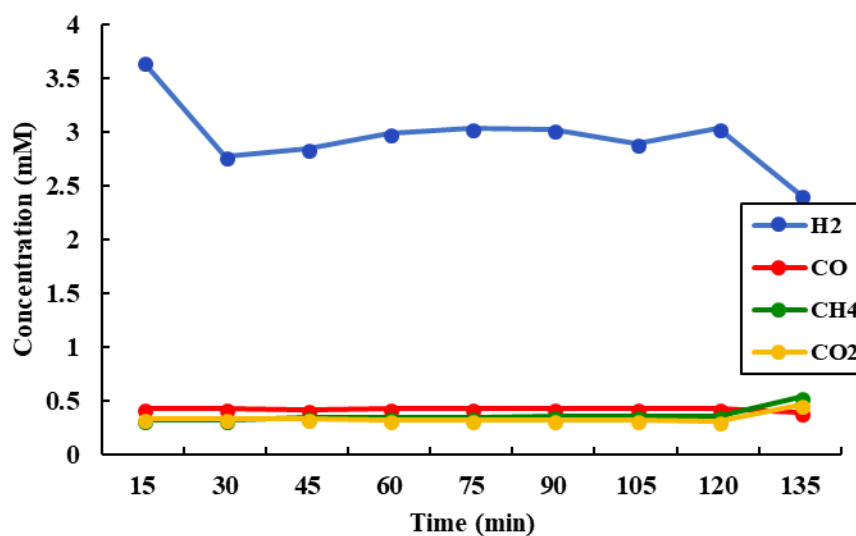


Figure 3-41: Gas evolution of MgAl₂O₄/Ni nanofiber catalyst at 700 °C.

As shown in **Figure 3-41**, the MgAl₂O₄/Ni catalyst shows a high conversion of the reactant gases at 81.84% for methane and 78.56% at the lower reaction temperature test. The hydrogen produced starts out high at 3.65 mM but reaches equilibrium at 2.87 mM as the reaction time progresses. The evolution of gases for the MgAl₂O₄/Ni catalyst at 800 °C is shown in **Figure 3-42**.

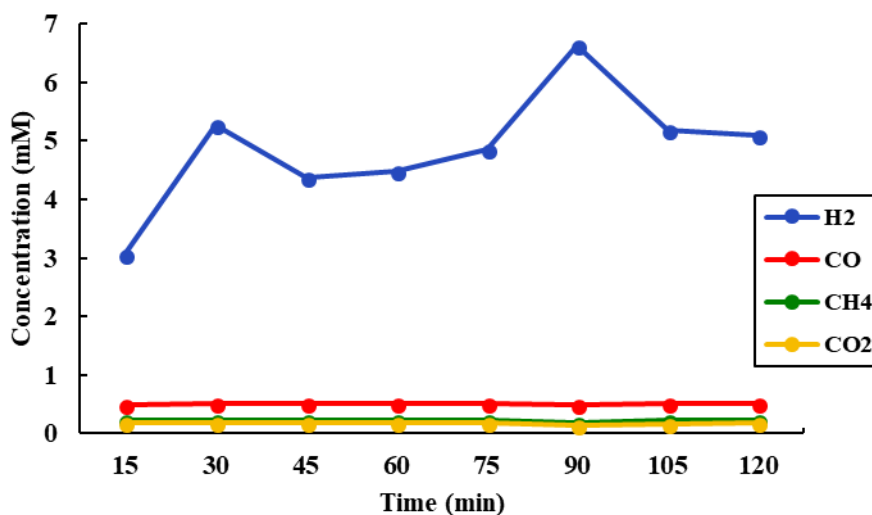


Figure 3-42: Gas evolution of MgAl₂O₄/Ni nanofiber catalyst at 800 °C.

At 800 °C, the conversion of the reactant gases very high, and the reactants are measured at only 0.22 mM on average for methane and 0.17 mM on average for carbon dioxide. The carbon monoxide has increased by 0.11 mM on average from its 700 °C run while the hydrogen gas has an average concentration of 3.65 mM. This is an increase of 63 % from the 700 °C test run and shows that there has been very little deactivation of the catalyst over the testing periods. **Figure 3-43** shows the gas evolution for the MgAl₂O₄/Ni catalyst at 900 °C.

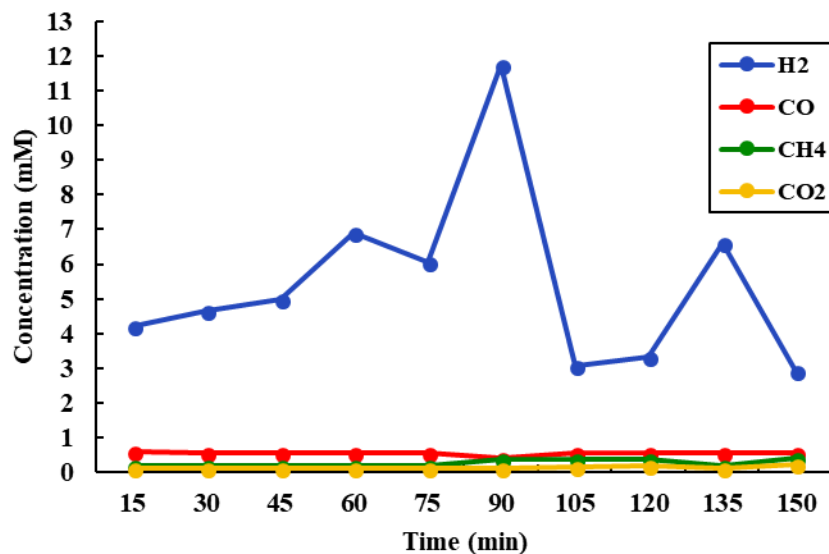


Figure 3-43: Gas evolution of MgAl₂O₄/Ni nanofiber catalyst at 900 °C.

Figure 3-43 shows the lowest concentration of the reactants for the 900 °C test run seen for any catalyst – both reactants are nearly completely consumed at 86.38% conversion for methane and 91.04 % conversion for carbon dioxide. After around 80 minutes the reactants start to increase in concentration indicating a drop in the reactivity, but the concentration gain stops at around 0.37 mM for methane and 0.12 mM for carbon dioxide. Hydrogen is extremely mobile with spikes as high as 10.45 mM indicating retention times within the mesopores of the catalyst are shifting due to carbon buildup. The difference in reaction rates from the 800 °C test run and the 900 °C test run seem similar in the first half, but carbon buildup influences the second half of the 900 °C test run. To observe the level of coking buildup on the surface of the catalyst, SEM and EDAX analysis was taken of the MgAl₂O₄/Ni before reaction, after 9 hours of reaction time and after 15 hours of reaction time. **Figure 3-44** and **Figure 3-45** show the MgAl₂O₄/Ni catalyst before reaction.

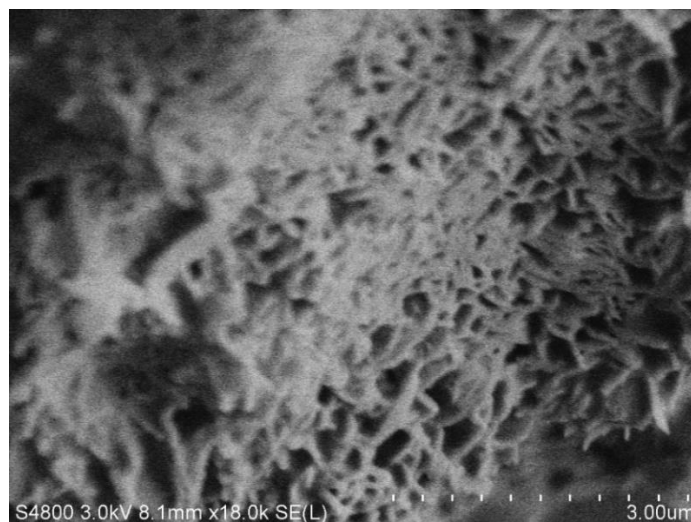


Figure 3-44: SEM imaging of $\text{MgAl}_2\text{O}_4/\text{Ni}$ nanofiber catalyst sample before reaction with nanofiber formation visible.

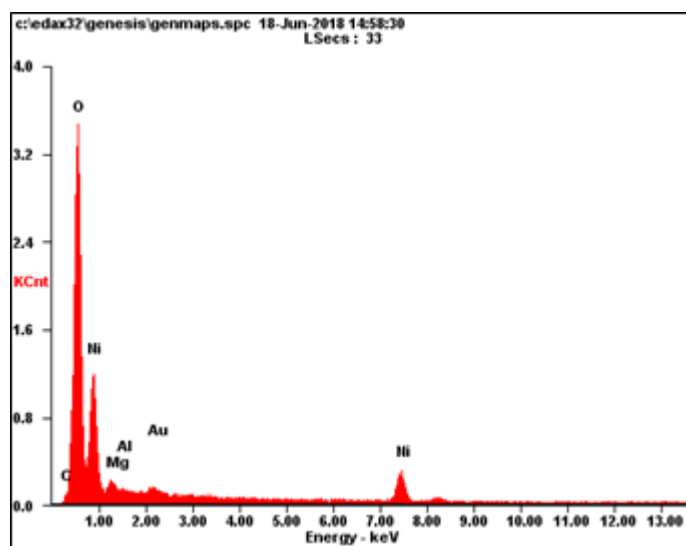


Figure 3-45: EDAX analysis of $\text{MgAl}_2\text{O}_4/\text{Ni}$ nanofiber catalyst sample before reaction.

As shown in **Figure 3-44**, the nanofibers have fused to create a spongy mesh during the calcination process. This contributes to the high retention of nickel in the membrane after wetness impregnation, which is a wt% of 35.34 or 13.12 at% as shown in

the EDAX analysis in **Figure 3-45** of the sample. Magnesium and Aluminum peaks were measured at 1.63 at% and 2.46 at%, while oxygen was measured at 53.43 wt% or 72.77 at% indicating nickel oxide had formed during the drying process. Gold was again used to assist in the imaging of the catalyst due to its inherent magnetism. After 9 hours, a sample of the catalyst was collected for study under SEM and EDAX techniques. **Figure 3-46** shows an SEM image of the surface of the catalyst and **Figure 3-47** shows the EDAX analysis of the catalyst.

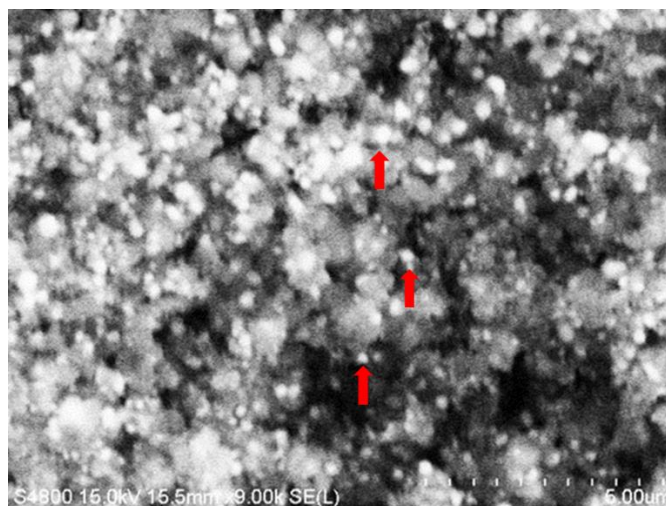


Figure 3-46: SEM imaging of $\text{MgAl}_2\text{O}_4/\text{Ni}$ nanofiber catalyst sample after 9 hours on stream, showing nickel nanoparticles (arrows).

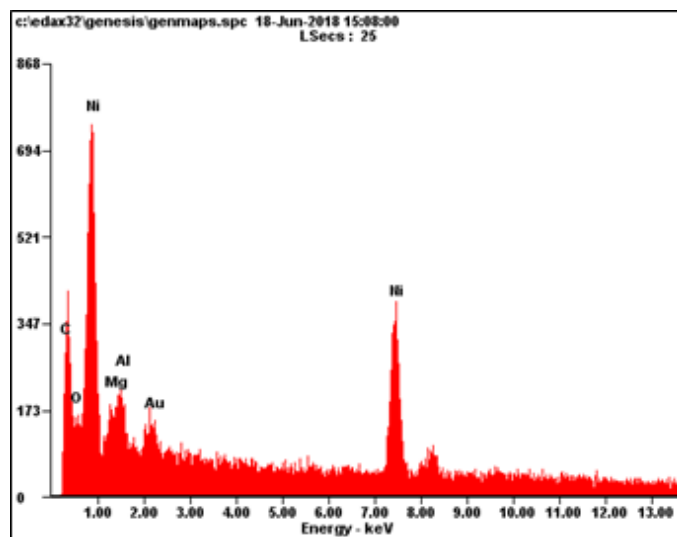


Figure 3-47: EDAX analysis of $\text{MgAl}_2\text{O}_4/\text{Ni}$ nanofiber catalyst sample after 9 hours on stream.

In **Figure 3-46**, the small bright dots are indicative of nickel nanoparticles on the surface of the catalytic support, with some highlighted by red arrows. The nanofiber supports have expanded and taken on a fluffy texture. This is due to carbon growth along the catalytic support structure with an increase in carbon by 21 wt% from the before reaction sample. The oxygen peak has significantly decreased from 72.77 at% to 7.96 at% while the aluminum and magnesium maintain similar at% at 1.65 and 2.53 at%, indicating the transformation of the nickel oxide into nickel metal, which is shown at 26.08 at% for this sample. Further carbon growth is shown after 15 hours of reaction in **Figure 3-48** and **Figure 3-49**.

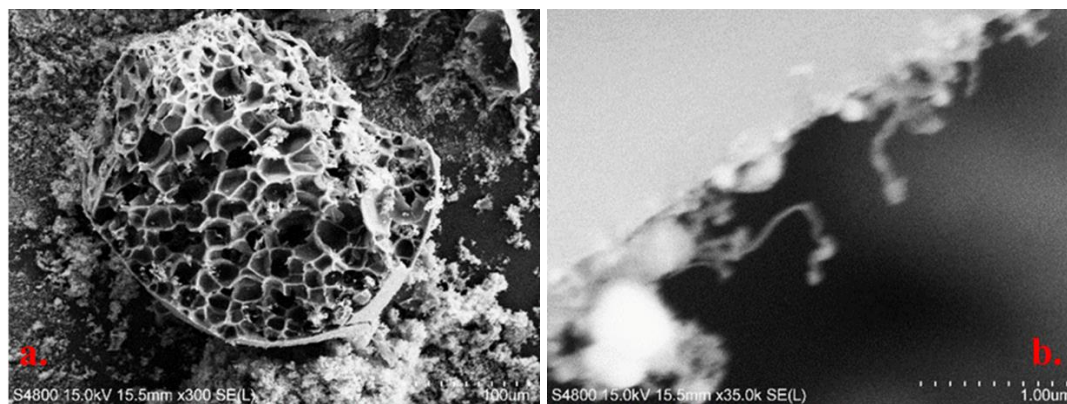


Figure 3-48: SEM imaging of $\text{MgAl}_2\text{O}_4/\text{Ni}$ nanofiber catalyst sample after 15 hours on stream, with a.) graphene bundles and b.) carbon whiskers

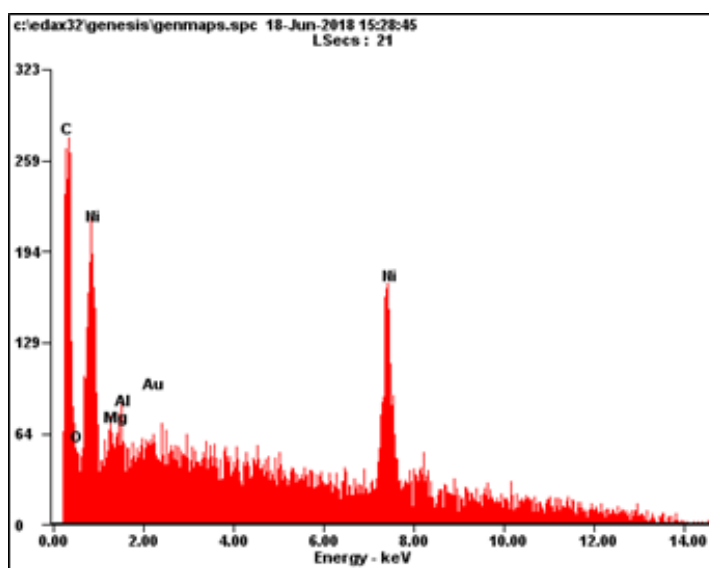


Figure 3-49: EDAX analysis of $\text{MgAl}_2\text{O}_4/\text{Ni}$ nanofiber catalyst sample after 15 Hours on stream.

After 15 hours of reaction time, very interesting nanostructures appeared on the surface of the catalyst. these nanostructures were made of carbon and seemed to be build-up from the initial mesh that made up the catalytic supports before reaction. The individual sheets that made up these structures were translucent and considered to be graphene sheets.

The features are very reminiscent of graphene nanowalls or graphene nanoflowers. These structures were only seen after 15 hours of reaction time with the spinel-type catalysts. While the carbon peak is much higher than the 9-hour EDAX analysis, but it's atomic percentage did not change much from the 9-hour run, gaining 13.34 at% over the 6-hour run time from the 9-hour sample. This can also be seen on the visible inspection shown in **Figure 3-50**, as the change to the powder is not visibly apparent.

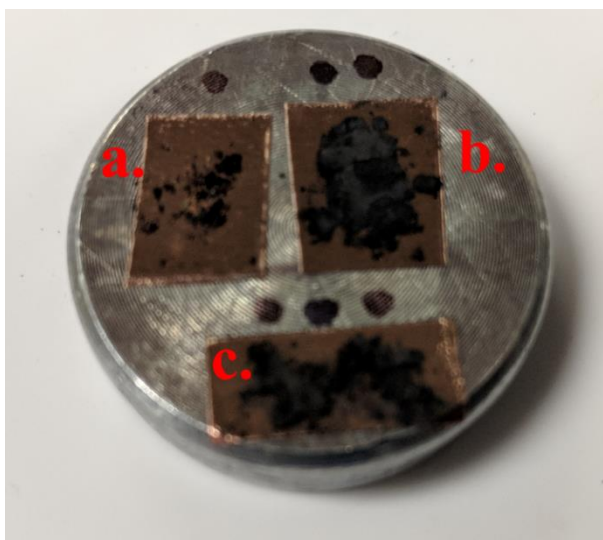


Figure 3-50: Visual inspection of MgAl₂O₄/Ni nanofiber catalyst at a.) before reaction, b.) after 9 hours of reaction and c.) after 15 hours of reaction.

3.5 Results and Discussion

After collecting all the EDAX elemental analysis of the nanofiber catalysts, the nickel content vs carbon content was compared over the test times as percentages of the weight and percentages of the atomic makeup of each catalyst. These were placed together as an easy reference to compare the effectiveness of each of the nanofiber catalysts alongside the original nickel catalyst for comparison in **Table 3-7**.

Table 3-5: EDAX elemental analysis for nanofiber catalysts with traditional nickel catalyst as a baseline.

Element	Initial wt%	Initial at%	9hr wt%	9hr at%	15hr wt%	15hr at%
Traditional Nickel Catalyst						
Nickel	5.28	1.85	5.52	1.92	5.91	1.89
Carbon	3.97	6.75	6.26	10.27	21.03	32.92
Nickel Ferrite 2:1 Nanofiber						
Nickel	22.76	11.77	36.25	25.26	33.19	21.42
Carbon	2.65	6.70	4.93	16.78	24.16	36.68
Nickel Ferrite 1:1 Nanofiber						
Nickel	21.63	1.73	3.33	1.14	3.82	1.19
Carbon	2.54	6.17	8.42	14.09	10.98	34.63
MgAl₂O₄/Ni Nanofiber						
Nickel	35.34	13.12	58.27	26.08	51.90	19.54
Carbon	6.81	12.36	27.99	61.22	50.52	74.56

Shown in **Table 3-7**, the content of the carbon for the nickel ferrite catalysts and the nickel catalysts increase in similar manners during all testing times. The carbon deposition increased drastically between the 6-hour and 9-hour marks, with the last run at 900 °C, the increased temperature means the Boudouard reaction is primarily responsible for the coke formation from carbon dioxide. Therefore, the nickel ferrite catalyst showed a less pronounced increase of coking compared to the pure nickel catalyst. The nickel ferrite at 1:1 ratio shows similar coking to its 2:1 counterpart (within 2 at% between either catalyst) indicating that increasing the iron content passed a certain point increases coke on the catalyst. The magnesium aluminate spinel supports showed a significant amount of

initial coking after only 6 hours but during the high-temperature phase remained very close to the same atomic percentage of carbon after 3 more hours at high temperatures. It is suspected that much of the carbon growth on this catalyst was predominately of a form of carbon that does not affect the reaction parameters of the catalyst, specifically the form of amorphous films (C_{β}) as shown in the SEM images after 15 hours. the spinel/nickel catalyst, which is why the catalyst itself had such excellent conversion rates.

Additionally, the average conversion rate for both methane and carbon dioxide were calculated based on the gas evolution of the reactants as described in equations 3.13-3.15. Using these equations, conversions were calculated from the reaction over the course of the testing periods were computed and averaged together to get an average conversion per catalyst per temperature, with the standard deviation of the measurements shown as error bars. These averages were obtained over the course of the 3-hour run times at 700 800 and 900 °C. The averages for the reactant gases are shown in **Figure 3-51** and **Figure 3-52** below.

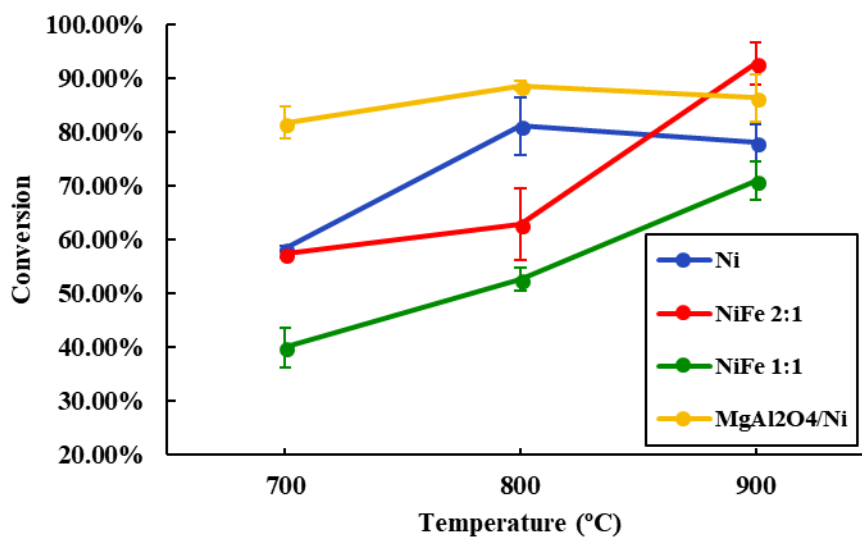


Figure 3-51: Average conversion percentages of methane of the nanofiber catalysts and the traditional nickel catalyst.

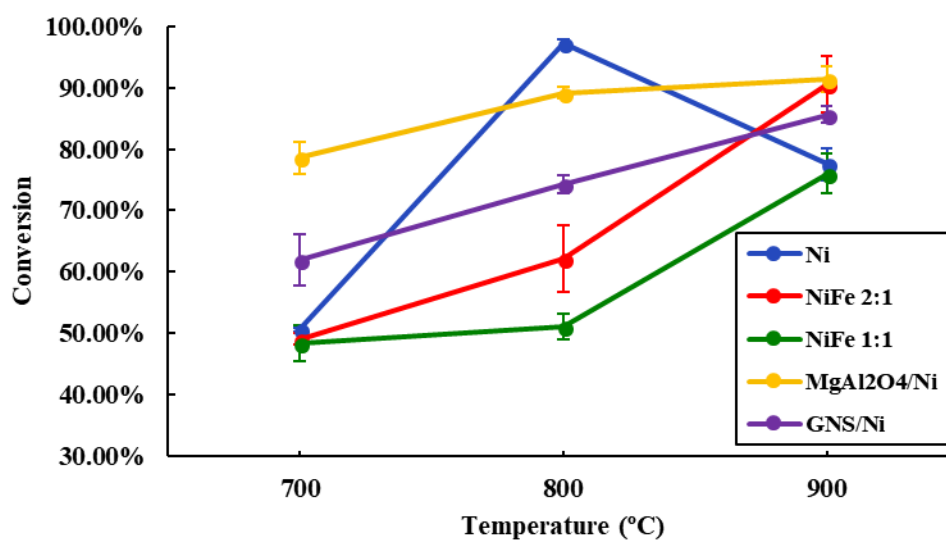


Figure 3-52: Average carbon dioxide conversion percentages of the nanofiber catalysts and the traditional nickel catalyst.

As shown in **Figure 3-51**, the rates of conversion for the MgAl₂O₄/Ni catalyst were much higher than the other catalysts at lower temperatures. Conversion rates at 800 °C were not as high as pure nickel for the nickel ferrites, but that changes for the nickel ferrite catalysts when the catalysts were tested at 900 °C, with higher concentrations of nickel increasing the conversion rates for both methane and carbon dioxide. The pure nickel catalyst had a spike in carbon dioxide conversion that drops after the first 30 minutes within the reaction period at 900 °C. This can be explained by the large buildup of carbon on the surface of the catalyst as seen in the surface inspection earlier.

Apparent activation energies for the nanofiber catalysts were then determined experimentally. Apparent activation energies are used to describe temperature dependent, non-stoichiometric reaction rates at which reactants and products are consumed. These are used due to the complex chemistry and multiple intermediate steps that are found in methane reforming and other industrial reactions. Apparent activation energies are used in these complex situations to offer a clear picture of the effect of the reaction conditions on the catalyst and differ from true activation energies due to their dependence on reaction conditions [24,27].

To determine apparent activation energy, natural logs of Arrhenius plots were made through experimentally determined reaction rates. Reaction rates were determined experimentally based on the rate of disappearance of reactant gases at different temperatures. Within a plug flow reactor, partial pressures are kept constant and the residency time defined by the space velocity is constant. With this in mind, the reaction rate can be defined as:

$$r = k_{app} P^{\alpha} P^{\beta} \quad Eq\ 3.16$$

where k_{app} is the apparent rate constant, and P^α and P^β are the partial pressures of the reactant gases. It is assumed the reaction is first order with respect to methane and carbon dioxide meaning that the α and β terms can both be set to 1. Under constant partial pressure and a steady flow rate, the reaction rate can be given by:

$$k_{app} \cong r \quad Eq\ 3.17$$

Which can then be put in terms of the Arrhenius equation:

$$k_{app} = A \exp\left(-E_{aa}/RT\right) \quad Eq\ 3.18$$

where A is the pre-exponential factor E_{aa} is the apparent activation energy and R is Boltzmann's constant and T is the temperature of the reaction. To determine apparent activation energy, the natural log is taken:

$$\ln k_{app} = \ln A - \left(E_{aa}/RT\right) \quad Eq\ 3.19$$

with the slope of the graph based on this equation being the $-\left(E_{aa}/R\right)$ term and its y intercept being $\ln(A)$. Multiplying the slope by the gas constant R gives the apparent activation energy of the catalyst for a reaction. The natural log of the reaction rates versus the inverse temperature are shown in **Figure 3-53** and **Figure 3-54**. To determine the slope, the points were first plotted and then a linear trendline was applied to the data. The slope was determined from the trendline to provide the apparent activation energies per catalyst.

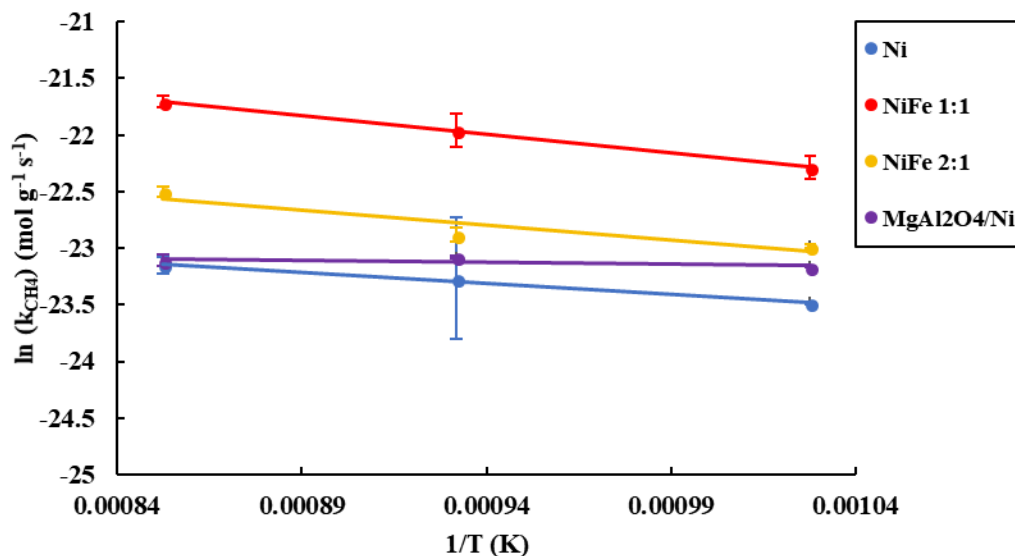


Figure 3-53: Natural log of rate vs 1/T for methane of the nanofibers catalysts and the traditional nickel catalyst.

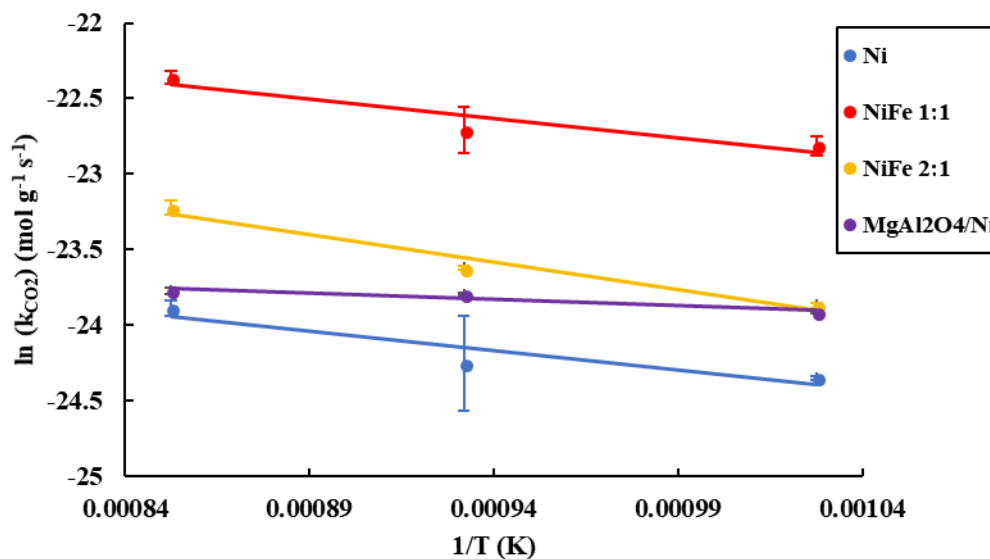


Figure 3-54: Natural log of rate vs 1/T for carbon dioxide of the nanofiber catalysts and the traditional nickel catalyst.

Here, the MgAl₂O₄/Ni showed excellent stability in the natural log of rate remaining nearly constant throughout the reaction periods, with very little error reported.

Pure nickel had the highest uncertainty across all temperatures, while nickel ferrite 2:1 shows a higher variation as shown by a high degree of error at lower temperatures. Using the **Figures 3-53** and **3-54**, apparent activation energies for the catalysts were obtained for both methane and carbon dioxide. These are displayed in **Table 3-8**.

Table 3-6: Calculated apparent activation energies for the nanofiber catalysts in kJ mol^{-1} with traditional nickel catalyst as a baseline for the conversion of methane and the conversion of carbon dioxide.

Catalyst	E_a of Methane Conversion	E_a of Carbon Dioxide Conversion
Ni	16.03	21.4
NiFe 2:1	22.35	30.34
NiFe 1:1	27.46	21.1
$\text{MgAl}_2\text{O}_4/\text{Ni}$	2.68	6.7

From literature, nickel ferrite catalysts made using wetness impregnation methods are reported between 30 to 58 kJ mol^{-1} for carbon dioxide, and between 91-36 kJ mol^{-1} for methane, showing that the 1:1 ratio of nickel and iron nanofibers have a 66% lower apparent activation energy than expected models, while the 2:1 ratio nanofibers behaved similarly to reported literature. Traditional nickel catalysts are reported between 30-104 kJ mol^{-1} for methane apparent activation energy, showing that the nickel catalyst falls within that regime. Nickel ferrite nanoparticle catalysts with a nickel to iron ratio of 3:1 were reported with apparent activation energies of 31 kJ/mol for carbon dioxide, and 91 kJ/mol for methane and traditional nickel catalysts are typically reported with apparent activation energies for methane between 33-104 kJ/mol [87]. This shows that while the traditionally made nickel catalyst falls slightly under the literature values, while the nickel ferrite nanofibers have a higher apparent activation energy for methane but higher apparent

activation energy for carbon dioxide due to the differences in the nickel amounts and the differences in the supports used. Magnesium aluminate/nickel catalysts have been reported with apparent activation energies of 26.39 kJ/mol for methane and 40.43 kJ/mol for carbon dioxide. The apparent activation energies of the magnesium aluminate nanofibers are much lower (over 80% for both apparent activation energies) than literature values due to the nanostructuring of the catalyst. The low apparent activation energies indicate that the magnesium aluminate nanofibers are very active, and the best catalyst/support combination for lower apparent activation energy [85]. Overall, the magnesium aluminate ceramic nanofibers were a highly stable support that displayed the highest levels of activity and the lowest apparent activation energy.

3.6 Summary

In this chapter, nanofibers were used as catalysts and catalyst supports for the dry reforming reaction. The nanofibers were made using an electrospinning process due to the flexibility in materials that could be incorporated into the metal/polymer sol-gel precursor for the nanofibers. After synthesis, the nanofibers were characterized to get diameters and determine porosity. After testing, they were calcinated at 500 °C to remove the polymer that formed the base of the sol-gel. This allowed the creation of metal and metal oxide-based nanofibers, which were then tested within the reactor at 700 800 and 900°C. While the temperature was varied the reactant flow rates were kept constant to measure the effect of temperature of the coke formation of the catalyst. Each temperature set point was tested for a 3-hour period, and then afterward the catalyst was allowed to run for 6 hours on stream at 800 °C to measure the extended effects of coking on the catalyst after 15 hours. Samples were taken of the catalyst after the initial 3 runs (9 hours total runtime) and after the final

6 hours of runtime (15 hours total runtime) and examined under the SEM. The tests found a buildup of different forms of carbon for each catalyst – polymeric and graphene films were prevalent on the magnesium aluminate spinels while carbides and were found on both nickel ferrite samples predominately. Due to the changes in surface morphology, the conversion of nickel ferrites on γ -alumina was found to be lower overall than the magnesium aluminate spinel support catalysts. Arrhenius rate equations were made for each of the equations and the natural log of the rate was plotted against the inverse of temperature to determine apparent activation energy of each of the catalysts. These show lower apparent activation energies and ability to operate at higher conversions overall for the nanofiber catalysts making these catalysts a viable alternative compared to traditional dry reforming catalysts.

CHAPTER 4

FABRICATION OF ELECTROCHEMICALLY EXFOLIATED GRAPHENE AND GRAPHENE NANOSCROLLS

4.1 Introduction

Graphene is a two-dimensional nanomaterial allotrope of carbon and the basic building block of most carbon-based nanomaterials. Due to its unique electronic properties, its immense material strength, and thermal and optical properties, graphene has a wide variety of research focused on its properties and applications [88-107]. While carbon-based supports seem counter-intuitive in preventing carbon growth on catalysts, both single wall and multiwall carbon nanotubes have been used as support materials for dry reforming and were shown to have a lower coking rate than traditional nickel catalysts. This was attributed to the electronic properties of the tube due to the stress placed on the scroll by the curvature of the tube [61,157].

Carbon nanotubes are expensive to synthesize, however, and so are difficult to use as an industrial scale solution to catalytic coking [144]. Graphene nanoscrolls (GNS) are produced by scrolling a graphene sheet and have been shown to have similar properties as carbon nanotubes but can be created using scalable, low-cost electrochemical methods [118,119]. This allows for the potential to utilize graphene nanoscrolls as a low-cost and scalable carbon nanotube replacement support for nickel nanoparticles without sacrificing the supports coke resistance.

This chapter discusses the properties of graphene and the formation of graphene platelets through an electrochemical exfoliation of bulk graphite process. In addition, graphene nanoscrolls were produced from the graphene platelets using an ultrasonication-induced scrolling process. These graphene platelets and graphene nanoscrolls were studied and characterized using a variety of techniques as shown in section 4.6 and 4.7. Then, nickel was loaded into graphene nanoscrolls through a vacuum loading technique and used as catalysts in the dry reforming reaction with data gathered from the GC, showing the evolution of gases at 3 different temperatures and fixed flow rates. This was used to show reactant conversion for the graphene nanoscroll catalyst at different temperatures and ultimately to determine apparent activation energies of the reactant intermediates. Additionally, coking on the surface of the graphene nanoscroll catalyst was investigated using scanning electron microscopy to observe surface morphology of different coking types and electron dispersive x-ray spectroscopy was used to observe the changes in carbon percentages on the surface of the graphene nanoscroll catalyst. This data was then compared to the nanofiber catalyst discussed in chapter 3 to determine the best catalyst for the dry reforming reaction.

4.2 Graphene Background

Graphene, since its discovery in 2004, has been at the forefront of nanomaterials research. Graphene is a 2- dimensional carbon allotrope and is the basic building block of graphite, which is made of millions of sheets of graphene stacked and compressed together, with each graphene sheet bonded on the (002) plane. Graphene itself has shown incredible elasticity, high electrical and thermal conductance, and optical transparency. These

qualities help explain why the discovery of graphene has started a rush of research into 2-dimensional nanomaterials [88-90].

Early research into graphene was focused primarily on two-dimensional phenomena in graphene such as half-integer quantum Hall effects and Dirac Fermion behaviors that are exhibited by the charge carriers in graphene. There has also been research into developing graphene-based micro/nano-devices that operate in the terahertz frequencies such as transistors and antennas and developing scalable production processes to make mass-produced graphene economically viable [91].

The potential impact graphene has on modern technology is vast. From more well-known devices such as field effect transistors to the use of graphene flakes in water filtration, from use as an additive to increase the strength of a material to next-generation nanoscale heat sinks, graphene has become a standard research material in almost every field. While there has been a large amount of research into the many applications of graphene, fabrication of graphene for use in these applications is a field of utmost importance. Due to graphene's simplicity as a chemical there are many fabrication methods that are used to derive the nanomaterial, each with a focus on specific properties of the material [92-95].

Currently, fabrication of pristine graphene easily ranks among the most expensive material processes in the world. Pristine graphene is single-layer graphene with no defects in its chemical structure that has had its free bonds at its edge bonded to hydrogen in a process known as passivation. While this synthesis process produces graphene that is very useful for studying the physical phenomena associated with graphene, but the cost of the production process makes it difficult to use for practical applications. With this in mind, it

is important to pursue graphene synthesis techniques that can be scaled to practical production amounts while still retaining as much of their useful properties as possible [96].

4.3 Physical Properties of Graphene

Graphene is the only two-dimensional material found to date that is naturally occurring. The crystal structure resembles a honeycomb, or repeating hexagons, with sp^2 hybridized bonds between carbon atoms. This bonding structure is also found in graphite, which allows for atomic shearing properties and is the same property that is exploited by graphite pencils. Graphite is composed of graphene sheets, which are A-B stacked (also known as Bernal stacking), allowing for flakes to simply shear off. Because of graphite's structure, single flakes of graphene can easily be removed from a graphite bulk using scotch tape in a process known as micromechanical cleavage. This method was first used in the discovery of graphene and won the researchers Novoselov and Geim the Nobel Prize in 2010 [97,98].

Studies have been done to characterize the bond structure in the graphene lattice. T. Nakajima and K. Shintani prepared graphene nano-disks that were used for studies that characterize the different edge types of graphene: armchair and zig-zag. This work focused on the edge configurations and shapes of graphene sheets to illustrate dependencies of stability and equilibrium energies on graphene sheet structure. To compare data with theoretical models, the authors use a molecular dynamics simulation on the equilibrium structures of graphene. The model, reproduced in **Figure 4-1**, revealed a typical relaxed configuration of a graphene sheet with sides: a, b, c, and d that have bond lengths of 1.45, 1.46, 1.47, and 1.48 Å respectively [99].

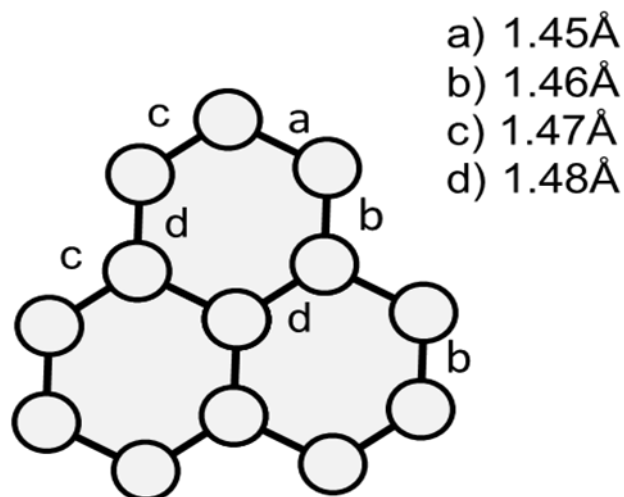


Figure 4-1: Graphene bond structure and lengths.

Synthesis methods have also been shown to have an impact on the physical properties of graphene, affecting bond structures within the atomically thin sheet. Using a chemical vapor deposition synthesis process, graphene was theoretically predicted to have a maximum surface area of $2600 \text{ m}^2 \text{ g}^{-1}$. Due to the alignment of carbon atoms within the honeycomb lattice, it was shown that graphene could be utilized as a hydrogen storage medium. Rao *et al.* predicted that single-layer graphene can accommodate up to 7.7 %wt of hydrogen [100].

Lui *et al.* reported on the ultra-flat properties of graphene sheets, by using a mica support as a substrate and micromechanical exfoliation of Kish graphite. It was reported that height variations of pristine graphene sheets could change up to 25 pm over micrometer lateral length scales. Their measurements were acquired by using an atomic force microscopy (AFM) in a non-contact mode to characterize the topography of the sheet. The lateral and height resolution of the AFM was 7 nm and 23 pm, respectively [101].

As memory applications in computers continue to demand faster digital signals in smaller form factors, graphene has been used in nano-magnetism applications. Nanographite particles were shown to exhibit unusual spin glass behaviors and magnetic switching phenomena. Yang *et al.* showed the existence of ferromagnetically ordered ground states in the zig-zag edge type of graphene, which is magnetic irrespective of whether the edges are regular or irregular. It was further shown that graphene possessed an up spin in a magnetic field and showed a down spin in a reversed field. This shows that graphene is a promising material for spintronic research [102].

Graphene's elastic properties have also been explored. C. Lee *et al.* probed monolayer graphene using non-contact mode AFM. Holes 1.5 μm in diameter were etched in silicon using a diamond AFM tip and graphene samples were placed over the holes and tested for elasticity, intrinsic strength, and ultimate strength. Testing was accomplished using a nanoindentation technique with the AFM tip. The testing showed that the second-order and third-order elastic stiffness for monolayer graphene corresponded to a Young's modulus of 1.0 TPa making it one of the strongest materials ever measured [103].

Graphene has also been used in the creation of higher capacity ultra-capacitors. Studies have shown reasons to believe that graphene may be able to store twice the charge as current commercially available materials. The ability of graphene to store charge can be attributed to massless charge carrier state within the nanomaterial that can be magnetically turned on and off, releasing power or storing it [104,105].

4.4 Electronic Properties of Graphene

Graphene has many properties that make it desirable for research and industrial applications. Perhaps the most interesting set of properties of the material are its electronic

properties. The use of graphene in electronic devices depends on the structure, construction methods and defects that might be in the graphene lattice due to the influence these have on the properties of the material. Additionally, multilayer graphene quickly loses its graphene-like properties as more graphene sheets are bonded together. It takes as little as three layers of graphene bonded together to start exhibiting graphite-like qualities [106].

In a typical crystalline structure, electron motion is described by the Schrödinger wave equation. In graphene, electrons move through the material as massless fermions guided by the Dirac equation. The Dirac equation is a relativistic version of the wave equation that was originally developed by Paul Dirac to explain fermions traveling at speeds where relativity would become a factor. Electrons interact with the graphene's lattice structure to create "Dirac fermions" that behave as electrons that have no mass and thus effectively travel at the speed of light. These Dirac fermions have been described as a liquid as well in some circumstances. While this property of a honeycomb lattices was shown to be theoretically possible, graphene is the first material to ever exhibit this property. This high mobility of electrons in graphene gives rise to many of its other properties and has become the basis of many studies into the quantum electrodynamics of nanomaterials. The Dirac Equation is described by the Hamiltonian:

$$\hat{H} = \hbar v_F \begin{pmatrix} 0 & k_x - ik_y \\ k_x + ik_y & 0 \end{pmatrix} = \hbar v_F \boldsymbol{\sigma} \cdot \mathbf{k} \quad \text{Eq 4.1}$$

where v_F is the Fermi velocity of the Fermions, \mathbf{k} is the Fermion momentum and $\boldsymbol{\sigma}$ is the 2D Pauli matrix [107].

The Dirac equation lends itself to some interesting physics in a graphene sheet. The Dirac cone is a phenomenon that is exhibited by single layer graphene sheets. This

phenomenon is exhibited in tight-bonding models of graphene between two carbon molecules that make up the basis-set of the hexagonal lattice with lattice points:

$$\mathbf{K} = \left(\frac{1}{3}, \frac{1}{\sqrt{3}} \right), \quad \mathbf{K}' = \left(-\frac{1}{3}, \frac{1}{\sqrt{3}} \right) \quad \text{Eq. 4.2}$$

Giving a linear E-k relation that results in a conical energy level diagram. The cone structure has a zero bandgap in normal graphene and requires doping the graphene to open a band gap in the material. Opening a bandgap can be accomplished with as little as 3% doping with nitrogen, and less with other atoms. **Figure 4-2** shows a Dirac Cone diagram of graphene [107].

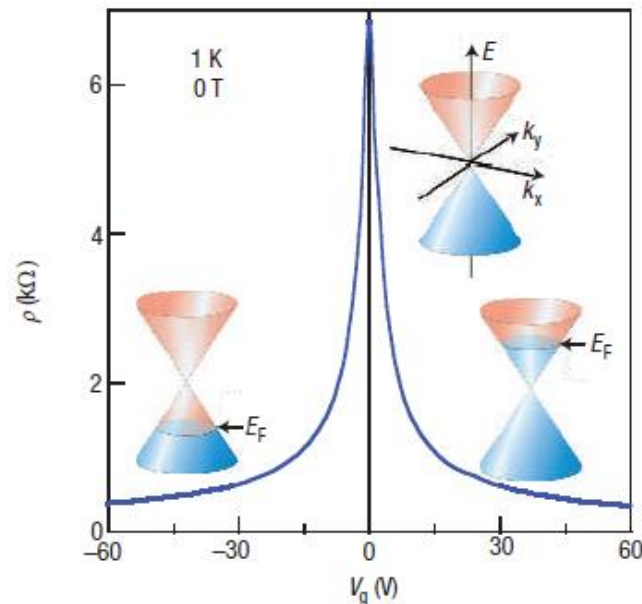


Figure 4-2: Energy spectrum of resistivity vs. gate voltage, with the Dirac Cone shown as an illustration of the energies as they pass through the structure.

Graphene also exhibits the quantum Hall effect at room temperature. This phenomenon is (as implied by its name) a quantum mechanical adaptation of the Hall effect found in classical physics. However, the quantum Hall effect is made up of half-integer

steps and thus is somewhat different from the classical Hall effect. This is due to the fact that the Dirac fermions are the charge carriers in graphene and not electrons. The quantum Hall effect has been shown to change back to an integer Hall effect when an electrical field is applied to bilayer graphene; the only known material to exhibit such phenomenon [107].

Additionally, the electronic properties of graphene have an influence on its optical properties as well. This is graphene's Dirac fermions coupling with the photons that hit graphene, and thus the optical transmission of graphene is due entirely to its fine structure constant:

$$\alpha = e^2/\hbar c \approx 1/137 \quad \text{Eq 4.3}$$

Without the addition of any material property for a single layer. The amount of light absorbed by graphene is large for its thickness, with 2.3% of white light being absorbed by a single layer of graphene which makes it visible to the naked eye. Each layer independently absorbs 2.3% and adding the layers together increases the absorption of light by another 2.3%. Graphene is unique in this property being one of the few nanostructures that are visible to the naked eye [108].

4.5 Edge Structures of Graphene

The electronic properties of graphene are also variable in nature depending on the graphene's edge structure. Graphene that does not bond its edges to a substrate is known as a graphene nanoribbon. Graphene nanoribbons, while possessing typical graphene properties, also exhibit different electronic properties based on the thickness of the nanoribbon and the edge structure of the nanoribbon.

Edge structure types are called zig-zag, and armchair based on the configuration of the hexagonal lattice in relation to the edge. The termination point of the graphene nanoribbon along the hexagonal structure is what determines how the lattice looks along the edge of the graphene nanoribbon. **Figure 4-3** shows the zig-zag graphene structure. Depending on the edge, the graphene may experience sp^3 hybridization, dangling bonds, or other edge defects. These π systems can both be present on a single nanoribbon, thus complicating matters further. The zig-zag edge type has a localized edge state at the Fermi level of graphene while the armchair type does not. Zig-zag graphene nanoribbons also have been shown to always be degenerate at wave number $k = \pi$ regardless of the nanoribbons width, meaning the wave functions are completely controlled by the edge type of the nanoribbon. These k values from zig-zag graphene trend away from π the further into the graphene nanoribbon, creating a band gap in zig-zag nanoribbons that is dependent on the width of the nanoribbon. Measuring the magnitude of the deviation in a zig-zag edge type nanoribbon gives a max at around 1.3 nm wide or about 7 atoms thick, meaning bulk graphite doesn't exhibit this band gap. It is also important to note that zig-zag graphene nanoribbons do not have to be 100% zig-zag edge type to show localized edge states and a band gap, though mixing the armchair edge type into the graphene nanoribbon decreases the overall band gap produced because they lack the edge state to contribute to it [109].

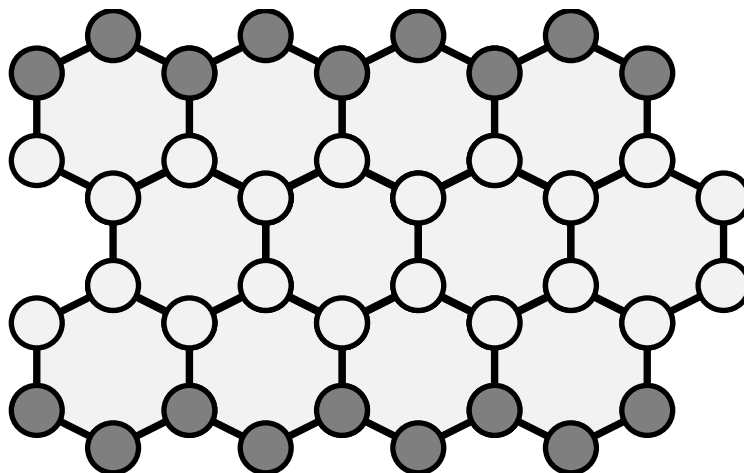


Figure 4-3: Example of zig-zag edge structure on graphene nanoribbon.

Armchair graphene nanoribbons (shown in **Figure 4-4**) also demonstrate several interesting properties. As stated previously, they do not possess edge states close to the Fermi level as zig-zag nanoribbons do. While most computational methods predict armchair edge nanoribbons as being capable of producing semiconducting to metallic properties, experiments have shown this edge type to always be semiconducting. A band gap can be created in armchair graphene as well, but the theory for this band gap is still developing with theories that it is due to electron-electron interaction, bond length differences between the hydrogen-carbon bonds at the edges and the carbon-carbon bonds in the bulk graphene, or that the current Hamiltonian for graphene needs a long-range “hopping term” to adequately explain the band gap. The band gap in armchair nanoribbons, regardless of which mechanism causes it, is proportional to $\frac{1}{W}$ where W is the width of the nanoribbon. Strangely, increasing the disorder at the edge via passivating the edge with radicals increases the conductivity of the nanoribbon, which is contrary to typical conductive materials. This disorder causes a deformation at the edge of the armchair which

is thought to be the reason for its odd electrical properties. At low disorder, the nanoribbon exhibits properties of an insulator, while at high disorder the nanoribbon becomes metallic. This allows control of electrical properties through introducing disorder into the edge type but requires some chemical changes beyond the simple structural effects of armchair graphene [110].

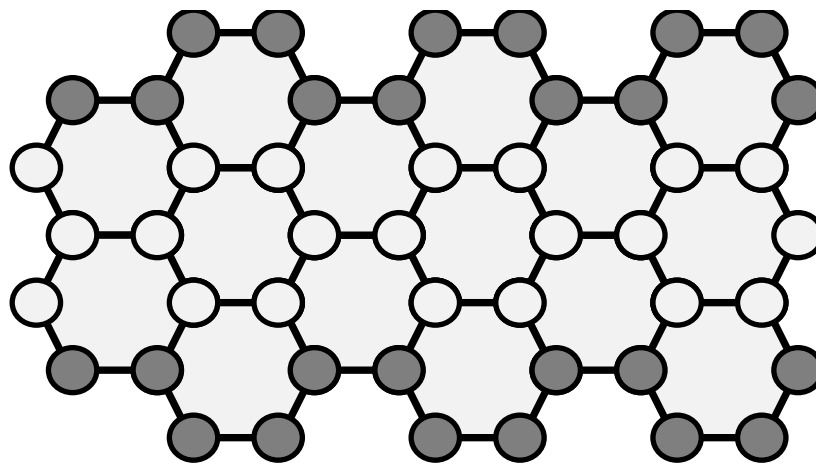


Figure 4-4: Example of armchair edge structure on graphene nanoribbon.

The changes to graphene nanoribbon's electrical properties by introducing disorder into the armchair edge type indicates that chemical changes to graphene can affect the electrical properties of the sheet. With the armchair nanoribbon, only the edges were altered to make these changes, however, several studies have attempted to chemically alter the interior lattice structure of graphene as well. This requires either growing the graphene sheet with different dopants or by adding certain extra particles to the graphene after synthesis. In the first case, graphene changes are due to defects in the structure itself, while in the second case the graphene changes its lattice structure to accommodate these particles.

Defects in graphene usually take the form of point or line defects or vacancies because other defect types are limited by graphene's two-dimensional nature. These defects are generally found in graphene that is grown via chemical vapor deposition (CVD) or similar methods due to the difficulty of guaranteeing the defect in graphene made from bulk exfoliation of graphitic oxide or other methods. Post CVD growth, graphene can be changed by irradiating the target carbon atom in the lattice with enough energy to knock the atom out of the lattice, allowing it to be sputtered away which leaves a vacancy. The use of charged ions fired at the honeycomb structure has also been shown to alter the structure of graphene. Introducing defects changes the Dirac equation for graphene, resulting in a different electrical response. This is due to the changes in the hybridization of the bonds in the area of the defect which effects electron trajectory. Point defects in the graphene structure scatter Dirac fermion waves, dropping the overall conductance of the graphene in general, but also possibility affecting it in different ways depending on the particle introduced, and if introduced on a graphene nanoribbon, wherein the nanoribbon it was introduced. While these changes are theoretically shown, they have yet to have an experimental result verifying them, due to the difficulty in introducing defects into the graphene structure [111].

Other work has been conducted on bilayer graphene by adding doping type defects, inducing a band gap between two attached layers. The graphene edges are then passivated with hydrogen. This construct of two graphene sheets with hydrogen bonds breaks many of the π bonds in the overall graphene structure which changes the graphene bilayer into a sort of quasi- sp^3 hybridization. These band gaps are tunable via the amount of hydrogen that has been attached to the surface of the graphene bilayer, which is known as

hydrogenated graphene. This hydrogenation is reversible and can be theoretically replaced by other atoms to further change the band gap opened in the graphene [112].

Graphene has been shown to be elastic, electrically conductive, transparent, and durable. Research into its physical and electrical properties have largely focused on two-dimensional phenomena such as half-integer quantum Hall effects and Dirac fermion behaviors that graphene charge carriers exhibit, while applications have focused on its use in micro/nano-devices in the terahertz range and synthesis methods have focused on economic viability at industrial scales. Synthesizing graphene sheets and then fabricating things from them is expensive outside of the lab scale. Progress in manufacturing and treating graphene in solution might make it usable at an industrial scale. Currently, there are many methods employed in the synthesis of graphene: chemical vapor deposition (CVD), epitaxial growth, micro-machining exfoliation, direct sonication, cutting carbon nanotubes and chemical reduction are just a few of the processes that have been studied [113,114].

4.6 Graphene Production

Current methods for production of graphene are wide-ranging. Initially, graphene was made by a mechanical exfoliation technique. This involved using an adhesive to mechanically separate graphene from bulk graphite by pulling the sheets apart and repeatedly contacting the adhesive surface to another adhesive surface [115,116]. Electrochemistry has also been studied and this method uses an electrical current to drive molecules in between the graphene sheets of a graphite crystal [117,118]. To create graphene in the lab, an electrochemical exfoliation process was developed that allows for

the creation of graphene nanoflakes in bulk quantities. This process was also used as the basis for the graphene nanoscrolls explored in section 4.8 [119]. **Figure 4-5** shows the graphene processing setup. This electrochemical exfoliation process works similarly to the electroplating of metals, which is as follows: a DC voltage is applied to the two graphite plates/rods (low voltage) while the plates are half to three quarters submerged in an electrolytic solution.

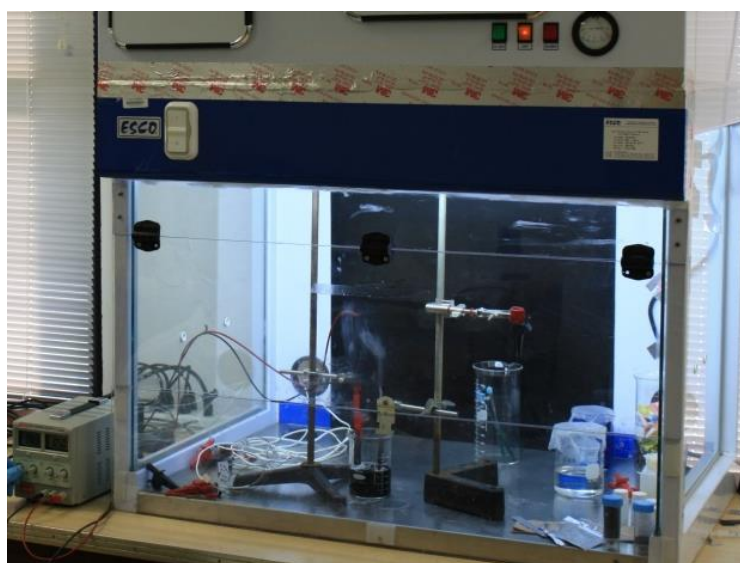


Figure 4-5: Graphene fabrication electrochemical setup.

Using a forward current, the electrolyte is pushed in between the weak bonds between graphene layers in the graphite rods in a process known as intercalation. The graphite electrodes are first intercalated with the electrolytic solution and upon reversing the electrical polarity graphene nanoflakes are stripped off the graphite. Using a dual graphite rod system, the process is able to simultaneously intercalate one graphite rod with electrolyte particles while stripping graphene from the other graphite rod. The low voltage

required for separating graphene from graphite crystals and the low cost of the electrolytic materials makes the electrochemical exfoliation method one of the safest and most cost-effective methods for bulk production of graphene. Similar to traditional metal electroplating setups, increasing the scale of production simply requires increasing the area of the graphite electrode, the amount of electrolyte and the amount of voltage being run through the graphite. As an added benefit, the electrolyte used in electrochemical exfoliation can be tailored to add specific enhancements to the graphene flakes. CVD produced graphene is expensive and takes a long time for processing, whereas our electrochemical exfoliation method is an inexpensive, scalable and faster processing [120].

To determine which chemicals were the most cost-effective electrolyte for scale-up, an analysis of the most common chemicals was done. **Table 4-1** lists the electrolytes and their associated costs, as well as the common post-processing chemicals. Prices were obtained using Dr. Wilson's VWR discount for a realistic look at lab scale-up procedures.

Table 4-1: Cost breakdown of electrolyte solutions.

Solvent	Molarity	Grams per liter	Cost per liter	Voltage used
KOH MW = 56.1 45% w/w is 11.677M sol	pH 13 (0.1 M)	5.61 g pure for 45% w/w): 8.564 mL	\$57.75/L, \$0.494/L plate sol	3V
SDS: MW= 288.3	0.1 M	28.83 g	\$67.45/100g, \$19.44/L plate sol	10V
PSS: MW = 70,000	0.001 M	70g	\$22.47	5V

As can be seen in the table, the PSS and SDS solutions, while usable for production of graphene at lower voltages, are a higher price per liter. PSS, in particular, was decided against due to the difficulty of separating the material from the graphene, which drastically lowered the yield. It was due to this that research was directed towards using SDS and KOH as the basis for the electrolytic solution. With a focus on the cost-effectiveness of the process, only a few materials were required for the creation of an electrochemical technique for the creation of graphene. The steps for production of the graphene were similar for each electrolyte with a small change in voltage (between 3-25 volts) however, allowing for interchangeability of the electrolyte.

The materials used to produce graphene flakes were sodium dodecyl sulfate (Alfa Aesar from VWR), potassium hydroxide, aqueous solution (45% w/w, Alfa Aesar from VWR), as for the electrolyte solution, dimethyl sulfoxide (Alfa Aesar, VWR) as storage solutions and polyvinyl alcohol, (MW: 10,000 VWR) were obtained and graphite sheets (from graphitestore.com) were used as electrodes for the electrochemical exfoliation. Additionally, a Keithley 2611A was used as a power source to provide voltage to the electrochemical process. The Keithley 2611A was hooked to a Dell computer and programmed using Test Script Builder to deliver its power in precise intervals to the system.

The process uses 2 graphite electrodes, thus eliminating the need for expensive and lab-restrictive metal counter-electrodes. The voltage was also set to change between positive and negative every 5 to 10 seconds to create a cycle of intercalation of the electrolyte in one electrode and then stripping the intercalated layers of graphene off of the electrode (while the same happens in reverse to the other electrode). Thus, automation of the process

was based upon a script that was written for this experiment in Keithley's Test Script Builder program for the Keithley 2611A power source.

Graphite electrodes were selected for their fines size (particle size). Isostatic pressing is a technique by which material like metal or graphite is placed in a pressurized oven with a chemically inert gas and while the oven is heated the gas expands pressing the material and increasing its density. Using isostatically pressed graphite allows interaction with a large number of graphite particles at once as the higher density and the lower particle size means more surface area overall. **Table 4-2** lists the pertinent material data for isostatically pressed graphite.

Table 4-2: GM-10 isostatically pressed very fine grain graphite.

Property	English		Metric	
Particle Size	.0004	in	0.00102	cm
Density	0.066	lb/in ³	1.82	gr/cm ³
Flexural Strength	8400	psi	57.9	MPa
Compressive Strength	18500	psi	127.6	MPa
Resistivity	5.5	Ohm x in x 10 ⁻⁴	---	
Hardness	65	psi	65	kg/mm ²
CTE	3.3	in/in °F x 10 ⁻⁶	5.9	Microns/m °C
Porosity	12	% VOL		% VOL
Thermal Conductivity	48	BTU/(h ft ² °F/ft)	83	W/(m ² . K/m)
Ash	0.05	%	---	
Temperature (Air)	750	°F	399	°C
Temperature (Inert)	5000	°F	2760	°C

The KOH electrolyte was created as a 500 mL 0.1 M KOH solution by adding 4.282 mL of KOH solution to 495.718 mL of purified deionized water. The other electrolytes were made similarly with deionized water. Once mixed, two graphite electrodes were fashioned from cutting a sheet of 4" x 4" graphite into 2 4" x 1" bars. These bars served as both anode and cathode and were placed approximately 3 inches into the KOH solution. After this, the automated program for the Keithley 2611A was activated, which shifted between +10V at 1 A max for 5 seconds, then -10 V at 1 A max for 5 seconds, then back. This continued for 6 hours, or roughly 2160 cycles. For the SDS solution, the electrodes

were set similarly to the KOH solution with the electrodes placed 3/4ths of the way into the solution, and the Keithley was set to the same voltage for the same amount of cycles. This process would cause a gradual darkening of the electrolytic solution, indicating the formation of graphene and nano-sized graphite particle formation. This process is illustrated in **Figure 4-6**.

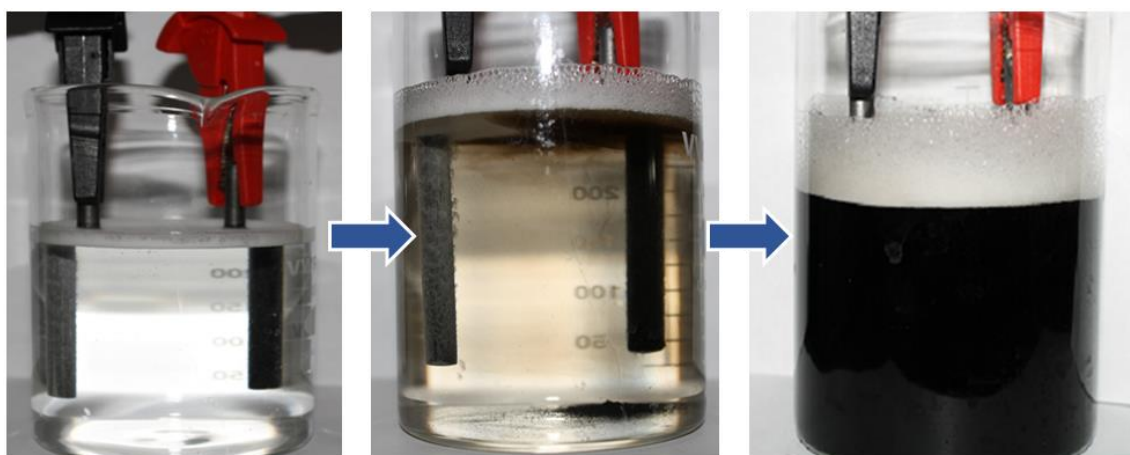


Figure 4-6: Graphene formation during the exfoliation process.

4.7 Graphene Characterization

Characterization of graphene flakes produced by electrochemical exfoliation has been carried out using a variety of methods. These samples were also tested against samples of graphene produced by third-party companies as a measurement basis for our own efforts. Characterization of the graphene obtained via the electrochemical process was carried out in the Institute for Micromanufacturing's metrology at the Louisiana Tech campus.

Scanning electron microscope images (SEM) was used to determine the physical properties of graphene produced in the lab. SEM images are created by using an electron

beam that is focused by magnetic fields to reflect off of the surface of a material. These electrons excite the atoms of the material they contact, causing the atoms to release secondary electrons, which are then detected and used to create an image of the material. SEM images provide detail of the physical dimensions of a graphene flake such as the diameter of the flake and some information on the thickness of the flake. It also is useful to look at multiple flakes and determine how the flakes interact.

In **Figure 4-7** we see a single flake of graphene under tunneling electron microscopy (TEM). These images were both obtained from graphene produced in the lab with the first being SDS electrolyte and the second from KOH, and both indicate a small thickness and large area of the flakes, of up to 1000 nm in diameter. Due to the electronic properties of graphene, there is some difficulty in imaging it with the SEM due to charging. To help with this, a conducting substrate (such as aluminum) should be used to collect the graphene. Lower acceleration and voltages also help with imaging of the graphene, as it can be very easily damaged by a high-powered electron beam and tends to deform. Lowering the detector closer to the sample also helps, as due to the low amount of scattered secondary electrons, the image may end up unclear. As a side note, this is also why transmission electron microscopy shows graphene to be transparent and difficult to image. Tunneling Electron Microscopy was carried out using the TEM at the metrology lab at UARK in Little Rock, Arkansas.

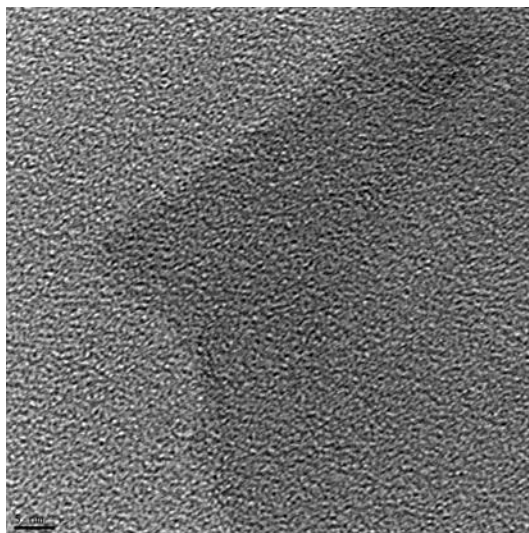


Figure 4-7: Single graphene flake imaged via TEM.

In **Figure 4-8** we see multiple flakes produced via the electrochemical exfoliation process. Once dry, these flakes tend to clump due to electrostatic forces, and some may even form weak bonds if not passivated thoroughly by hydrogen. This sample was collected after several purification steps.

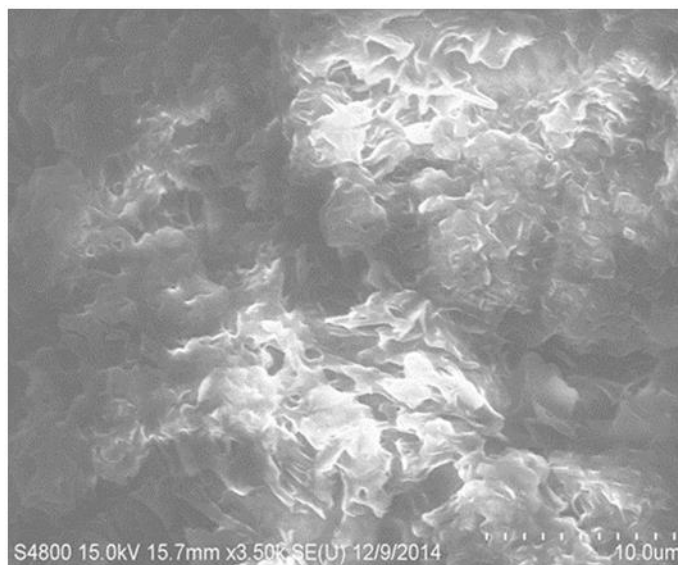


Figure 4-8: Graphene flakes produced by electrochemical exfoliation after drying.

4.7.1 Graphene NanoSheet XRD Analysis

Additional characterization was done on the graphene to determine its crystalline properties. First, x-ray diffraction was used to distinguish the crystal structure from that of graphene. X-ray Diffraction, or XRD, is a method that uses X-rays to identify structural properties of materials. Repeating patterns in materials are known as its crystal structure, and in order to identify crystalline patterns in materials, an X-ray emitter will rotate over a set number of radians (listed in degrees) while a detector measures the scattering of the X-rays as they collide and then rebound from the atoms in a crystal. This phenomenon is known as Bragg diffraction and can be described with the following equation, known as Bragg's Law:

$$2d \sin \theta = n\lambda \quad \text{Eq 4.3}$$

where d is the spacing between planes of the crystal and n is some integer that is a multiple of the wavelength λ . Using a visual aid, an example of Bragg's law can be seen in **Figure 4-9**.

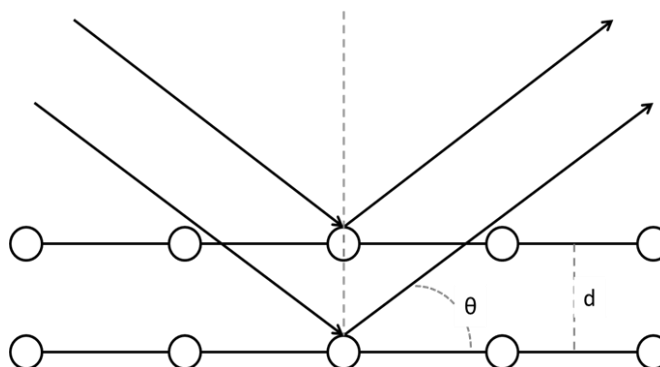


Figure 4-9: Bragg diffraction model.

During processing in the SDS solution, we produce graphene that is suspended in solution and graphitic particles (more than 10 atomic layers) that sink to the bottom. To remove the graphite residue, it is centrifuged out during processing and is measured with XRD for comparison. Graphite has a distinctive peak at 26° which graphene does not have, due to its two-dimensional nature. This peak corresponds to the [002] plane of the graphite, clearly indicating its layered nature. Identifying this peak or lack thereof is thus a quick way of determining if our sample is graphene or not, without having to wait on the use of the Raman spectrometer. Using the data gathered from the graphene powder and particulate, it is clear that the lab made graphene sample is missing the graphite peak. Additionally, the A0-3 measured graphene obtained from Graphenesupermarket.com shows this peak, indicating the presence of multiple layers stacked on one another. A0-3 is described on the site as 12 nm graphene that has 30-50 monolayers and this data lines up

with this description. **Figure 4-10** shows the XRD of lab-produced graphene compared to graphite and store-bought A0-3 graphene.

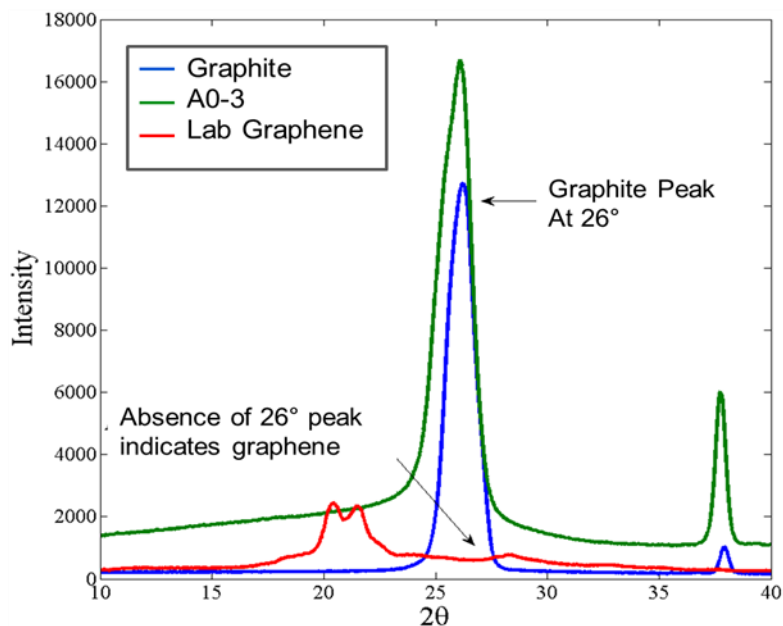


Figure 4-10: XRD data collected from lab produced graphene, A0-3 graphene from a third party, and graphite.

As shown in **Figure 4-10**, the XRD shows the lack of the peak at 26° for the graphene made via electrochemical processing. The inclusion of the smaller peaks around $20-23^\circ$ is typical of graphene but also may indicate defects in the crystallinity of the graphene sheet. These defects are possible indications of oxide formation on the graphene crystal, defined by the graphene oxide peak at 23° .

The graphene was then tested using Raman Spectroscopy. Raman Spectroscopy was discovered by C. V. Raman in 1928. This spectroscopy technique utilizes inelastic scattering of monochromatic light, typically from a laser, known as Raman scattering. This type of spectroscopy typically reads from 500-1500 nm wavelengths and is useful over

infrared (IR) spectroscopy for several applications, such as aqueous solutions or mixtures that give off gases, as these do not scatter. Raman spectroscopy gives information on fundamental modes, allowing chemical structures to be explored. It also offers a narrower band with fewer overtones than IR spectroscopy, with requirements below 400 cm^{-1} which many organics and inorganics require to be seen clearly. It takes little to no sample preparation for Raman spectra of a sample and can measure vibrational modes associated with symmetrical linking such as C-C or C=C bonding.

Raman is specifically useful for graphene due to its ability for accurately measuring the symmetric linking between carbon atoms within graphene. Raman microscopes work by exciting the sample using a laser of varying wavelengths. Raman spectra were obtained on UARK's Horiba HR 800 LabRam system. This Raman spectrometer has 3 laser excitations, 514 nm, 633 nm and 784 nm, though only 514 nm and 784 nm were used for measurement and each has about a $1\text{ }\mu\text{m}$ diameter spot size. A confocal microscope is used to collect the spectra (100x objective was used). The spectral data is passed between 1800 and 600 groove/mm holographic gratings and captured using a Peltier-cooled CCD camera.

4.8 Graphene Nanoscrolls

Graphene nanoscrolls, graphene wrapped in a roll, receive less attention than other allotropes despite their many unique characteristics [121-123]. These graphene nanoscrolls, like other carbon allotropes, have excellent electrical properties; it can withstand current densities on the order of $5\text{e}7\text{ A/cm}^2$ this is possible due to it being a single graphene sheet scrolled up [124,125]. Another compelling potential application of graphene nanoscrolls is as a medium for hydrogen storage [126,127]. Graphene nanoscrolls can hold two to four times more hydrogen than carbon nanotubes with the storage amount

adjustable via the variation of interlayer spacing [128]. The most important parameter of graphene nanoscrolls compared to nanotubes is its open-ended morphology. The theoretical maximum of the specific surface area of a graphene sheet is 1315 m²/g, and due to graphene nanoscrolls open-ended morphology, they are able to achieve a theoretical maximum specific surface area of 2630 m²/g [129]. With this increase of specific surface area, graphene nanoscrolls allow for a higher density of sites compared to carbon nanotubes. Other applications graphene nanoscrolls could be used for including; layered transistors, chemical/biological storage vehicles, with coil spring and rigid piston nano-actuator functionality [130-131].

Graphene-based nanoscrolls have been developed through a variety of fabrication processes from chemical synthesis to mechanical [132-133]. Mechanical methods for converting graphene into graphene nanoscrolls can involve mechanical exfoliation to create monolayer graphene sheets that are then deposited onto the SiO₂/Si wafer, which is then followed by intercalation of isopropyl alcohol (IPA) to produce graphene nanoscrolls [134]. Other mechanical methods involve ball milling graphite nanoplatelets creating graphene nanoscrolls with various morphologies including cylindrical and fusiform scrolls [135]. Additional novel methods for creating graphene nanoscrolls involve microwave sparks in conjunction with liquid nitrogen, hydrogenation enables scrolling, nitrogen-doped graphene nanoscrolls through the adsorption of Fe₂O₃ [136-140]. Chemical synthesis methods for producing graphene nanoscrolls have involved chemical vapor deposition (CVD) or the intercalation of graphite [141-144]. CVD allows for precise control of the crystallinity of graphene but can be expensive and difficult to scale for bulk production of graphene nanoscrolls. Acceptor and donor-type intercalation are other

methods of chemical synthesis for developing graphene nanoscrolls [145]. For acceptor-type intercalation, graphite is mixed with red fuming nitric acid (98% wt) while ozone is bubbled inside the reactor. Afterward, both processes utilize ultrasonication for the conversion of graphene into nanoscrolls [146]. Intercalation of graphite requires the use of a pressurized vessel and concentrated nitric acid (98% wt) or potassium metal. The first report of chemical synthesis of nanoscrolls involved donor-type intercalation, where potassium metal mixed with graphite is heated to 200°C overnight in an autoclave filled with helium [147]. Our process utilizes an electrochemical method for the fabrication of graphene and then an ultrasonication method to convert the graphene sheets into nanoscrolls.

Electrochemical exfoliation of graphite was investigated to adequately manufacture graphene nanoscrolls in bulk driving the implementation of these materials into consumer products. Electrochemical exfoliation does not require the use of pressurized vessels, it eliminates the need for external heating sources, and due to its great adaptability, various electrolytic solutions can be implemented to alter surface effects of graphene produced. Electrochemical exfoliation requires bulk graphite as the electrode material. Various electrolytic solutions can be employed ranging from acids to bases, for this work sodium dodecyl sulfate (SDS) was chosen as it is widely used in consumer products such as shampoo and toothpaste [148]. SDS used in electrochemical exfoliation has been reported to produce low defect monolayer graphene with a 3V bias voltage applied [149].

The voltage applied to the system was varied from 10V to 25V, with the polarity reversed every 10 to 20 minutes. Graphene nanosheets ranging from monolayers to graphite were produced with our method. To ensure proper removal of graphitic particles

the solution was centrifuged at 10,000 rpm for one hour and then the solution was decanted. Ethanol is then mixed in with the graphene-containing solution followed by ultrasonication for 3 hours. For the ultrasonication procedure, the frequency applied was 42kHz \pm 6% with a 100W power. Ultrasonication provides the required energy for the scrolling process to occur for graphene into nanoscrolls. During ultrasonication compression and rarefaction waves are created inside the liquid, with the rarefaction wave cycle producing a cavitation (vacuum cavity inside the liquid). The main stages of ultrasonic cavitation are nucleation, bubble growth and the implosion of the bubble, with these stages varied depending on the frequency, solvent, surface tension, and vapor pressure. These bubbles then implode creating temperatures ranging from 4000K to 25,000K, with pressures from 1000 to 10,000 atm and have cooling rates greater than 10¹¹ K/s [150,151]. These conditions are very localized but will affect nanoscale materials greatly. The final product is a uniformly formed GNS that can be easily distinguished from graphene nanosheets during characterization. This process is shown in **Figure 4-11**. The process described in the image, is a.) process starts with bulk graphite, b.) intercalation of graphite occurs via electrochemical exfoliation, c.) graphene nanosheets are produced, d.) nanosheets are ultrasonicated for 2 hours, e.) during the ultrasonicated process the graphene nanosheets are rolled into nanoscrolls. This allows for the production of bulk graphene-based nanoscrolls from solution-based graphene platelets.

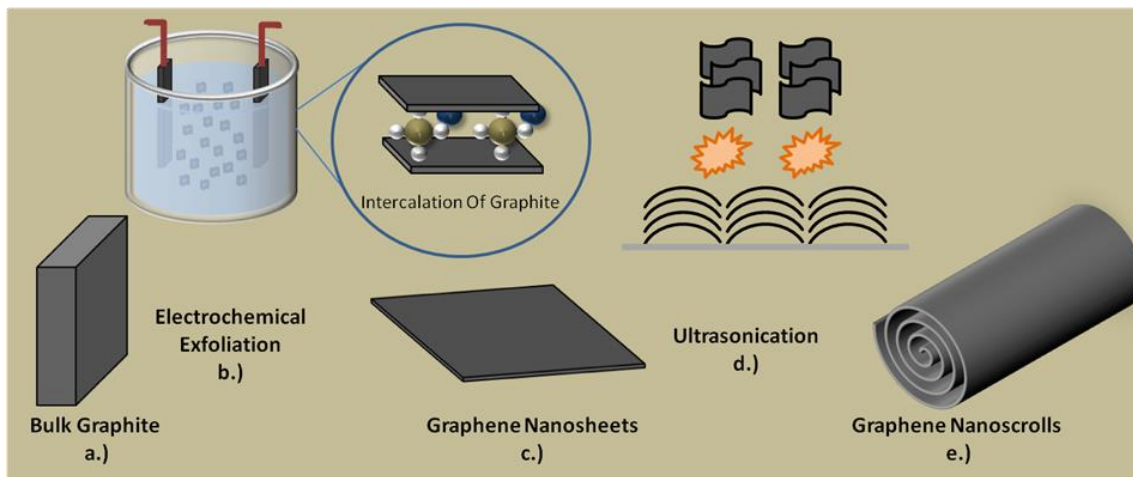


Figure 4-11: Dual carbon nanoscroll feedstock production.

Morphological studies were carried out with tunneling electron microscopy (TEM) and XRD. Electron spectroscopy was utilized to characterize the transformation of graphene nanosheets into graphene nanoscrolls. TEM imaging of the solution after electrochemical exfoliation shows the formation of graphene nanosheets as seen in **Figure 4-12a**. Even with potentials up to 25V monolayer graphene nanosheets can be produced as shown in **Figure 4-12b**. After ultrasonication, the GNS formed with the majority clustering together, seen in **Figure 4-12c**. This clustering is similar to carbon nanotubes and is due to π to π interactions [152]. Additionally, some graphene nanoscrolls were observed to have a cell within them separated by sheets of graphene, as seen in **Figure 4-12e** and possible fullerene formation in **Figure 4-12f**.

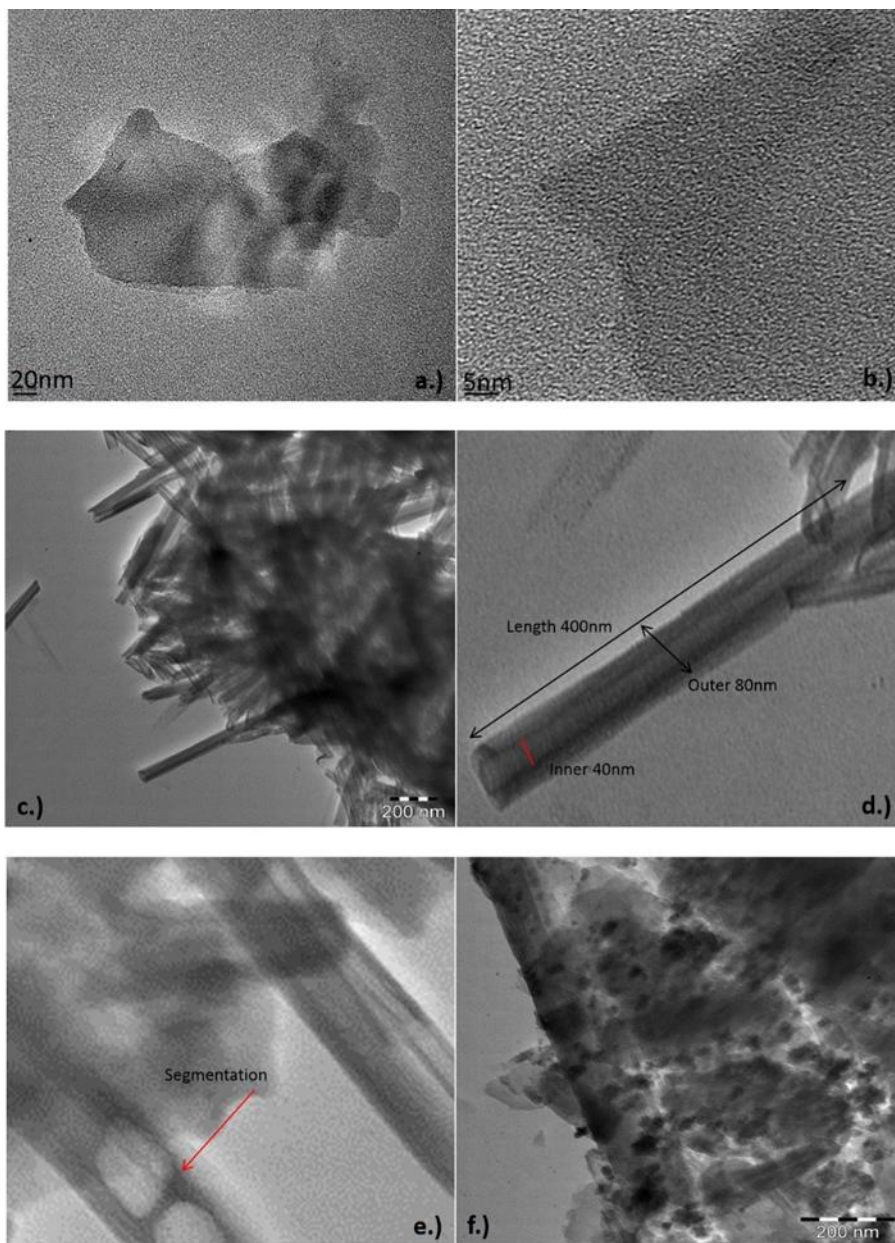


Figure 4-12: Morphological analysis with electron spectroscopy.

Typical graphene nanoscrolls have a cylindrical form that can be evaluated as an Archimedean spiral given by the expression:

$$r = a + b\theta$$

Eq 4.4

Shown in polar coordinates (r,θ) , where r is the distance from the origin, a is inner radius starting point, b is the interlayer distance and θ is the polar angle. This equation allows for finding the length of each spiral via:

$$l = \int_a^b \sqrt{r^2 + \left(\frac{dr}{d\theta}\right)^2} d\theta \quad \text{Eq 4.5}$$

The number of layers of the graphene nanoscrolls can be calculated from the general expression:

$$N = L/\pi D \quad \text{Eq 4.6}$$

where L is the length and D is the diameter of the scrolls. Variations of graphene sheets allow for graphene nanoscrolls with lengths ranging from 50 nm to microns. Using a graphene nanoscroll shown in **Figure 4-12d** as an example, a GNS having one micron in length with a diameter of 80 nm would have close to four layers with monolayer graphene having a thickness 0.34 nm. The number of layers in the example scroll was determined through equation 3 having 3.9789 turns, which gives a graphene sheet length of 1.497 microns.

4.8.1 Graphene Nanoscroll XRD Analysis

XRD analysis techniques give a more complete picture of the crystalline structure and help determine the quality of the graphene nanoscrolls. Again, graphene was centrifuged and washed from the SDS and then ultrasonicated. The graphite particles collected after the centrifuging step shows an intense response peak at 26.4° , this corresponds to the [002] plane of graphite. The graphene-containing solution after being decanted and dried shows the absence of the 26.4° as well as other peaks associated with graphite (**Figure 4-13**).

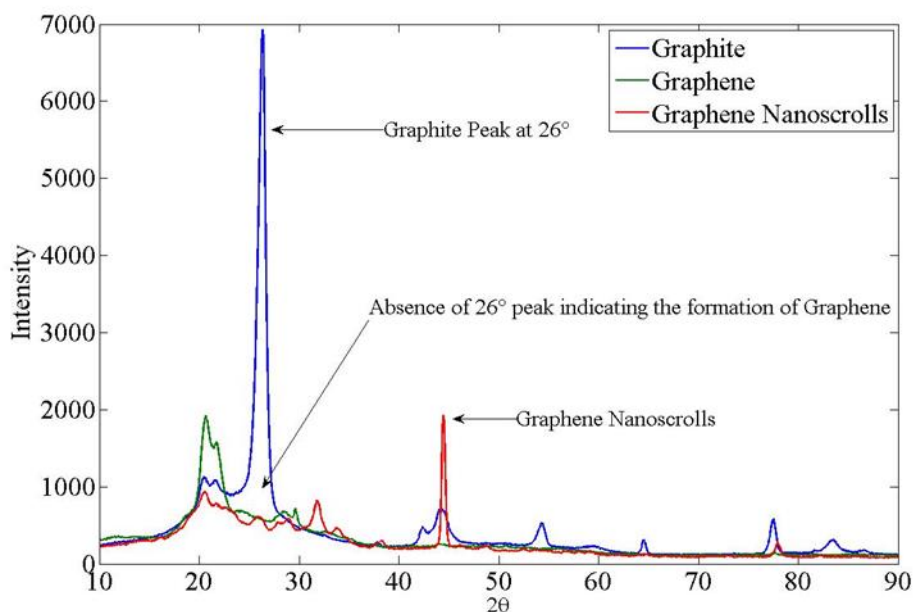


Figure 4-13: XRD analysis showing the crystallinity of the carbon nanostructures from the conversion of graphite to graphene nanosheets to graphene nanoscrolls.

The graphene nanoscrolls show during XRD analysis the absence of the 26° graphite peak. At 44.5° the nanoscrolls have a peak with a significant intensity. For further analysis of the graphene nanoscrolls, we compared single wall, (obtained from Carbon Solutions) and multiwall nanotubes (obtained from MicroTechNano, USA). Both our nanoscrolls and SWCNTs have a peak around 44.5°, the peak intensities illustrate the crystallinity differences (**Figure 4-14**). Graphene nanoscrolls are not pure single-walled structures as is evident by the difference in peak intensities. When comparing our graphene nanoscrolls with MWCNT at the 44.5° shows that they have close to identical intensities, however, our nanoscrolls do not have the large graphite peak at 26.4° as the MWCNT. The

right shift of peak at 44.5° for the graphene nanoscrolls can be attributed to the stress of the spiral structures [153].

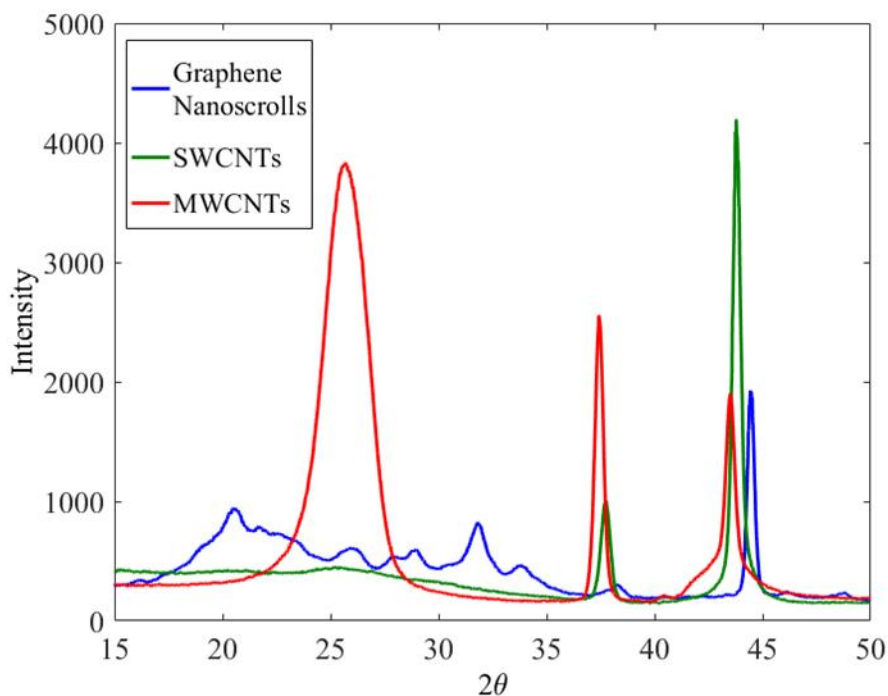


Figure 4-14: XRD comparison of the graphene nanoscrolls with as bought single wall and multi-wall carbon nanotubes.

Another area of interest is the peak at 32° for the graphene nanoscrolls. This peak is only present in the graphene nanoscroll sample. One theory is the peak represents the bonding of the graphene nanoscrolls with sodium from the SDS solution during ultrasonication. Computational work on carbon allotropes that are produced at pressures in the GPa range shows some structure at the 32° , such as M and X carbon allotropes [154]. Ultrasonication can possibly create localized temperatures and pressures to produce such structural changes to the carbon structure.

4.8.2 Raman Spectroscopy

In addition, the graphene nanoscrolls were studied under Raman Spectroscopy. These tests were again carried out at the University of Arkansas at Little Rock. Raman spectroscopy is an ideal tool for graphene and carbon nanotube study because it is a simple, non-invasive technique that can be used to study the excitation wavelengths of the sp² hybridized bonds [155-157]. Raman spectroscopy was carried out by floating the graphene nanoscrolls in a solution of ethanol and water. The solution containing the nanoscrolls was then added drop-wise to a silicon wafer and allowed to dry in the air before measurement. The Raman microscope utilized a laser with a wavelength of 514 nm for visible light and 784 for the near infrared and a magnification of 100x. Raman spectroscopy for the electrochemically fabricated graphene nanosheets is presented in **Figure 4-15**.

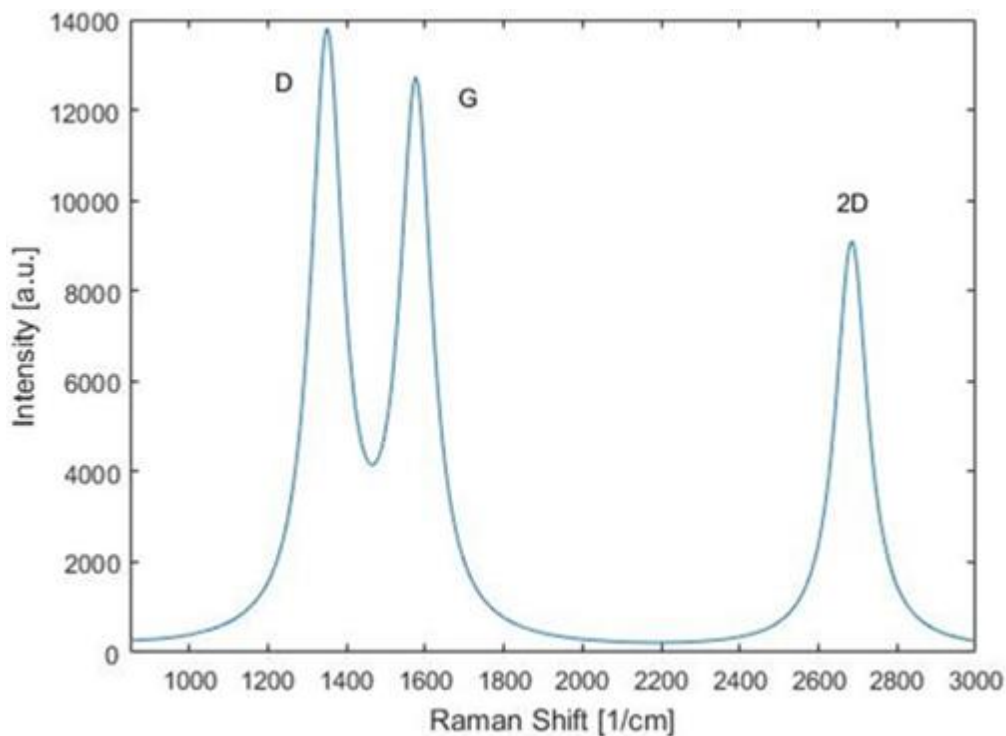


Figure 4-15: Raman spectroscopy of graphene nanosheets

Shown in **Figure 4-15**, the D-mode peak, or first order overtone, shows up at 1300 cm^{-1} , indicating disorder within the sp^2 bonds. This is due to distortion within the graphene structure of the nanoscrolls. At around 1580-1590 cm^{-1} , the G-mode, or second order overtone, of graphene represents the stretching or flexing of the graphene C-C bonds. The fact that these are split may represent impurities within the graphene. The D/G ratio for **Figure 4-15** sample (potential of 25V) was 1.0845. The D+G mode or 2D mode is a second order mode that is found close to 2684 cm^{-1} . This is shown in **Figure 4-16**. These figures all show a response in the RBM-mode of the spectra, indicating vibrational response commonly seen in carbon nanotubes. Additionally, the strength of the D and G-modes are similar to one another, while the G-mode seems much larger than the 2D-mode.

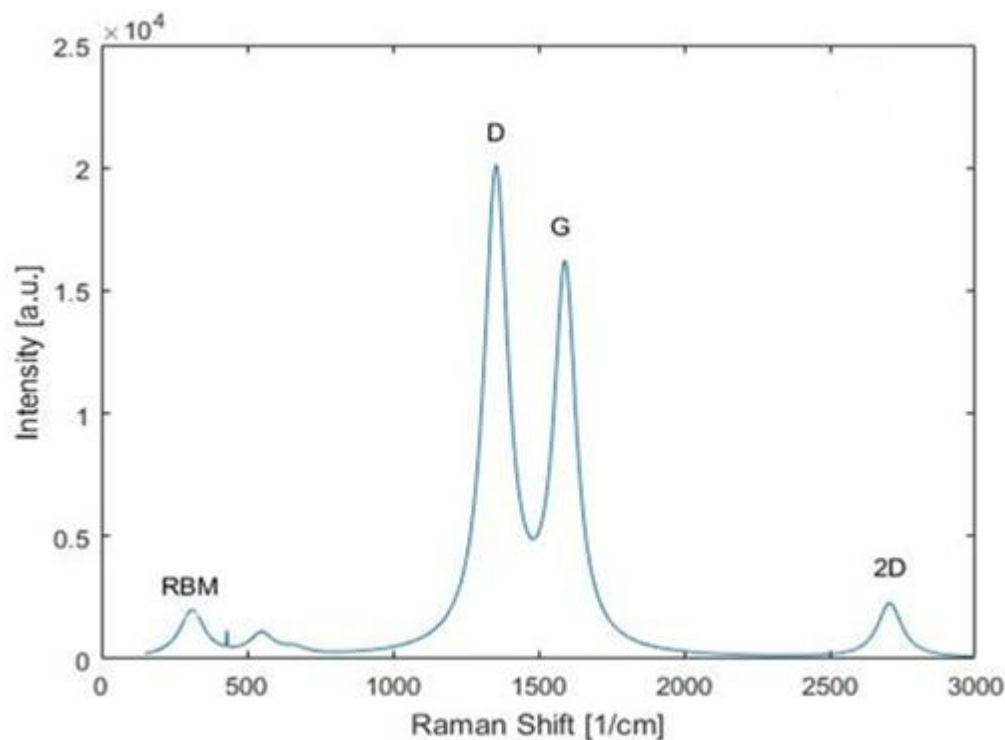


Figure 4-16: Raman spectra after peak fitting and baseline removal.

As can be seen in **Figure 4-16**, the D-mode peak, or first order overtone, shows up at 1300 cm^{-1} , indicating disorder within the sp^2 bonds. This is due to distortion within the graphene structure of the nanoscrolls. At around $1580\text{-}1590\text{ cm}^{-1}$, the G-mode, or second order overtone, of graphene represents the stretching or flexing of the graphene C-C bonds. The fact that these are split may represent impurities within the graphene. The D+G mode or 2D mode is a second order mode that is found close to 2700 cm^{-1} . This mode is helpful for determining the number of layers. As the G-mode is much higher than the 2D mode, it would seem as if there are multiple layers within the nanoscrolls. Additionally, the vibrational modes in the RBM bands in around $150\text{-}400\text{ cm}^{-1}$ suggest carbon nanotube-like

behavior. Indeed, the strength of the G-mode compared to the 2D mode would strongly suggest carbon nanotube-like properties from the nanoscrolls.

4.8.3 Cyclic Voltammetry

Cyclic Voltammetry was conducted with graphite electrode as the counter electrode, with a platinum wire as the working electrode along with Ag/AgCl reference electrode. The scan rate was 20 mV/sec during processing. **Figure 4-17a** is the 0.1M SDS solution without any graphene suspensions in the solution. The inset of **Figure 4-17a** shows the cathodic reaction with the water in the solution occurring at the platinum electrode due to no formation of graphene nanosheets in the SDS solution. **Figure 4-17b** is 0.1M SDS after running for six hours at 10V. Graphene nanosheets suspended in the solution make it more electrochemically stable reducing the cathodic reactions of hydrogen evolution at the platinum electrode. **Figure 4-17c** and **Figure 4-17d** are 17.5V and 25V respectfully show similar structure except for an increased current density and shift in the anodic reaction. After graphene nanosheets are produced in the SDS solution the anodic reaction initially becomes sharper and shifts to the more positive direction indicating more graphene being produced at these potentials.

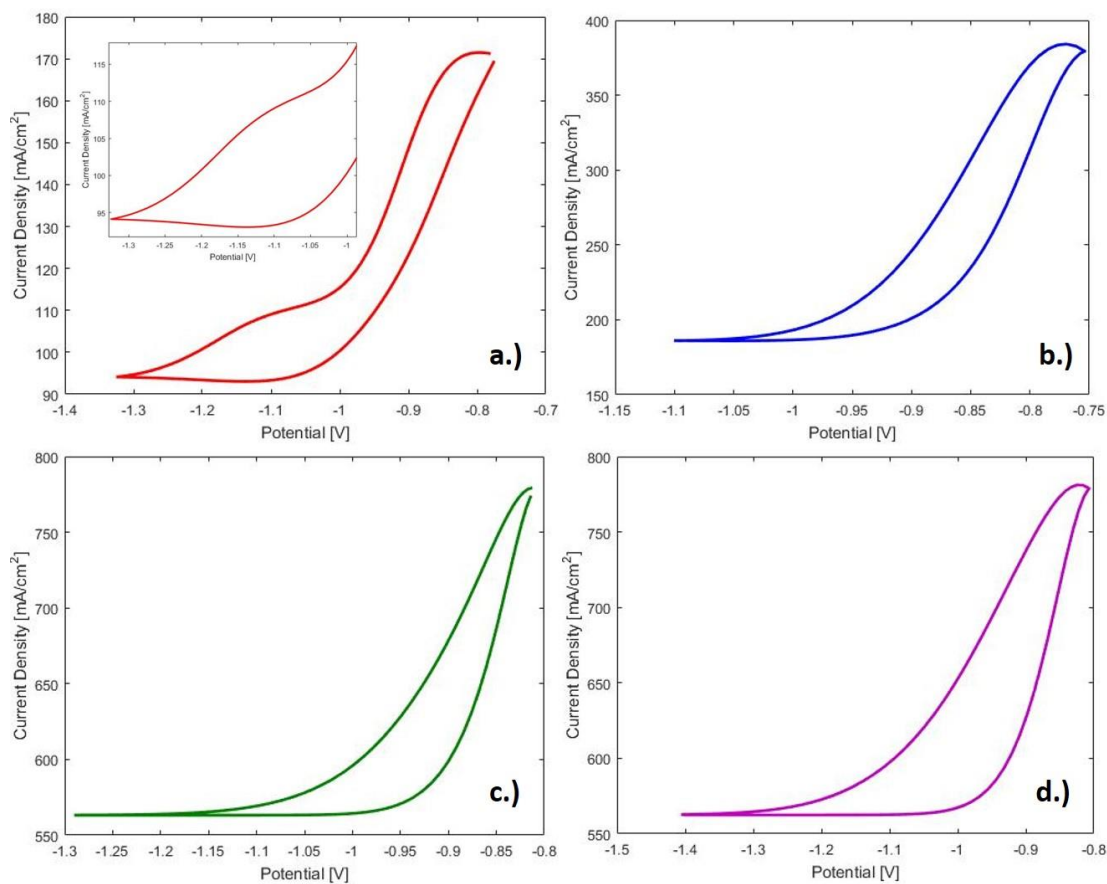


Figure 4-17: Cyclic voltammetry for a.) 0.1M SDS only, b.) with suspended graphene nanosheets 10V potential, c.) at 17.5V, and d.) at 25V potential.

4.8.4 UV-VIS Analysis

UV-VIS spectroscopy was conducted for samples exfoliated at potentials of 10V, 17.5V and 25V shown in **Figure 4-18**. The SDS solution background was removed by the spectrophotometer during processing of each sample. As the exfoliation potential is increased the absorbance increases resulting in more graphene nanosheets suspended in the SDS solution. The maximum peak for both the 17.5V and 25V is located at 212nm.

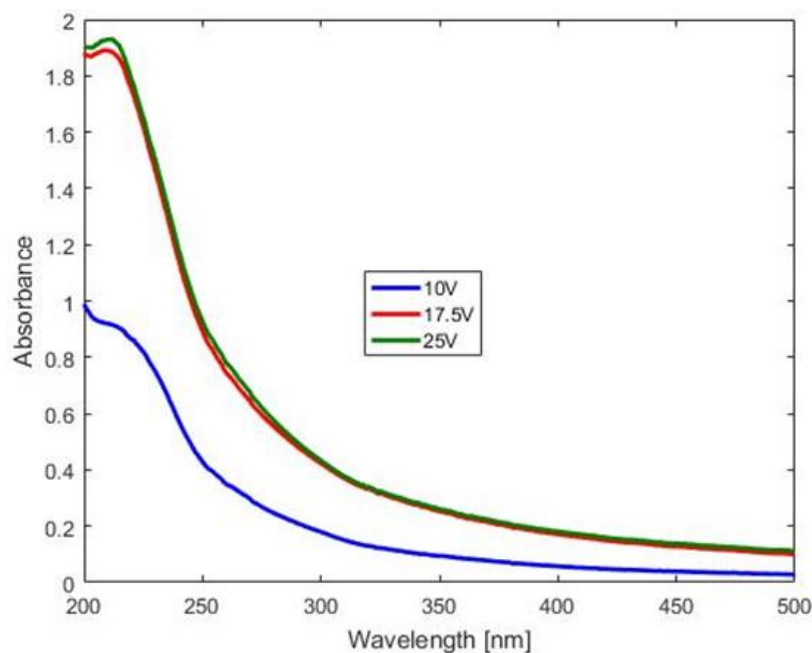


Figure 4-18: UV-VIS analysis at potentials of 10V, 17.5V, and 25V.

4.9 Loaded Graphene Nanoscroll Reactor Testing

During research into exfoliation electrolytes, potassium hydroxide was used in a highly basic pH 13 aqueous solution. Graphene made in this method was cleaned and ultrasonicated into graphene nanoscrolls. When graphene and graphene nanoscrolls were studied under TEM for morphologies, it was discovered that they had been decorated with potassium metal particles. This led to the exploration of the use of graphene nanoscrolls as supports. Graphene nanoscrolls have a high surface area, similar to carbon nanotubes (CNTs). Due to the inherent stresses of the curved planes of graphene that make up both carbon nanotubes and graphene nanoscrolls, the electronic states of the graphene nanoscroll are thought to aid in the activity of catalysts. This raises the possibility of their use as an active support layer for catalytic reactions [158]. Due to these factors, they were

utilized as supports for nickel nanoparticles for dry reforming catalysts. **Figure 4-19** and **Figure 4-20** shows potassium decorated graphene in the process of scrolling and loaded graphene nanoscrolls.

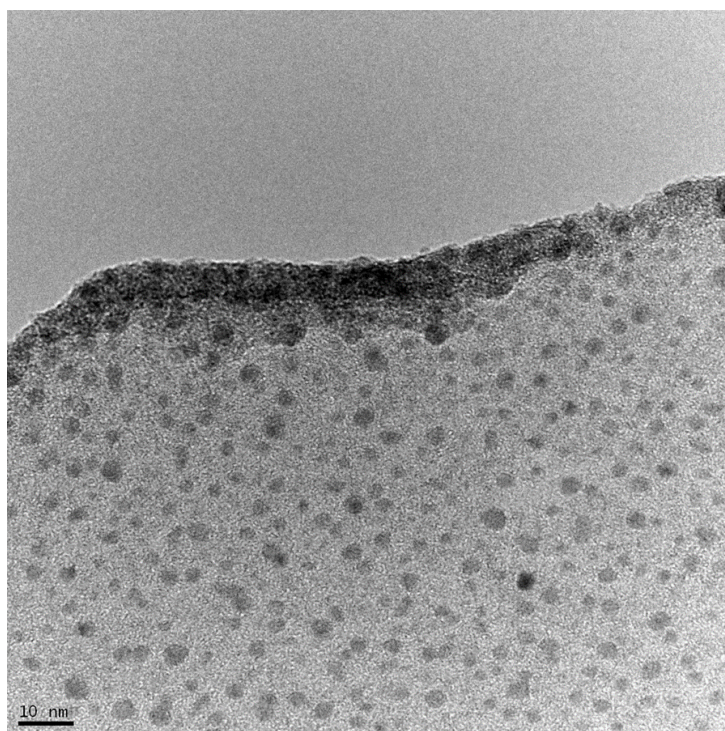


Figure 4-19: Potassium decorated graphene in the process of scrolling.

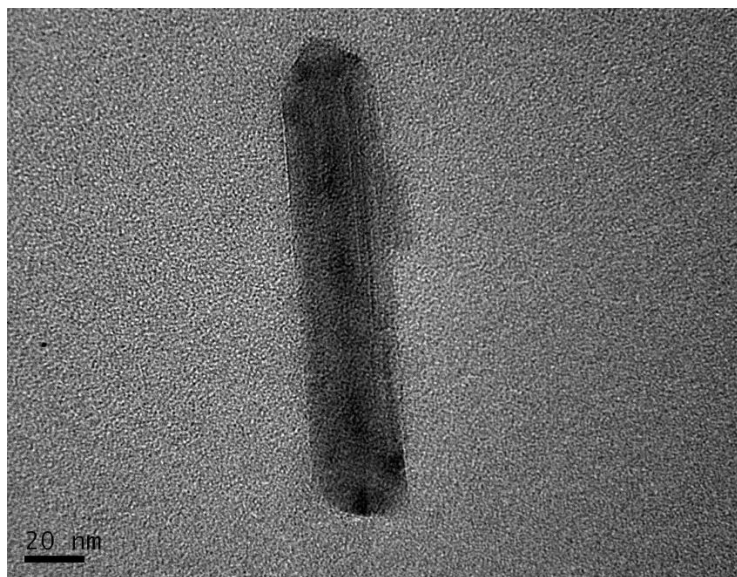


Figure 4-20: Graphene nanoscroll loaded with potassium nanoparticles.

Graphene nanoscrolls were loaded with nickel using an aqueous solution of 20% nickel nitrate. This was conducted using a vacuum loading technique. First, 5 ml of graphene nanoscrolls from solution were added to a 5 ml of 6% wt nickel nitrate solution. This was then placed under vacuum at 25 Torr and 60° C of heat. After 24 hours, this solution was washed and 5 ml of 6% wt nickel nitrate were added again. The solution was then placed back under 25 Torr and 60° C of heat for 24 hours.

After the final 24 hours had passed, 3.5 g of γ -alumina pellets were added to the solution which was absorbed into the pores of the pellets. These pellets were then dried at 100° C in an Erlenmeyer flask until there was no condensation formed on the sides of the Erlenmeyer flask or about 8 hours. The pellets were then calcinated in a burnout furnace to 500°C to transform the nickel nitrate into nickel. The pellets were then loaded into the reaction chamber for reaction testing.

Similar to the nanofiber-based catalysts, reactions were carried out over 3 temperature setpoints; 700°C, 800°C, and 900°C. At each temperature range, the active time on stream at the temperature was set to 3 hours with GC readings approximately every 15 minutes. The input gases were set at 30 sccm per minute for CO₂ and 20 sccm of methane (1.5:1 ratio of CO₂:CH₄). **Figure 4-21** and **Figure 4-22** show the evolution of gases of CH₄, CO and H₂ over time at 700°C and 800°C.

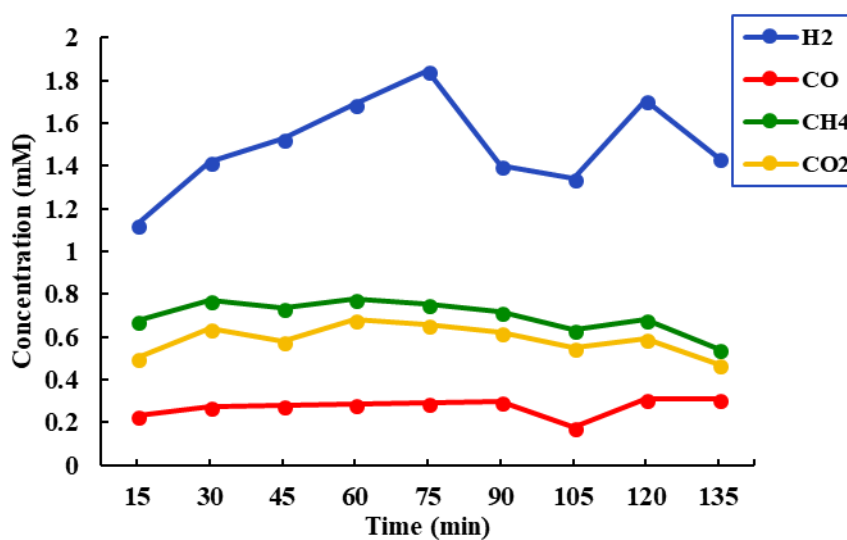


Figure 4-21: Gas evolution at 700°C for nickel loaded graphene nanoscrolls.

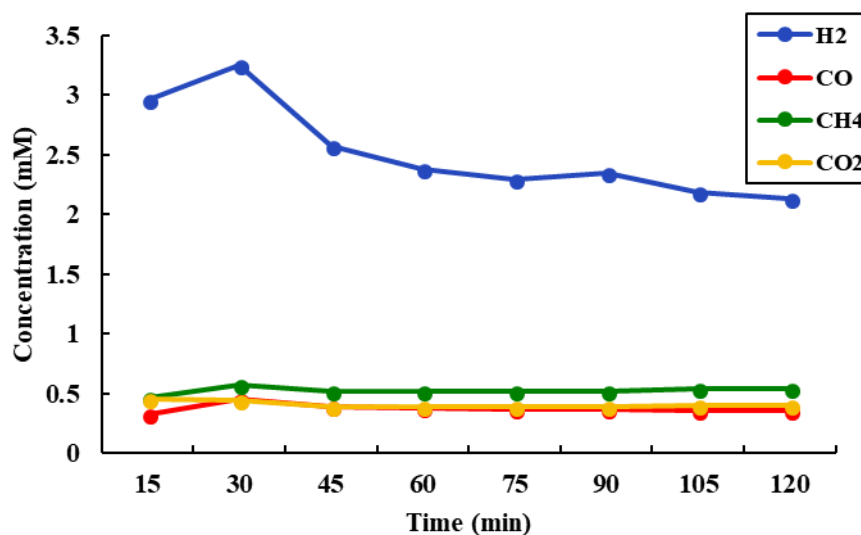


Figure 4-22: Gas evolution at 800°C for nickel loaded graphene nanoscrolls.

As shown in **Figure 4-21** and **Figure 4-22**, methane starts at an average of 0.7 mM during the 700 °C test run and falls by 25.29 % during the 800 °C test run. This is also shown in the carbon dioxide levels which decrease by 31.03% on average between the 700 °C and 800 °C test runs. During the 800 °C test run, hydrogen sees a 27.9 % decline in concentration starting 30 minutes after the measurement phase started at the end of the test run. The dip in products is also reflected in the carbon monoxide, which shows a decrease in concentration from the start of the test run by 21.36 % by the end of the run.

Figure 4-23 shows the reaction over time at 900 °C.

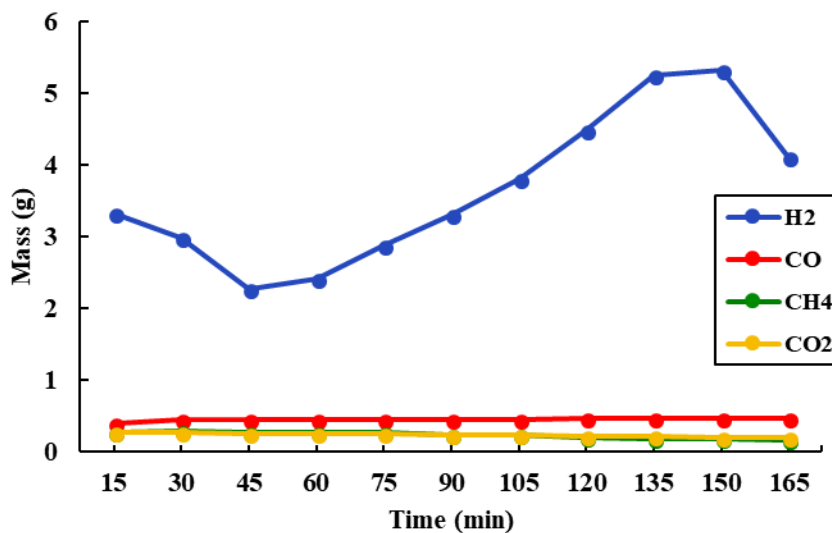


Figure 4-23: Gas evolution at 900°C for nickel loaded graphene nanoscrolls.

Figure 4-23 shows the 900 °C test run, with high conversion of the reactants that slowly decrease in concentration, by 40.6 % for methane and 23.36 % for carbon dioxide, over the runtime indicating a ramp-up of activity in the catalyst. The products see similar rises in concentration with carbon monoxide showing steady increase by 17.94 % increase during the testing period. Hydrogen is more mobile but starts to show a decline in the last measurement. The rapid changes in hydrogen are most likely due to retention time within the nanoscroll, which can experience hydrogenation at high temperatures [146]. Below, the methane conversion of selected catalysts is shown compared to the GNS/Ni catalyst in **Figure 4-24** while the conversion of carbon dioxide is shown in **Figure 4-25**.

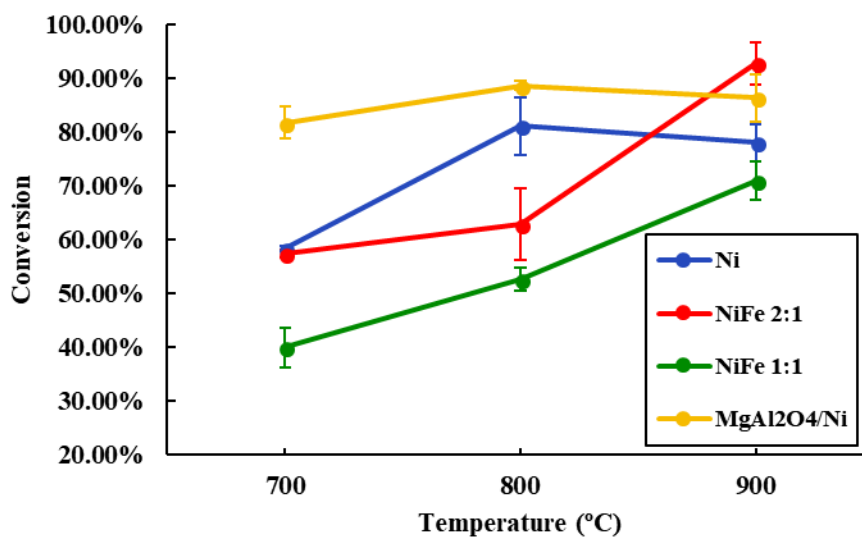


Figure 4-24: Average methane conversion percentage of select catalysts.

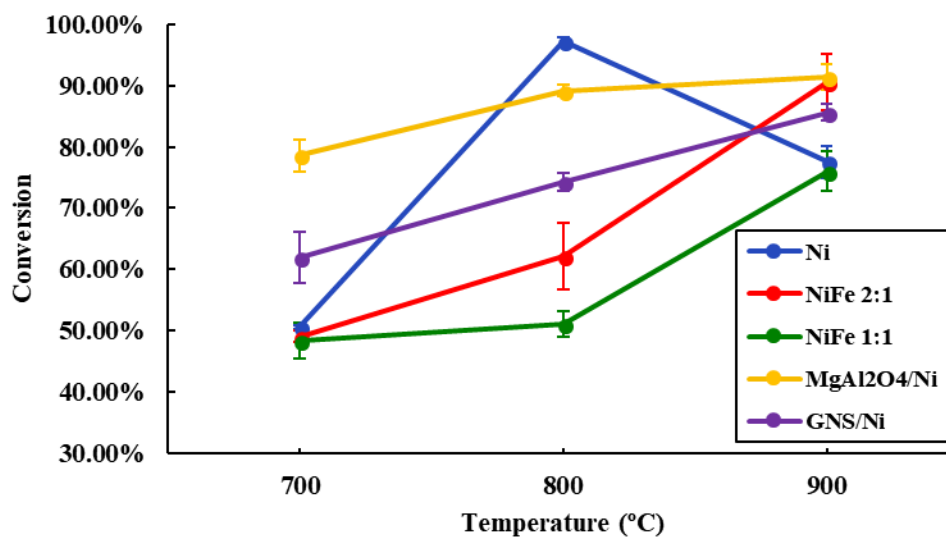


Figure 4-25: Average carbon dioxide conversion percentages for graphene nanoscrolls and other catalysts.

While methane conversion was higher for the nickel ferrite 2:1 catalyst at 900 °C, the GNS/nickel catalyst had higher conversion rates at the lower two temperatures at 64.68 % and 73.6 % for the 700 °C and 800 °C test runs, respectively. The activity of the GNS/nickel catalyst is very linear both in methane, where it shares linearity with the traditional nickel catalyst and in carbon dioxide conversion. After the conversion was calculated at each test run temperature, the GNS/Ni catalyst was then run at 800 °C for 6 more hours, and samples of initial catalyst were compared to samples taken at the 9-hour and 15-hour mark respectively. These samples were studied using the SEM and with EDAX to observe the carbon content of the samples. **Figure 4-26** shows nickel loaded graphene nanoscrolls on the surface of a γ -alumina pellet highlighted by the red circle.



Figure 4-26: Graphene nanoscrolls on the surface of the alumina pellet.

The loaded graphene nanoscrolls were difficult to observe under SEM due to the charging of the metal and the magnetic nature of pure nickel. The coating and drying process caused some clumping on the pellet, and there are areas with fewer graphene nanoscrolls and correspondingly lower carbon content. Additionally, a larger graphene platelet that is half scrolled can be seen here with nickel deposited in it. The EDAX of this feature showed a high carbon content, as shown in **Figure 4-27**.

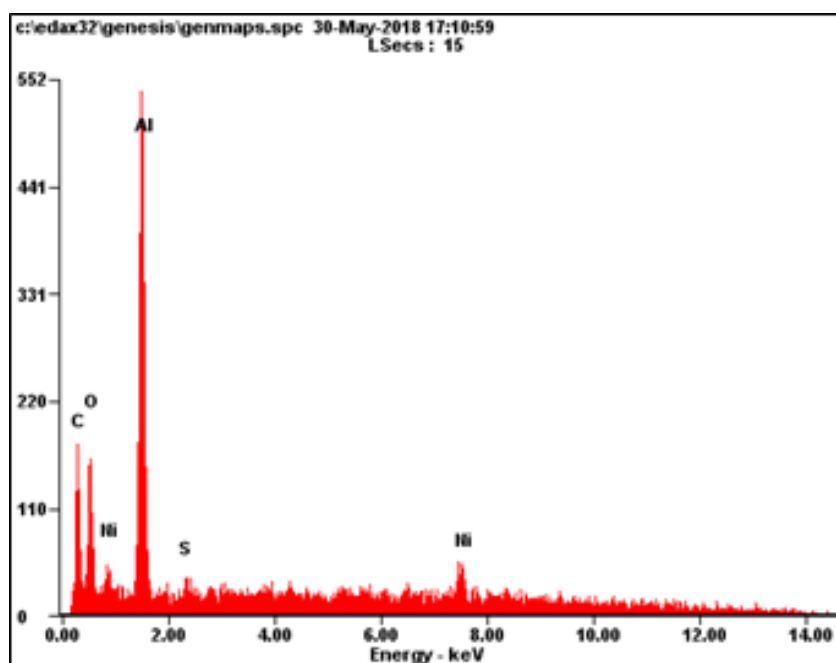


Figure 4-27: EDAX of loaded graphene nanoscroll cluster.

During the drying of the nanoscrolls on the surface of the alumina pellet, clumping of the GNS occurred. Areas with less GNS were explored using EDAX as well, and a high disparity was discovered between the carbon content of areas with and without GNS clusters. **Figure 4-28** shows an EDAX of this area.

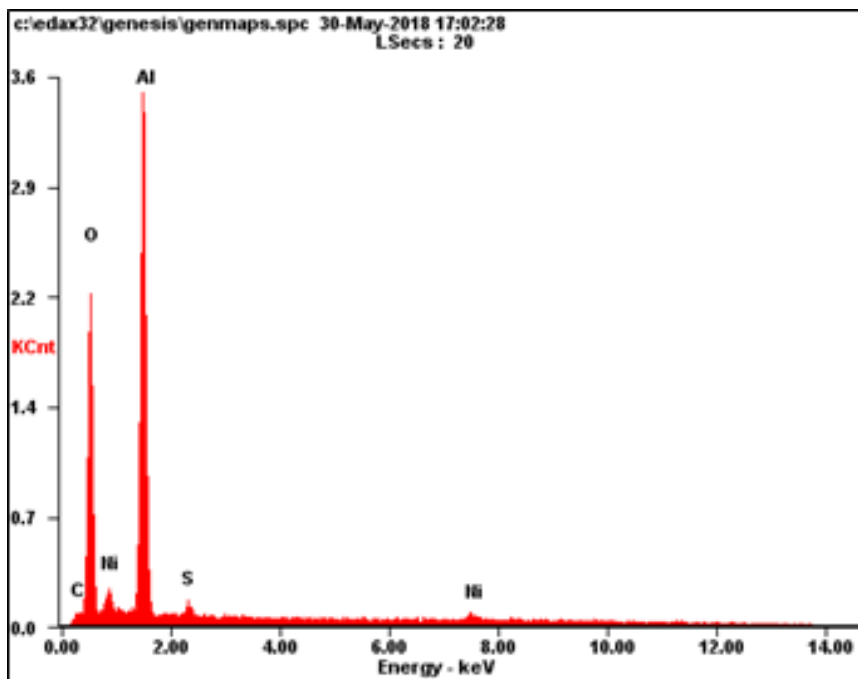


Figure 4-28: EDAX of the area without GNS clusters.

As seen in **Figure 4-28**, the carbon content is significantly diminished. Sulfur is also seen in both EDAXs likely due to incomplete separation of the sodium dodecyl sulfate used in the exfoliation process of the graphene nanoscrolls. The sulfur content is slightly lower in the clusters than outside showing that the SDS was likely released from the interior of the nanoscrolls during the loading of nickel. **Table 4-3** shows numerical data associated with **Figure 4-27** and **Figure 4-28**.

Table 4-3: Elemental analysis of nickel loaded GNS on alumina pellet.

Element	W/O Cluster wt%	W/O Cluster at%	W/ Cluster wt%	W/ Cluster at%
Nickel	7.69	2.75	17.04	5.11
Carbon	3.70	6.46	41.60	60.95
Sulfur	1.62	1.03	1.36	0.75

As shown in **Table 4-3**, the sulfur content remains lower at 1% or lower throughout the pellet, while carbon shows a difference of 163.457% by weight (158.81% by atomic percentage) and nickel shows a less pronounced difference of 88.55% by weight (77.78% by atomic percentage) between the GNS cluster and non-cluster areas. After this, the sample taken after 9 hours of run time was observed. This sample shows a much more uniform distribution of carbon across the surface of the pellet. This is due to the coking of the pellet during the 9 hours of run time. **Figure 4-29** shows an SEM image of the surface of a pellet after 9 hours of runtime.



Figure 4-29: SEM of GNS/Ni pellet at 9 hours on stream.

The SEM image in **Figure 4-29** shows clear coking as well as a whisker formation. Additionally, the formation of the round carbides found on the nickel catalyst is not present on the surface of the pellet. After SEM imaging, EDAX readings were taken for the 9 hours on stream pellet. The EDAX of this SEM image is shown in **Figure 4-30** below.

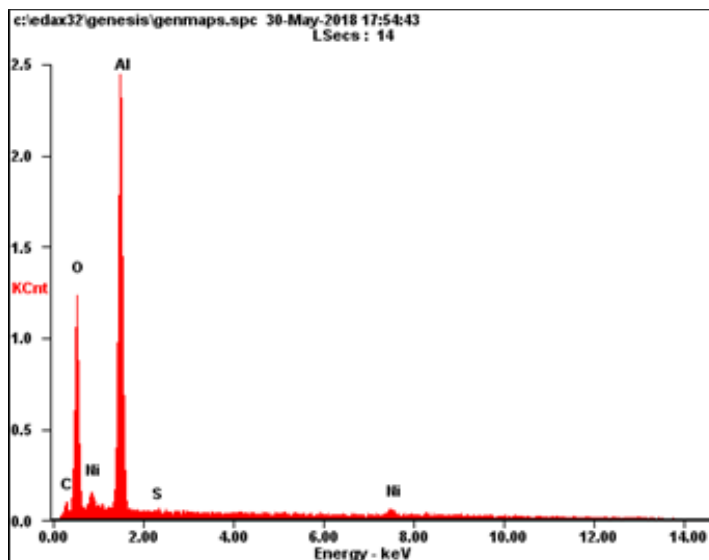


Figure 4-30: EDAX of GNS/Ni pellet after 9 hours on stream.

Here we have a small amount of carbon compared to nickel content. This pellet also had almost no sulfur in the background indicating the removal of any dodecyl sulfate that might have been stuck inside of the graphene nanoscrolls. Here, carbon is about 10.08 % wt, a 172% increase from non-cluster areas. After the EDAX reading for the 9 hours on stream pellet was taken, the 15 hours on stream pellet was studied under SEM imaging. This is shown in **Figure 4-31** below.

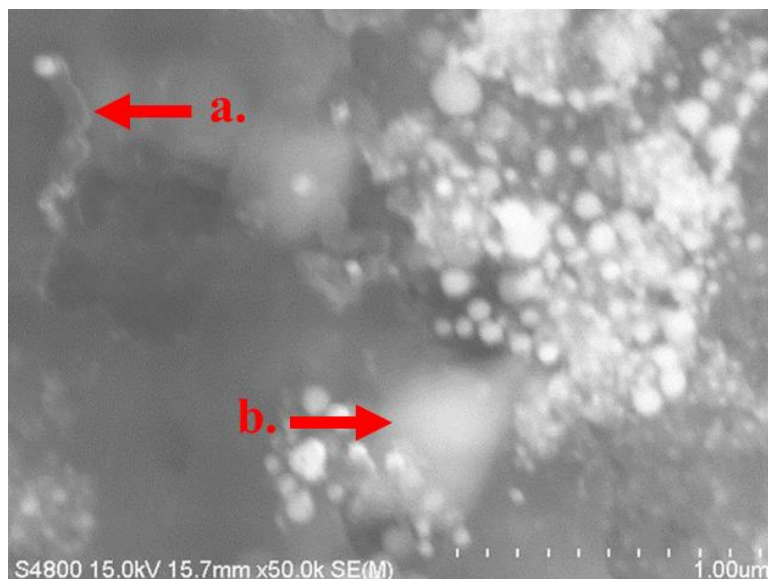


Figure 4-31: GNS/Ni pellet after 15 hours on stream.

As shown in **Figure 4-31**, there is evidence of nanoscrolls (a.) and graphene formation (b.) on the surface of the pellet. There is also a high amount of carbon in all areas, indicating a greater amount of coking. Examining the pellet under EDAX again, it is shown that there are still differences between the clustered GNS/Ni areas and the pellet areas, though the differences are less pronounced. As shown in **Figure 4-32**, the pellets surface has some nickel and carbon buildup from the initial readings, while **Figure 4-33** shows an EDAX of a GNS/Ni cluster.

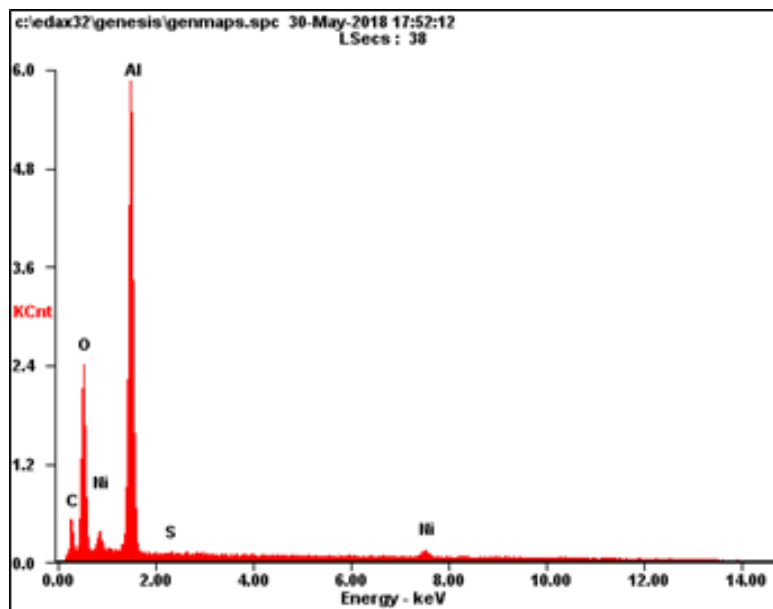


Figure 4-32: EDAX of GNS/Ni pellet after 15 hours on stream.

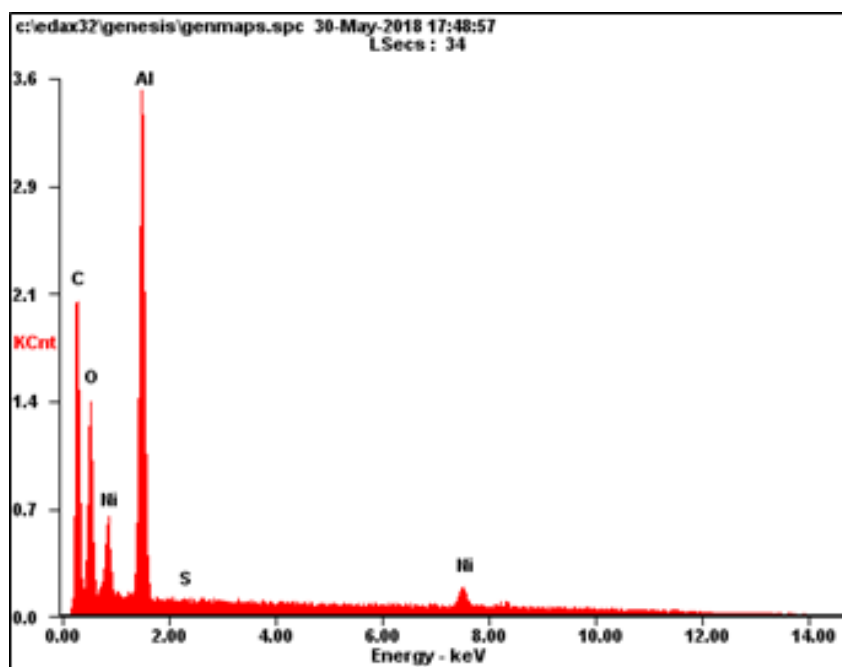


Figure 4-33: EDAX of GNS/Ni cluster after 15 hours on stream.

As can be seen in **Figures 4-32** and **4-33**, there is a significant difference in the amount of carbon on and off of the clusters. This difference is shown in **Table 4-4** below.

Table 4-4: Elemental analysis of GNS/Ni on pellet after 15 hours on stream.

Element	W/O Cluster wt%	W/O Cluster at%	W/ Cluster wt%	W/ Cluster at%
Nickel	7.45	2.45	9.42	2.52
Carbon	14.17	22.76	50.46	66.05
Sulfur	0.12	0.07	0.12	0.06

That's a difference of 112.3% between the clusters and the surface of the pellet on carbon, which is a decrease of 51.157% from the pellet that was studied before being run. Additionally, there is a carbon increase of 40.57% on the non-cluster areas from 9 hours to 15 hours and a total of 152% increase from the before run pellet, indicating that most of the coking occurring had occurred in the first 9 hours of on-stream time. The increase from the clusters from initial to final is only 21.29% which shows lower coking rates directly on the catalyst. A visual inspection of the pellets taken at the start, 9 hours and 15 hours shows the buildup of coke on the surface of the catalyst. This is shown in **Figure 4-34** below.

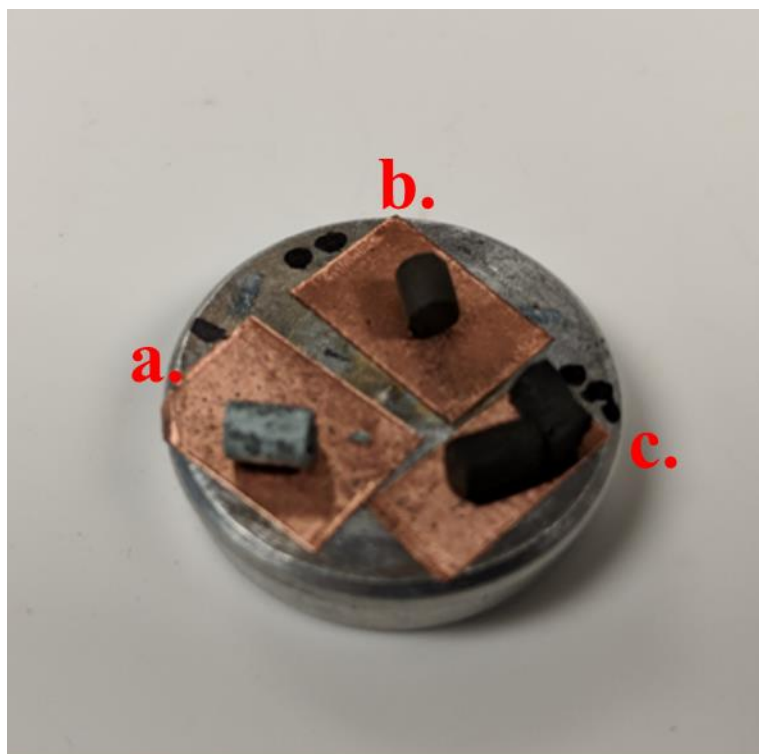


Figure 4-34: Visual inspection of pellets (a.) before reaction, (b.) after 9 hours, and (c.) after 15 hours.

Reaction rates were calculated for reactants based on their rates of consumption and products based on rates of production at different temperatures. The reaction rates for the GNS/Ni catalysts were determined according to Eq 3.16 through Eq 3.19 and used to find the apparent activation energy of the dry reforming reaction with respect to methane and carbon dioxide. The natural log of the reaction rates of methane is shown in **Figure 4-35** while the natural log of the reaction rates of carbon dioxide is shown in **Figure 4-36** below.

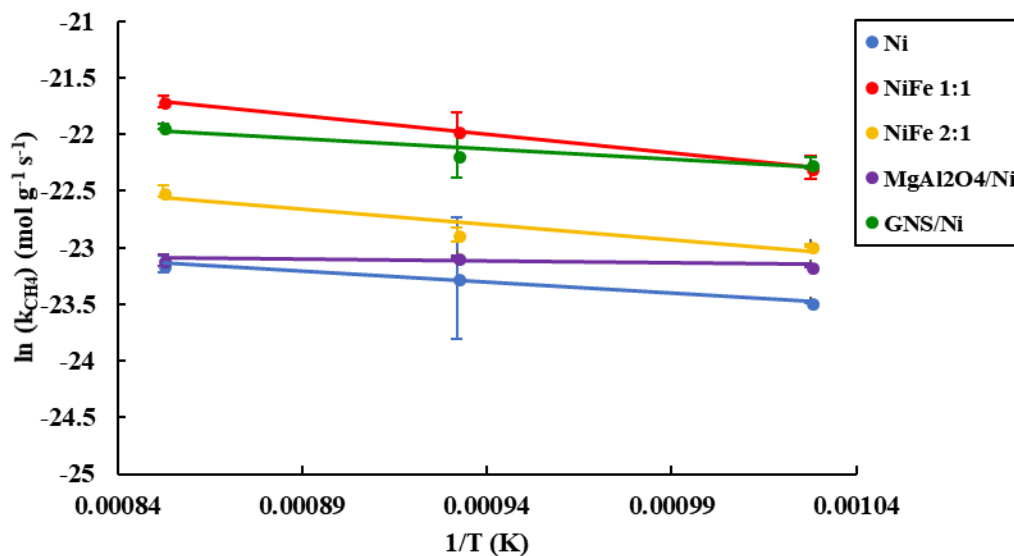


Figure 4-35: Natural log of reaction rates of methane.

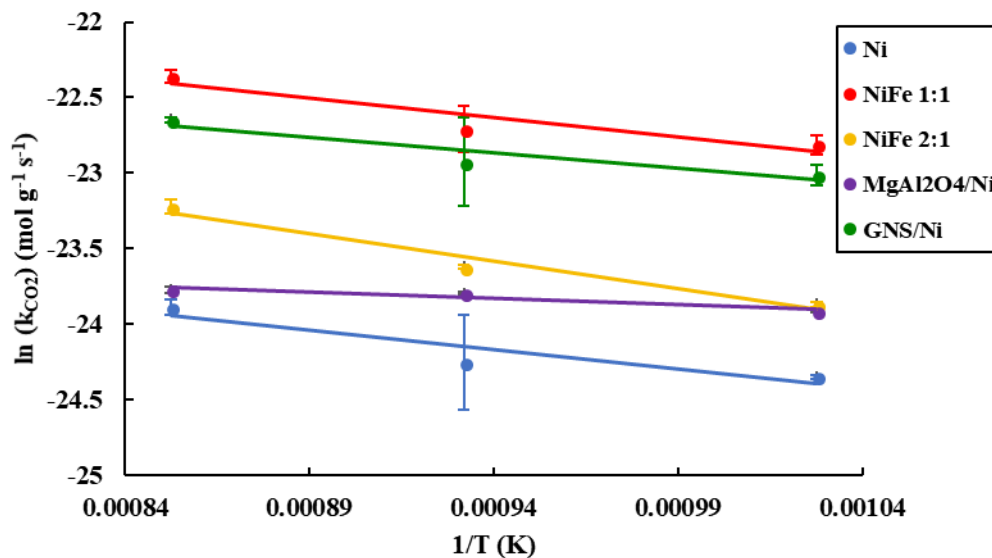


Figure 4-36: Natural log of reaction rates of carbon dioxide.

The slope of these graphs corresponds to E_{aa}/R with R being Boltzmann's constant.

This is then used to find the apparent activation energy, E_{aa} , for the nickel loaded graphene

nanoscrolls which are 14.96 kJ/mol for methane and 16.93 kJ/mol for carbon dioxide. This is in good agreement with other nickel-based catalyst apparent activation energies stated in literature, except with a lower apparent activation energy for carbon dioxide, indicating a preference towards the carbon dioxide dissociation intermediate step [159]. Coking on the catalyst, both on and off the graphene nanoscroll cluster, showed a better rate of coking resistant than carbon deposition on carbon nanotube catalytic supports found in Ma *et al.*, who showed a 20.8 %wt change in carbon content on the CNT catalysts after 8 hours of reaction testing, while the GNS/Ni catalyst showed a 21.29 % wt change from initial carbon content after 15 hours of reaction testing [158]. Graphene nanoscroll supports were excellent at resisting carbon buildup, as the GNS/Ni catalyst was measured as the lowest amount of carbon deposition of the tested catalysts, 12.17% lower at% carbon than the NiFe 1:1 nanofiber over the same amount of reaction time. This makes the graphene nanoscroll supported nickel nanoparticle catalysts the best at resisting coking of the catalysts tested.

4.10 Summary

Bulk electrochemical fabrication methods for graphene were studied and characterized using several different methods to test the layering of the graphene produced in this method with good agreement with graphene produced through mechanical exfoliation. Additionally, graphene from this method was used to create nanoscrolls with lumens of 40 nm, much larger than typical carbon nanotubes. These graphene nanoscrolls were used as supports for nickel in the dry reforming reaction. The reaction was run at several setpoints for 3 hours each and then set at 800 °C for an additional 6 hours of runtime. Samples were taken at specific intervals and studied under SEM and EDAX for

coke formation and morphological characterization. Gas chromatography was used to determine methane conversion and find the rates of reaction for carbon dioxide and methane. Finally, the reaction rates were used to find the experimentally determined apparent activation energy of the reactions. The apparent activation energy of the catalyst is in the regime of the nanofiber catalysts and lower than the traditional nickel catalyst prepared by the wetness impregnation method, and the coking rate was the lowest of all the studied catalysts, making the nanoscrolls a viable alternative to carbon nanotubes as a support for the dry reforming reaction and offering a low cost, scalable nanostructured support option that is highly resistant to carbon buildup.

CHAPTER 5

METAL OXIDE NANOFIBER GAS SENSORS

5.1 Introduction

Chemiresistive gas sensors utilize chemicals that change resistance in response to chemical changes in the surrounding atmosphere. This is caused by the chemical interaction between the introduced gas and the sensing material. Metal Oxide semiconductors (MOx) can operate as chemiresistive gas sensors due to the changes that happen due to reduction and oxidation by gases. Thin films of these materials are commonly used as MEMs based chemical sensors, but they typically require introduced energy in the form of heat to replenish the sensor with oxygen [164-166].

As chemiresistance is a phenomenon that happens on the surface of a sensing material, nanomaterials have been shown to be excellent chemiresistive gas sensors due to their high surface area. Research into metal oxide sensors has focused on the high surface area that electrospun nanofibers can provide [159-163]. While these sensors are much more responsive, they still require heat to regenerate. This chapter is focused on the fabrication of passive gas sensors that were made through the mixture of graphene nanoscrolls and electrospun metal oxide nanofibers in a doped polyaniline medium. These sensors were tested using methane, ethanol, and acetone at different concentrations at room temperature.

5.2 Metal Oxide Gas Sensor Operational Theory

Metal oxide sensors respond in the presence of reducing gases and are marked by high response sensitivity and low regeneration time. These sensors must be heated to ensure the regeneration occurs though. Due to this, metal oxide sensors require a “warm-up” time while the heating element reaches operational temperature. Metal oxide sensors are warmed up in the air, and then as a reducing gas flows over them, experience a measurable change in resistance. Additionally, metal oxides can have different oxidation states that can change the effect of the reaction sites within sensors [167]. Current state-of-the-art MOx sensors use a thin film of metal oxide because higher surface area results in higher response. It is a natural extension of the electrospun nanofiber technique to produce high surface area structures for higher sensitivity gas sensors. A schematic showing how nanofiber MOx sensors operate is shown in **Figure 5-1**.

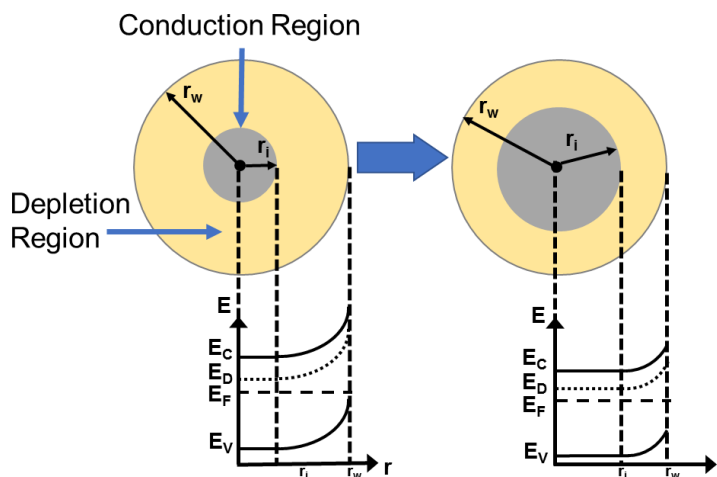


Figure 5-1: Model of metal oxide sensor theory.

5.3 Metal Oxide Nanofiber Fabrication

Nanoscale materials offer an advantage over traditional sensing materials due to their increased surface area [168]. The increased surface area allows for greater surface interaction with the sensed gas; thus, larger surface area allows for more molecular interactions, increasing the sensitivity of the sensor [169]. Further increases to the surface area can be found by the addition of mesopores on the nanofibers, which are further expanded during calcination. On the nanoscale, iron and its oxides exhibit useful sensing properties at lower cost and wide availability. Iron (II, III) oxide (Fe_3O_4), the most stable of iron oxides, has shown itself as a useful gas and humidity sensor when in a nanoparticle or thin film form [170]. Iron oxide nanofibers made via electrospinning have also exhibited acute ferromagnetism [171]. As nanostructured sensors are developed consistent processing and characterization of the nanofabrication process becomes a crucial step in the creation of these next-generation sensors. Indeed, electrospun nanomaterials are already finding their way into MEMS devices as sensing materials [172].

Polyvinyl alcohol (PVA) (MW: 100,000, 87% hydrolyzed, Ward's Science) was mixed with iron nitrate nonahydrate ($\text{Fe}(\text{NO}_3)_3 \cdot 9\text{H}_2\text{O}$, Alfa Aesar) in deionized water to create a polymer/iron solution. The concentration used for the PVA was altered from 10%, 12.5% and 15% wt while the iron nitrate concentration was changed between 3% 5% and 7% wt per PVA concentration. This results in 9 solutions with different concentrations of PVA and iron. The solutions were fed through a peristaltic pump at a variable rate to a blunt tipped syringe needle. A DC high voltage supply was used to apply a voltage to the needle. Another power supply was used to put a DC voltage of -2kV on the metal target for the fibers bringing the voltage of the total system around $\sim 22\text{kV}$. Operational

parameters for the fabrication of the iron nanofibers are given in **Table 5-1**. A positive voltage and pump speed were used to maintain a constant flow of solution. Fibers were then calcinated to obtain high purity iron nanofibers. Calcination was done using an MTI Corporation GSL-1500X-50-UL tube furnace. The samples were placed on alumina trays in the center of the furnace and heated at a rate of two degrees per minute to a final temperature of 700°C. These calcinated fibers were then allowed to cool in the tube furnace.

Table 5-1: Operation parameters of electrospinning setup.

Voltage range on needle:	20kV-21kV
Voltage on target:	-2000V
Pump speed:	0.010-0.012 mL/min
Humidity:	60-64%

A theoretical analysis was done on fiber diameter using known diameters of iron and its two more common oxides, Fe₂O₃ and Fe₃O₄. The molecular weight of PVA, Fe(NO₃)₃·9H₂O, Fe and its respective oxides were used to create the analysis. The amounts of PVA and iron nitrate in the solution were determined by percent weight (%wt) and were altered within 20% of the total mass of the solution while the other 80% wt is water. To find the ratio of the initial and final radii, initial assumptions were that after calcination no PVA remained and only pure iron or one of the two types of iron oxide remained in the nanofiber. Using the %wt of the iron nitrate, the mass of the iron within the PVA/ Fe(NO₃)₃·9H₂O was determined using:

$$Fe(g) = \left(g Fe(NO_3)_3 \cdot \left(\frac{mol Fe in Fe(NO_3)_3}{MW of Fe(NO_3)_3} \right) \cdot MW of Fe \right) \quad Eq 5.1$$

This equation can be used to find the volume of PVA and iron nitrate in the initial fiber as well as the volume of iron in the final product. Taking the total volume of the initial fiber to be the sum of the PVA and the iron nitrate. Assuming that both fibers are the same length allows for a ratio of the two fibers to be taken. Using the ratio of final over initial radii and the material's respective molecular weights and atomic radii, we can determine the size a nanofiber made with different %wt of polymer and iron and corresponding oxides. **Figure 5-2** shows the differences between the two oxides and the pure metals final diameter as the $\text{Fe}(\text{NO}_3)_3 \cdot 9\text{H}_2\text{O}$ is varied with the PVA.

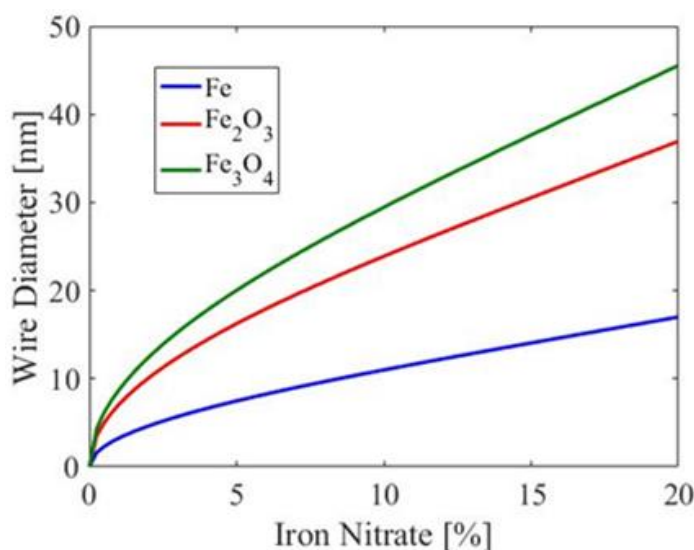


Figure 5-2: Theoretical wire diameters of different iron oxides.

After measurement, fibers were placed in an annealing process that was performed by increasing the temperature of a tube furnace by 3°C a minute until it reached a temperature of 550°C and held there for 3 hours in an air atmosphere to remove PVA via calcination. After cooling, the fibers were again measured under SEM to determine their final diameter. SEM data was obtained for each of the samples. **Figure 5-3** shows the 5%wt

Fe and 15%wt PVA mixture for pre- and post-calcination as an example of the images obtained.

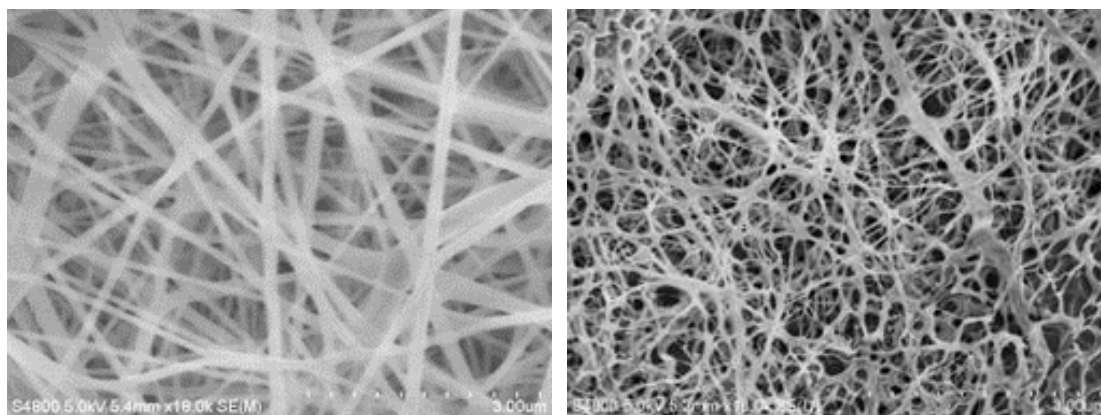


Figure 5-3: Fiber diameter examples pre- and post- calcination.

Using the SEM images, average diameter for fibers were determined by measurements of the width. Pre-calcinated data was collected for all of the samples and averages were used to determine the porosity. The post-calcination images obtained from the 5% FENO₃ and 15% PVA were used to determine diameter loss during the calcination process. Pre-calcination fiber diameter averages are displayed in **Figure 5-4**.

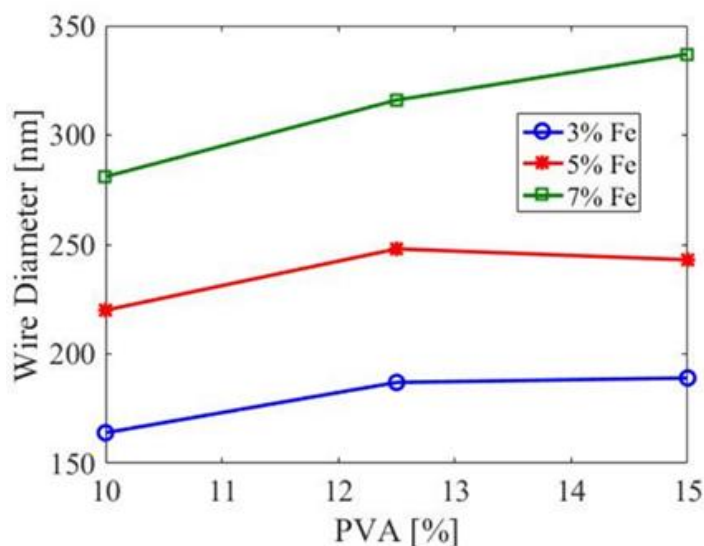


Figure 5-4: Experimental-based average fiber diameters of iron oxide nanofibers.

The average diameter of the post-calcinated fibers was determined to be 32 nm with a standard deviation of ± 12 nm and a standard error of ± 1.41 nm. The error between theoretical non-porous fibers and experimental post-calcined fiber this is 75.4% for the pure Fe fiber, 49.25% error of the Fe_2O_3 fiber and 37.5% for the Fe_3O_4 fiber. The error percentages suggest near total conversion to Fe_3O_4 during calcination as well as mesopore formations within the iron oxide fibers. Conversion of PVA into amorphous carbon may also contribute to the size differences. The transition from PVA/ $\text{Fe}(\text{NO}_3)_3 \cdot 9\text{H}_2\text{O}$ nanofiber to Fe oxide nanoparticle might also involve some measure of conversion into an iron carbide.

The extremely small diameter of the post-calcination fibers, however, indicates a near total loss of PVA in the sample either through evaporation or conversion into amorphous carbon. Use of higher voltage also played a role in the smaller final fiber diameter. Taking the error between the theoretical non-porous fibers and the experimental

post-calcinated fiber as a measure in part of porosity is encouraging as the porosity of the sample will increase the reactivity of the fibers during sensing.

The theoretical analysis found that 5% iron nitrate would produce 7.5 nm to 20 nm depending on the formation of pure Fe or Fe₃O₄ fibers. Looking at experimental results we produced fibers with 32nm diameters on average with only ± 12 nm deviation. These size fibers fall in line with the production of Fe₃O₄, the model has an error of 37.5% which is believed to be accounted for by the development of mesopores during the electrospinning and calcination processes.

5.4 Doped Polyaniline Gas Sensors

Gas sensing materials that utilize a metal oxide thin film or nanomaterial are marked by high sensitivity due to their large surface area. These sensors typically operate at high temperatures requiring a heating element to facilitate the regeneration of the sensor after the sensing event has occurred. To lower the heat and thus the energy required to use these sensors, there has been an exploration of the addition of a conducting medium to increase response and assist regeneration. Organic mediums offer the advantage of both being reactive and enhancing the electrical properties of the sensor.

Polyaniline (PANI) has been the subject of multiple fields of study including solar cells, flexible electronics, batteries, and biosensing. This is due to polyaniline's ease of synthesis, its chemical stability, and its high conductivity. Polyaniline offers an ideal medium for gas sensing due to its oxidation states, the emeraldine salt and base forms, being responsive to gases as well. Research into increasing the selectivity of PANI gas sensors towards certain gases by doping with metal oxide nanoparticles as well, with a

focus primarily on organic gases. Organic gases are some of the most widely used industrial gases today, making it an important topic of research [173].

Research into metal oxide doped polyaniline has led to several room temperature sensor configurations. Additionally, the use of graphene has been shown to increase the response rate of PANI based sensors. There is less research however on the effects of metal oxide loaded graphene nanoscrolls doped into a PANI medium. This research explores the use of metal oxide nanorods made through electrospinning within a graphene nanoscroll doped polyaniline medium for gas sensors. These sensors have been studied for a variety of metal oxides over several organic gases including methane, ethanol, acetone, and LPG [174,175].

Before the metal oxide nanofiber/GNS doped PANI sensors were tested as gas sensors, a MEMS interdigital or “comb drive” array was fabricated to provide a testing apparatus. This array was printed by using gold on chrome on a quartz chip and then a photolithographic method was used to create lines spaced 20 μm apart. Both interdigital arrays had 10 fingers on each side. First (step 1) the borosilicate glass slide is cleaned to remove any dust or organics that may cause problems with the adhesion of the chrome to the quartz. Step 2 is the depositing of the chrome and gold layers using an electron-beam evaporation technique. Once the gold is deposited, the photoresist SU-8 is applied to the surface of the gold in an even layer through spin-coating and then pre-baked at 50°C for 10 minutes (step 3). In step 4, a mask is printed using a mask creation software (Express PCB) and printed on a transparency using an inkjet printer. This mask is aligned over the photoresist and exposed to UV light for 10 minutes in step 5. The exposed photoresist is removed using propylene glycol methyl ether acetate (PGMA), allowing for the unexposed

photoresist to leave the pattern in step 6. Once the pattern was revealed, the sample was placed in a gold etchant to remove the gold not covered by the pattern. After this step, the slide is introduced to gold and chrome etchant and the etchants remove the exposed gold and chrome (step 7). Finally, acetone was used to clean the unexposed photoresist off of the slide, leaving the etched gold surface free. **Figure 5-5** details the step by step photolithography process for the fabrication of the interdigital array.

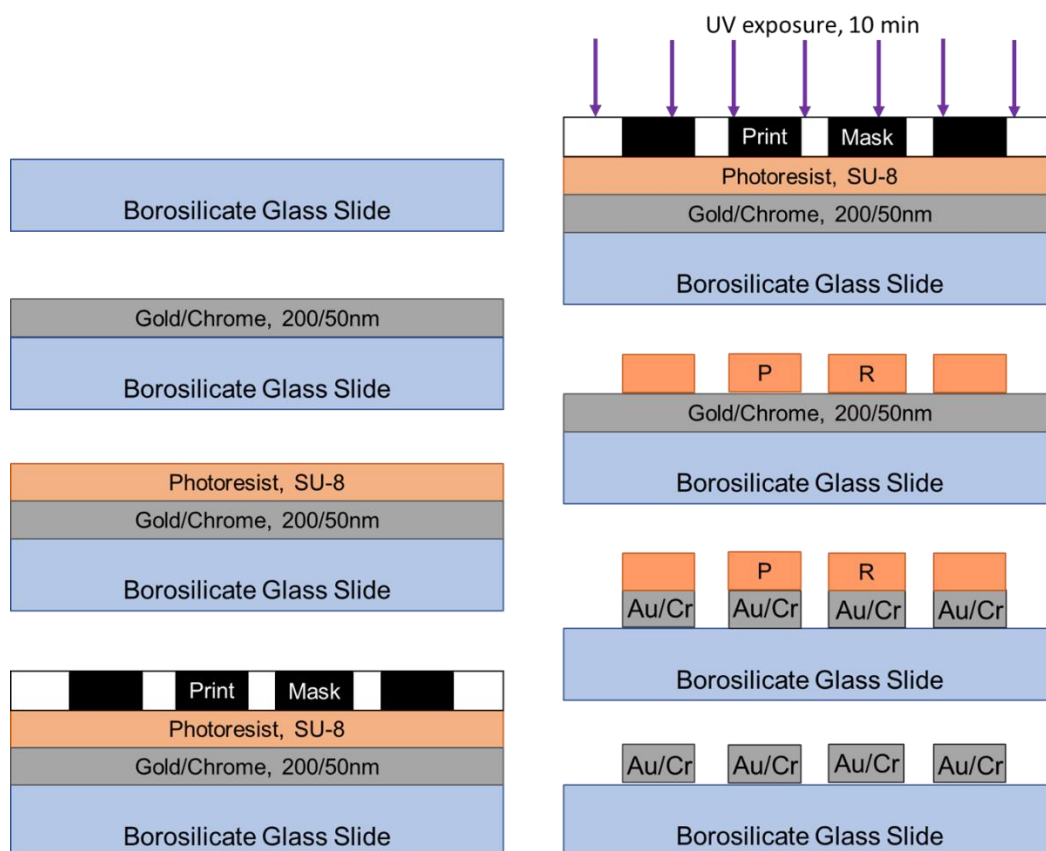


Figure 5-5: Operational steps for fabrication of MEMS gas sensor

To prepare the metal oxide nanofibers, 3 % wt iron nitrate, and 3 % wt nickel nitrate were added into several 10 % wt aqueous polyvinyl alcohol (PVA) sol-gel and mixed for 3

hours. This sol-gel was then electrospun at 20 kV and a 12 cm gap. The nanofibers were collected and calcinated at 500 °C and then crushed into a powder. The graphene nanoscrolls (GNS) produced using a previously published electrochemical followed by ultrasonication technique. Afterward, they were washed and dried. Then, 0.5 g of polyaniline was added to 10 ml of n-methyl—2-pyrrolidone (NMP) and ultrasonicated for 1 hour. To make doped PANI solutions, 0.8 mg of nanofibers and 0.5 mg of GNS were mixed with 3 ml of PANI solution and ultrasonicated for 1 hour. Once mixed, the metal oxide nanofiber, GNS doped PANI blends were applied as a thin film to the surface of an interdigital sensor array. Then, 1 ml of the GNS doped PANI solution and 1 ml of the nanofiber doped PANI solution were combined and ultrasonicated for 1 hour. This nanofiber/GNS doped PANI solution was then drop-cast on an interdigital sensor array. The sensors were then dried in a vacuum oven at 60 °C for 4 hours.

After the fabrication procedure for each MEMs array, the array was allowed to dry and then tested using an Agilent 34401A digital multimeter. The multimeter was connected to a computer running Keysight Technologies Benchvue with multimeter application via an RS-232 serial cable. This setup allowed for quick measurements of resistance over pre-determined times. **Figure 5-6** shows a single interdigital array before the application of nanofibers. The resistance of these arrays was initially tested while in this blank state. The results of the test found that most arrays had a reading of O OVLD on the multimeter, which is shown when the resistance is too large to measure. This confirmed a complete separation of the gold and chrome between the digits.

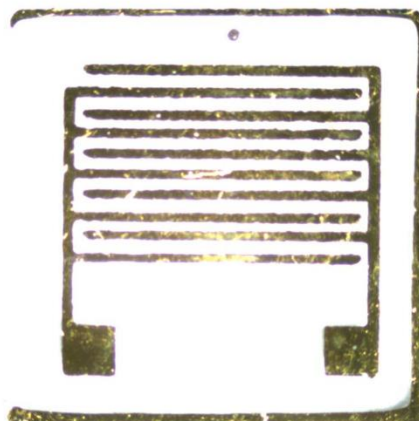


Figure 5-6: MEMS interdigital array, gold on chrome digits are 200 μm wide and spaced 200 μm apart.

After testing the resistance of the baseline arrays, they were coated with the metal oxide nanofiber/GNS doped PANI in a thin film. The sensors were then dried at 60 $^{\circ}\text{C}$ in a vacuum chamber. After drying the surface thickness and roughness of the sensor were studied using a Keyence VK-X150 laser confocal microscope to determine the thickness of the film. **Figure 5-7** shows the height measurements of the thin film sensor.

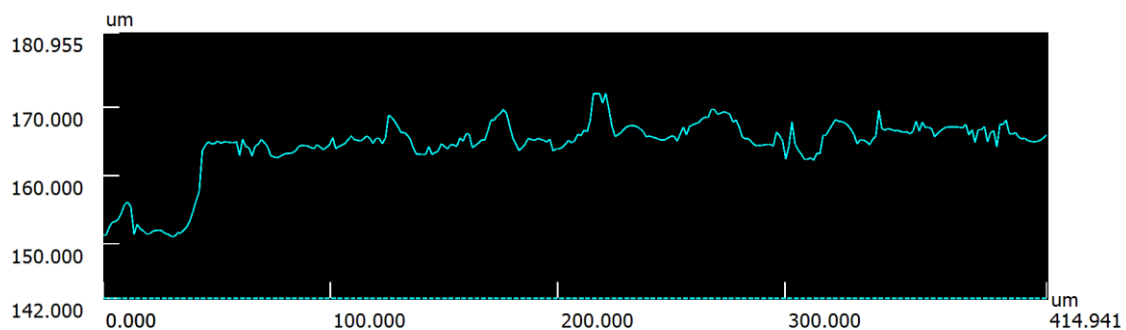


Figure 5-7: Height measurements of the thin film using the laser confocal microscope.

The average height of the thin film shown is 18 ± 4.6 microns as shown in **Figure 5-7**. The consistency of the film was studied across the entire film, and while the study shows small spots where cracks occurred the film was generally consistent. The thickness map is shown in **Figure 5-8**.

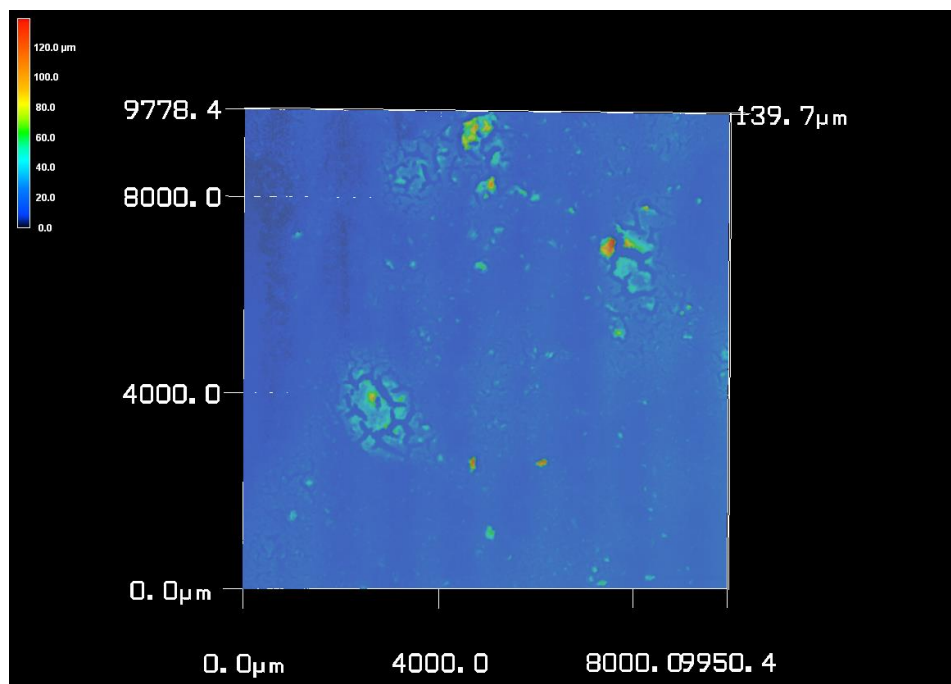


Figure 5-8: 3D height mapping of the sensor/thin film surface using the laser confocal microscope.

The sensors were tested by placing them in a small chamber to slow the rate of release of gas. The test chamber had a volume of 5670 ml, with set airflow of 10 ml/min, and methane was delivered at a set rate in a slow release. The temperature of the test chamber was maintained at 25 ° C. Resistance changes for methane are shown for the nanofiber sensor in **Figure 5-9**, for the graphene nanoscroll sensor in **Figure 5-10**, and for the nanofiber plus graphene nanoscroll sensor in **Figure 5-11**.

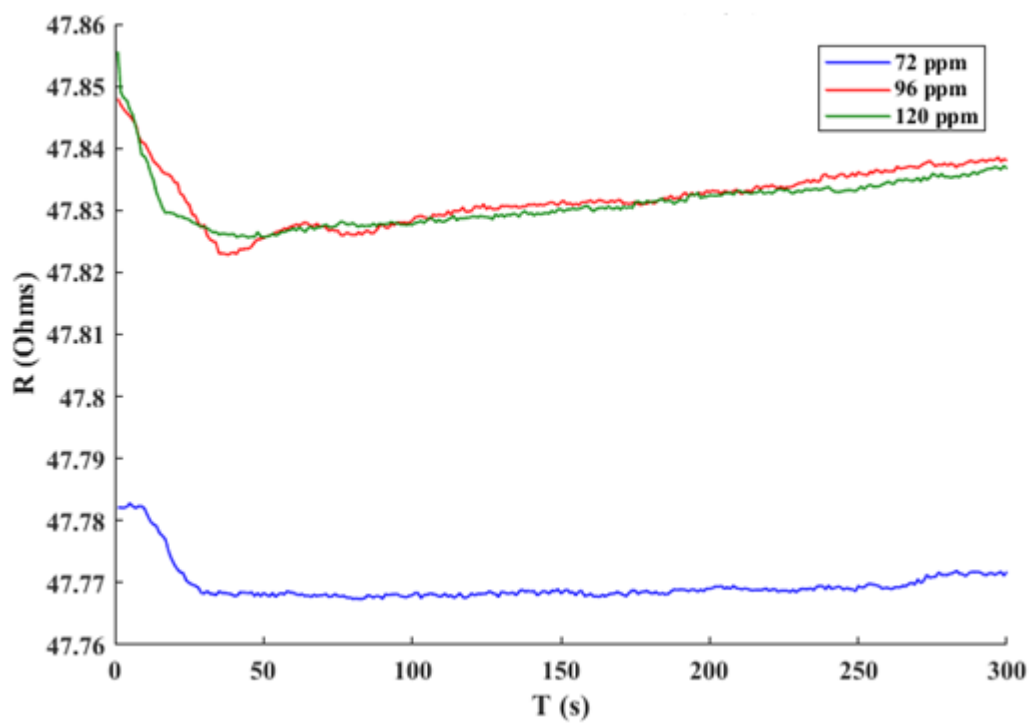


Figure 5-9: Methane response for nanofibers in PANI sensor.

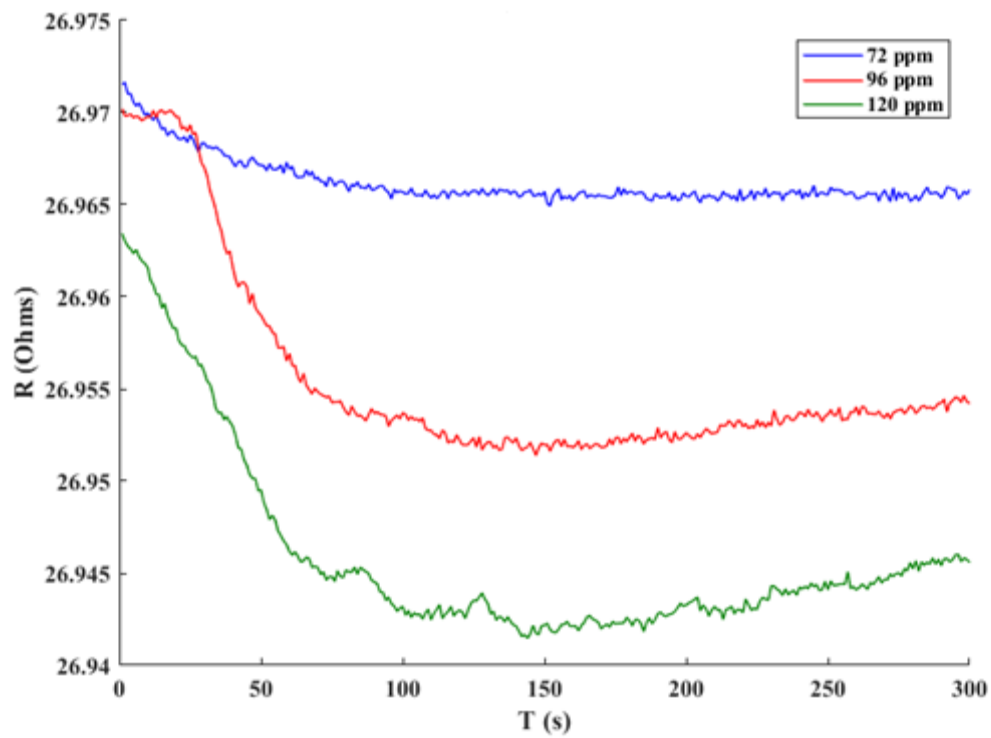


Figure 5-10: Methane response for GNS in PANI sensor.

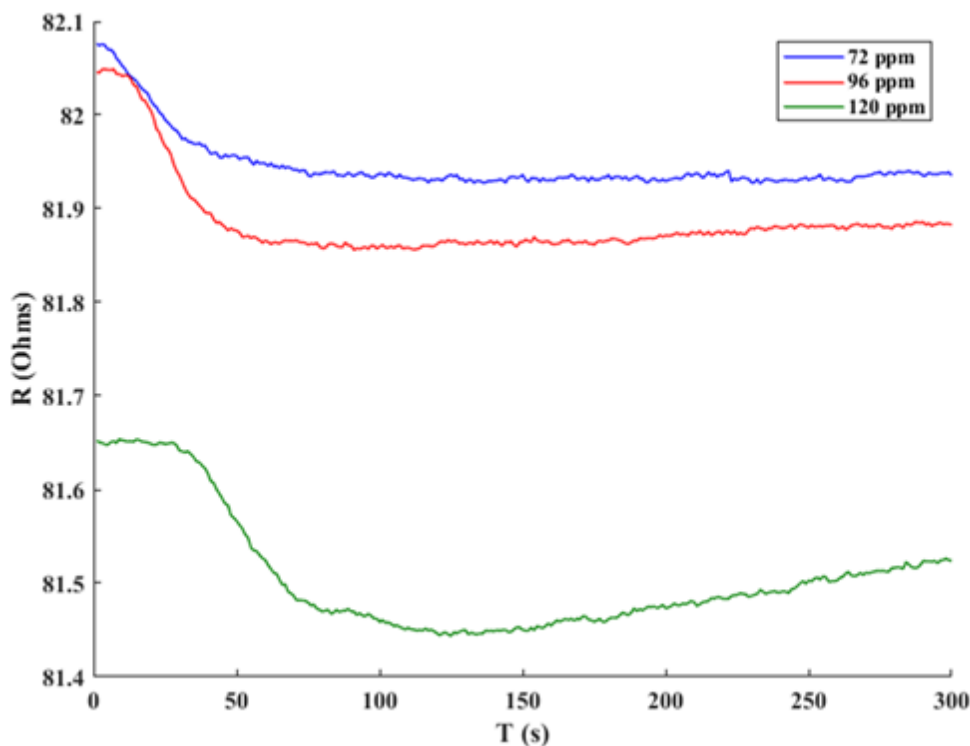


Figure 5-11: Methane response for nanofiber/GNS in PANI sensor.

Sensor response caused a decrease in the resistance as the sensors responded to the reducing gas, methane. The nanofiber sensor response to methane was slower taking 450 seconds to recover to a flat line while the graphene nanoscroll sensor provided a quicker response, reaching its new setpoint by 300 seconds. The nanofiber/graphene nanoscroll sensor had a higher sensitivity to methane but also had recovery times that were similar in time (450-500 seconds) to fully recover. Sensor response is measured by the percent difference between the initial resistance of the thin film surface and the surface during the release of the test gas and is shown by:

$$S = \frac{\Delta R}{R_i} = \frac{R_g - R_i}{R_i} \times 100 \quad \text{Eq 5.2}$$

where R_i is the initial resistance of the sheet and R_g is the resistance during the test gas phase. This response sensitivity is then compared to the calculated levels of gas to find a response per ppm of gas. **Table 5-2** shows the calculated sensitivities of the sensors for methane.

Table 5-2: Calculated sensitivities for methane.

Gas Amount	Nanofiber Sensor	GNS Sensor	Nanofiber/GNS Sensor
72 ppm	0.0313	0.0596	0.1814
96 ppm	0.0524	0.0614	0.2297
120 ppm	0.0625	0.0782	0.2560

Table 5-2 shows that the graphene nanoscroll sensor has a much higher response to methane than the nanofiber sensor, with a 157% difference in response rate. This is thought to be due partially to the electronic transport of the graphene nanoscrolls in the PANI film. Due to the absorption of the methane gas on the surface of the PANI film, expansion of the crystal structure within the polymer can occur which in turn changes the conduction path. The nanofiber/GNS sensor shows 106.4% difference in signal from the GNS sensor at 120 ppm of methane and a 121.5% difference from nanofibers alone. Additionally, the polyaniline only sensor showed a response of 0.01644% at 96 ppm, which is a difference of 104.4% from the nanofiber sensor, a difference of 115% from the GNS sensor and a difference of 173% for the nanofiber/GNS sensor. It is hypothesized that the graphene nanoscrolls have a synergistic effect with the nickel ferrite nanofibers allowing for higher conduction than polyaniline alone allowing for a more exaggerated change from the reduction of the nanofibers and surface molecules of polyaniline.

After testing with methane, acetone vapor was tested. Acetone vapor was formed by using 0.05ml, 0.1 ml, and 0.15 ml of acetone and heating it in a sealed container at 100 °C for 5 minutes. After heating the vapor was injected into the test chamber for analysis. Resistance changes were taken for the nanofiber sensor in **Figure 5-12**, the graphene nanoscrolls sensor in **Figure 5-13** and the nanofiber plus graphene nanoscroll sensor in **Figure 5-14**.

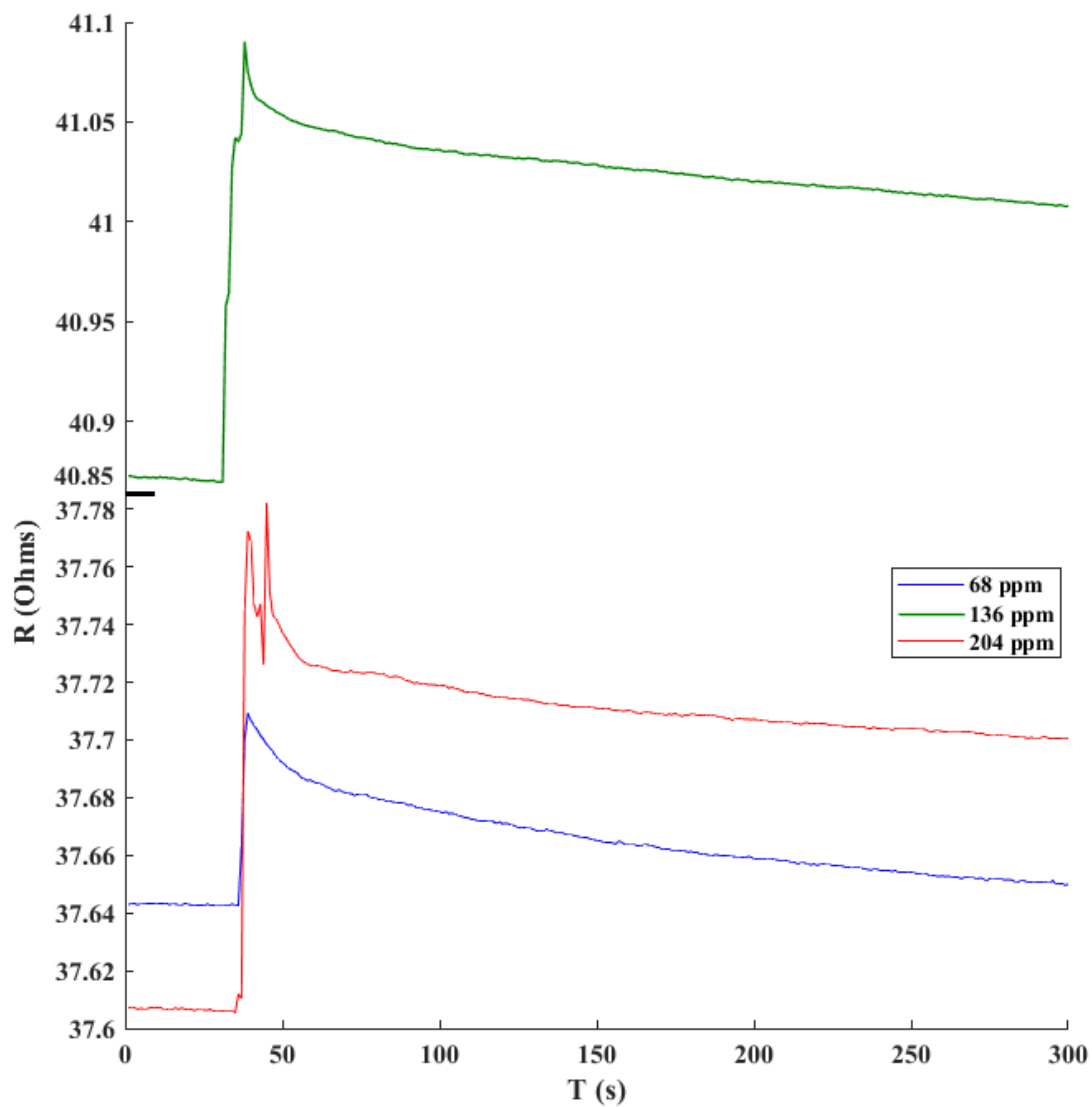


Figure 5-12: Response for acetone on nanofiber in PANI sensor.

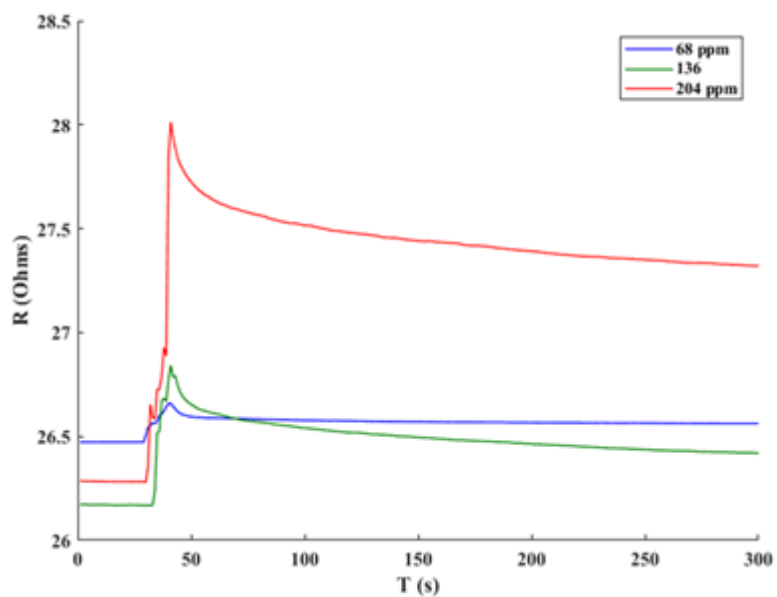


Figure 5-13: Response for acetone on GNS in PANI sensor.

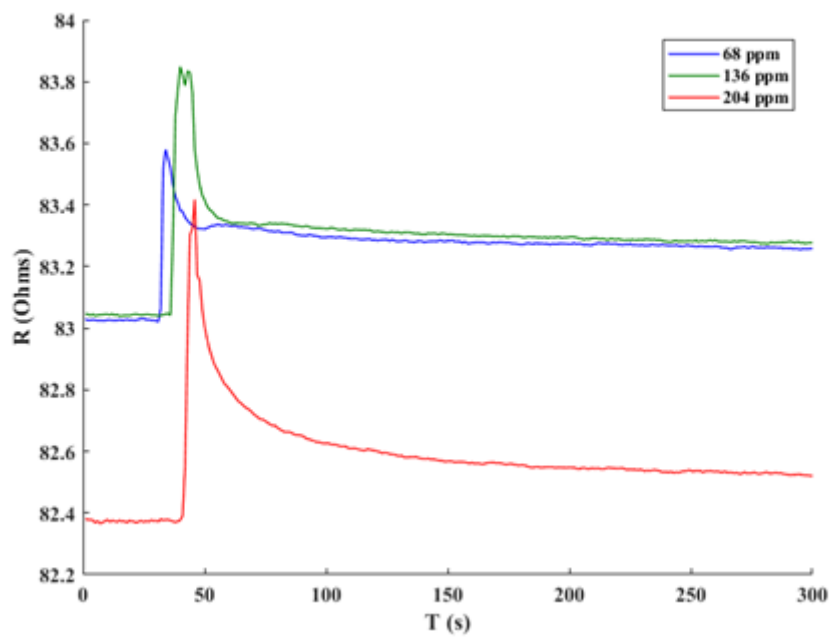


Figure 5-14: Response for acetone on nanofiber and GNS in PANI sensor.

Here, nanofibers have noticeably lower responses than graphene nanoscrolls with a 120% difference in response between the nanofibers and the graphene nanoscrolls while the nanofiber/gns response fell in between the two sensors, with only a 5.2% lower sensitivity than the graphene nanoscroll sensor for 68 ppm. At higher ppm, the difference is much greater with 173.48% difference between the graphene nanoscroll sensor and the nanofiber sensor. The polyaniline only sensor showed a response of 0.332 at 136 ppm of acetone which is only 23.87% lower than the nanofiber sensor but 154.3% lower than the GNS sensor and 103.5% lower than the nanofiber/GNS sensor. The nanofiber sensors showed a low reaction for acetone, due to the fact that ketones are a very poor reducing agent. This is because, in terms of carbonyl reduction, ketones do not have direct hydrogen bonds to their carbonyl group and have lower steric effects than other organics. The sensitivity for each sensor at the tested ppm of acetone is displayed in **Table 5-3**.

Table 5-3: Calculated sensitivity for acetone.

Vapor Amount	Nanofiber Sensor	GNS Sensor	Nanofiber/GNS Sensor
68 ppm	0.177	0.709	0.673
136 ppm	0.422	2.574	1.045
204 ppm	0.468	6.593	1.269

After testing methane and acetone, ethanol vapors were tested. Ethanol vapor was formed by using 0.05 ml, 0.1 ml, and 1.5 ml of ethanol and heating it in a closed container at 100 °C for 5 minutes. After heating the vapor was injected into the test chamber for analysis. Resistant measurements for ethanol vapors are shown for nanofibers in **Figure 5-**

15, the graphene nanoscroll sensor in **Figure 5-16**, and the nanofiber plus graphene nanoscroll sensor in **Figure 5-17**. **Table 5-4** shows the calculated sensitivities of ethanol.

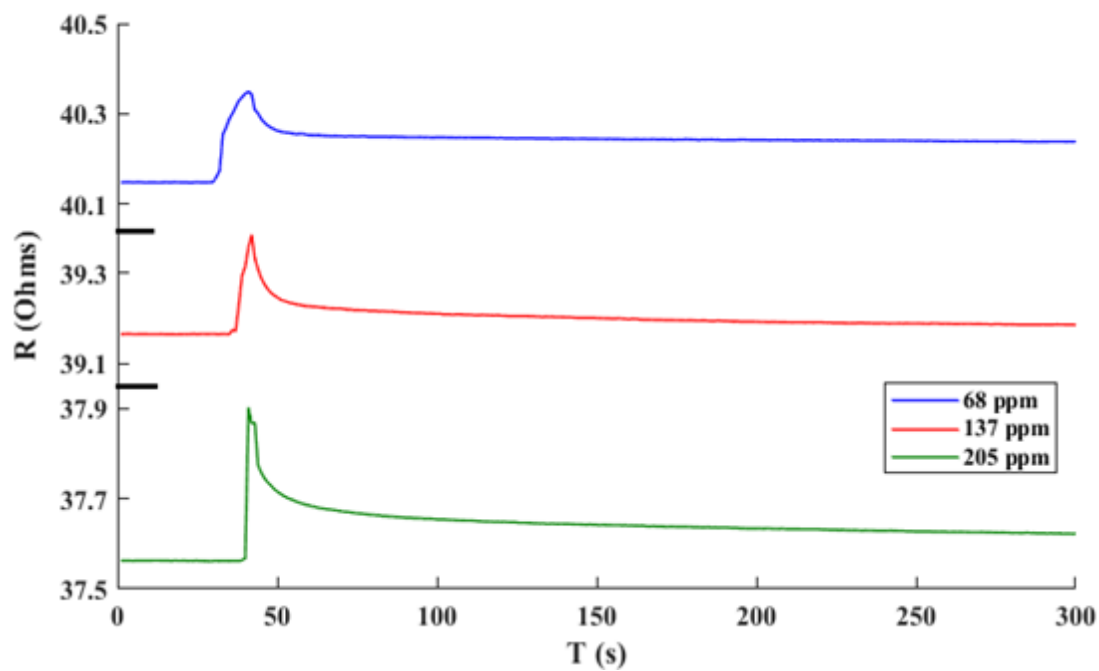


Figure 5-15: Response for ethanol on nanofiber sensor.

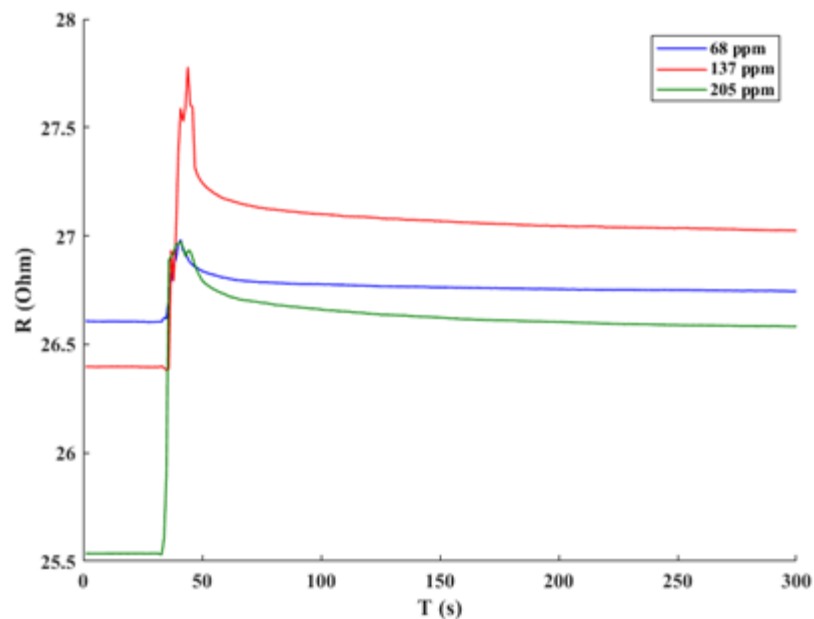


Figure 5-16: Response for ethanol on GNS sensor.

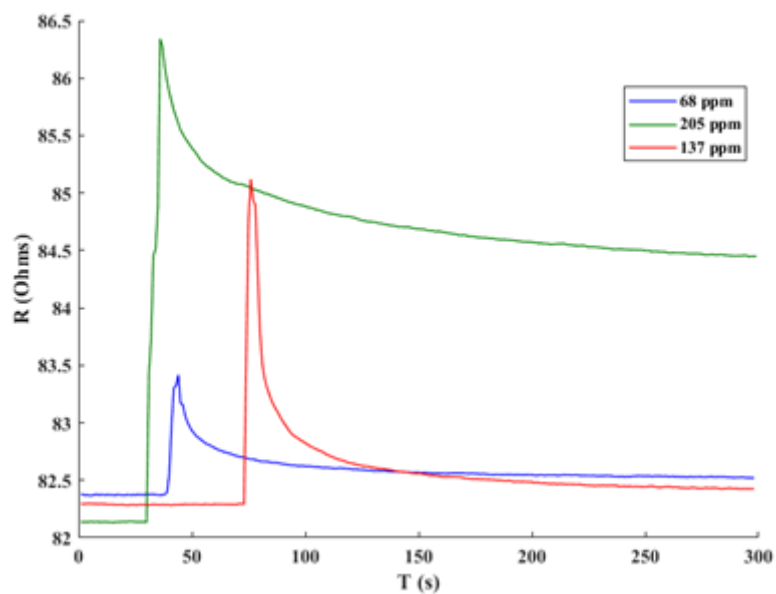


Figure 5-17: Response for ethanol on nanofiber/GNS sensor as resistance change.

Table 5-4: Calculated sensitivities for ethanol.

Vapor Amount	Nanofiber Sensor	GNS Sensor	Nanofiber/GNS Sensor
68 ppm	0.501	1.425	1.269
137 ppm	0.564	4.521	3.443
205 ppm	0.905	5.656	5.04

The nanofiber/GNS sensor shows a lower response than the nanofiber only sensor by 29.3% difference between the responses at 137 ppm injected. At the end of the 300 second testing period, the nanofiber/GNS sensor had lowered to a 2.79% difference from its starting resistance. This shows chemisorption on the polyaniline which leads to an expansion of the polymer, causing an increased resistance. The polyaniline only sensor showed a sensitivity of 0.249 at 137 ppm of ethanol, a difference of 77.5% lower than the nanofiber doped polyaniline sensor, 179.1% lower than the graphene nanoscroll doped polyaniline sensor, and 173% lower than the combination nanofiber/graphene nanoscroll sensor. This indicates the addition of nanoparticles to the polyaniline greatly enhances performance due to the surface area and enhance conduction of the graphene nanoscrolls and oxidation states of the heterogeneous metal nanofiber. **Figure 5-18** shows the sensitivities vs the various concentrations of methane, **Figure 5-19** shows the sensitivities at the various concentrations of acetone and **Figure 5-20** shows the sensitivities at the concentrations of ethanol.

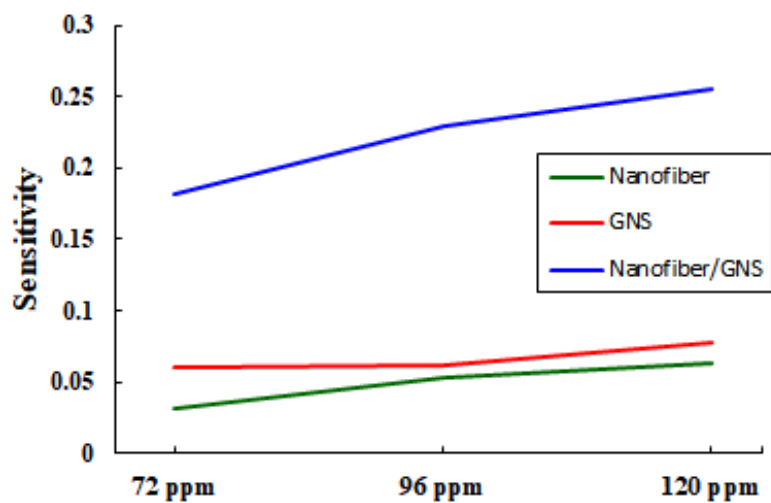


Figure 5-18: Sensitivities of the sensors at different methane concentrations.

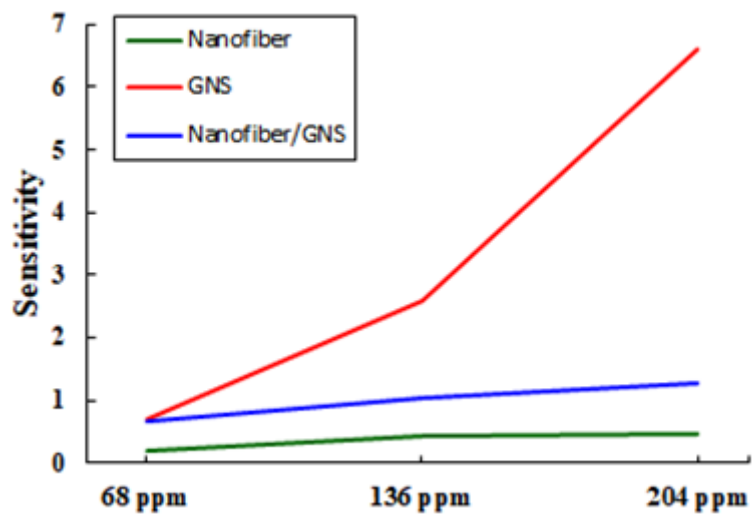


Figure 5-19: Sensitivities of sensors at different concentrations of acetone.

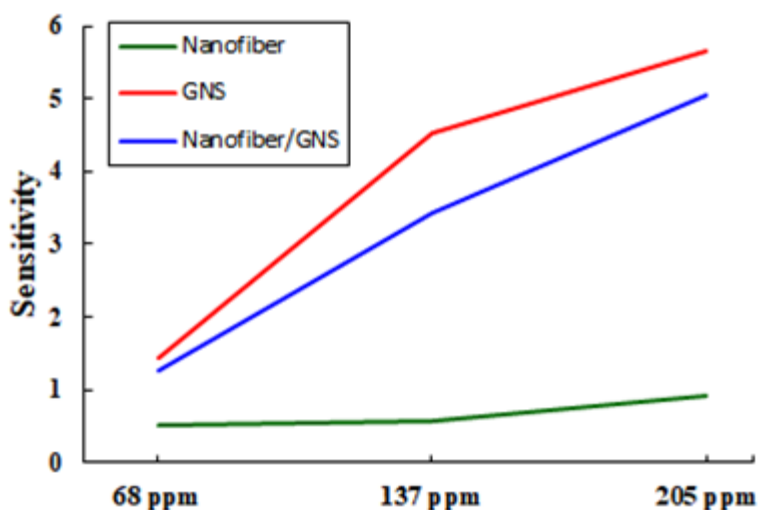


Figure 5-20: Sensitivities of sensors at different concentrations of ethanol.

As shown, both nickel ferrite nanofibers and graphene nanoscrolls in a polyaniline medium can greatly enhance the gas response to methane, ethanol, and acetone. The addition of GNS into the sensor formed the main increase to the sensitivity for the nonreducing gases acetone and ethanol, while the nickel ferrite nanofiber's addition to the sensors formed the largest increase in sensitivities for the reducing gas, methane. This indicates different modes of response present in the polyaniline doped sensors, with the first mode described as the change in oxidation states of the nanofibers and polyaniline itself, with publications pointing to several different oxidation states in ferrite particles being one of the properties that ferrite-containing sensors are so sensitive to oxidizing and reducing gases [174]. The second mode is described as an expansion of bonding lengths due to chemisorption which causes a change in electrical conductivity that is enhanced by the GNS [175]. This shows that multiple dopants can be used in a polyaniline medium to enhance different sensing modes and create a passive gas sensor

that is tuned for specific sets of reducing and nonreducing gases and can detect differences in gas amounts at the ppm level.

5.5 Summary

Both graphene nanoscrolls and nanofibers offer potential use in a variety of different applications. Gas sensors were chosen due to the high surface area and conductive nature of these two nanomaterials. In order to determine how gas would interact with the surface of a nanofiber, porosity calculations were done on the nanofibers. Nanofibers were found to have a 75.4% size difference between modeled structure and the experimentally determined diameter indicating the presence of a high amount of mesopores within the structure.

To create gas sensors, polyaniline was used as a conductive polymer base and was doped by nanofibers and graphene nanoscrolls. These solutions were then drop-cast onto gold on chrome interdigital MEMs arrays that were fabricated using photolithographic techniques. The sensors were tested using a digital multimeter to record resistance under methane, acetone, and ethanol vapors at 3 concentrations. These readings were analyzed, and sensitivities were determined experimentally for the three different chemicals. This research shows the versatility of nanofibers and graphene nanoscrolls as nanomaterials that have high sensitivity to organics and can sense at room temperature. This shows the inclusion of nanofibers and graphene nanoscrolls offer different avenues to cover multiple organics and have tailor-made responses to each.

CHAPTER 6

CONCLUSIONS AND FUTURE WORK

6.1 Conclusions

Steam methane reforming is currently the chief method of hydrogen production and carbon dioxide emissions that are measured at over 18 million tons annually. The hydrogen industry is valued at roughly 150 billion dollars annually. Mitigation of carbon dioxide and other greenhouse gas emissions has been a focus of the chemical processing industry as it moves to meet carbon emission standards. Dry reforming offers the possibility of eliminating carbon dioxide emissions from steam reforming but is not used due to a higher required energy and solid carbon formation that deactivates the catalytic material used in dry reforming. The research in this dissertation demonstrates a clear pathway toward the creation of high activity, low apparent activation energy nanostructured catalysts that are highly coke resistant for use in the dry reforming reaction, and the use of these nanomaterials in the creation of passive MEMs sensors for local analysis of gases in a reaction system.

To show this, the research in this dissertation focused on the use of ceramic nanofibers and the use of graphene nanoscrolls as supports for nanoparticle nickel catalysts and heterogeneous nickel ferrite catalysts. These nanofibers were made using a process known as electrospinning which was chosen for its ability to create consistent, high aspect

ratio nanofibers that can contain a variety of metals, nonmetals and semimetals materials. The use of these nanofibers was shown to lower the apparent activation energy of the conversion of methane (the rate-limiting step of dry reforming) while also lowering the conversion of carbon dioxide. In particular, the magnesium aluminate catalyst showed an apparent activation energy that was 91% lower than traditionally made nickel catalyst using a wetness impregnation method for the methane conversion, while remaining consistently active during the entire 15-hour testing period, primarily through tendency of the coking on the surface to form polymeric and amorphous films that did not deactivate the active sites on the catalyst. This is due to the magnesium aluminate spine's high stability and reported ability to utilize solid carbon in the dry reforming reaction [85]. The graphene nanoscroll-supported catalysts were excellent at resisting coking on the surface of the catalyst, forming 10 at% less carbon on the surface than traditional nickel catalysts.

In Chapters 2 and 3, the current state of the methane reforming industry was explored, the reaction kinetics of the dry reforming reaction, its side reactions, and coking mechanisms were detailed as well as the current state of the art in dry reforming, followed by the experimentation of homogeneous and heterogeneous nickel-based nanofiber catalysts made through the electrospinning process. These were tested in a plug flow reactor at 3 different temperatures to determine reaction rates, surface coking, and apparent activation energies. The apparent activation energies were found to be within literature values for the standard nickel catalyst, and the nickel ferrite 2:1 wt% apparent activation energy was 86.5% higher than the NiFe 1:1 wt%, which, while close to the calculated in literature suggests that it required higher temperatures to reach similar conversions as its 1:1 wt% counterpart. Magnesium aluminate spinels were shown to be excellent supports

in nanofiber form, with an extremely high stability and a very low calculated activation energy, at 0.66 kJ/mol. It was determined that due to the low apparent activation energies of the magnesium aluminate supported nickel catalyst, it was the best catalyst for lowering required energy in the dry reforming reaction.

In Chapter 4, graphene and graphene-based nanoscrolls were explored. The graphene nanoplatelets were made through an inexpensive electrochemical exfoliation process. They were then tested under XRD and Raman spectroscopy to determine their layered properties. Additionally, the graphene sheets were then used to make the graphene nanoscrolls using heat and ultrasonication. These nanoscrolls were studied under TEM and Raman to determine their properties. The use of graphene nanoscrolls as novel supports for nickel-based dry reforming was also studied. Due to graphene's unique electronic structure, the graphene nanoscrolls based support offered a strong support of the catalytic material. The results of this test show that loading of graphene nanoscrolls offer a viable path forward towards coke resistant dry reforming catalysts, producing less visible whiskers and having lower activation energy than the nickel ferrite 2:1 catalyst and a lower coke deposition than the nickel ferrite 1:1 catalyst, making it best catalyst for resisting carbon deposition. Additional testing with noble metal catalysts inside of graphene nanoscrolls would be a productive continuation of this research, and additional testing on how much the deposited carbon on the surfaces of the nickel ferrite and magnesium aluminate nanofiber catalysts influence the dry reforming reaction would help validate the claims of deposited carbon taking an active role in the dry reforming reaction on the surfaces of these catalysts.

In Chapter 5, the use of nanofibers made through electrospinning and graphene nanoscrolls made through electrochemical exfoliation and ultrasonication as a basis for gas sensors was explored. These gas sensors offer the ability to sense minute amounts of gas at room temperature. These sensors were made using a MEMs photolithography method with the sensing material drop cast onto the surface of the MEMs interdigital array. The sensors were tested under 3 different concentrations of methane, ethanol vapors and acetone vapors. It was shown that the addition of 0.8 mg of nanofibers and 0.5 mg of graphene nanoscrolls with 3 ml of polyaniline enhanced the gas and vapor sensitivities by over 173% for ethanol. This shows that heterogenous metal nanofibers and graphene nanoscrolls offer viable paths forward toward tuning response for passive gas sensing.

Taken together, the research in this dissertation has shown that nanofibers via the electrospinning method offer a viable nanostructuring synthesis method for the creation of highly stable mesoporous meshes for the use in dry reforming. Due to their flexibility in loading for the nanofiber, the catalysts can be tuned precisely and for different product ratios and support materials. The magnesium aluminate ceramic nanofibers showed a long life and a high conversion percentage, owing to their low activation energy required for the dry reforming reaction. Additionally, graphene nanoscrolls were shown to be a nanostructured support for the loading of nickel catalyst that was highly resistant to deactivation due to coking. Graphene nanoscrolls offer the prospect of using a cheap bulk electrochemical process to produce highly coke resistant supports for using in dry reforming. Gas sensors fabricated using the nanomaterials synthesized in this research also showed tunable responses to a variety of organic gases including methane, one of the most difficult gases to detect using a chemoreceptive sensor. The sensors were shown to be able

to detect small amounts of these gases passively at room temperature, allowing them to be included in any low energy system to detect a variety of potentially useful organic compounds. Additionally, the mixture of the nanofiber and graphene nanoscroll sensor proved to be the most flexible of the sensors, with responses to all the gases tested due to the different reaction modes in the sensor. This offers the exciting possibility of future research where graphene nanoscrolls could potentially be used in the electrospinning process to be directly incorporated into nanofibers, imparting their coke resistance to the lower activation energies associated with the nanofibers.

6.2 Future Work

Apart from future publications, several research avenues present themselves in the immediate aftermath of this dissertation. An exploration into the role that deposited carbon on the surface of the magnesium aluminate catalyst plays in the dry reforming reaction would help to explore why the catalyst remained consistently active despite having built up coke over the testing period. The use of more exotic metals such as ruthenium or platinum as the active metal catalyst would be useful for extending the catalysts lifetime and the extremely high surface area of the nanofibers allows for less of the material to be used in the production of the catalyst, lowering the overall cost of using such catalysts in industry. Additionally, testing the reaction in plasma environments offer the opportunity to create an environment that is ideal for dry reforming, and utilize the catalyst in a synergistic effect with the plasma while eliminating coking effects. The results of this dissertation show that hydrogen formation using dry reforming of methane offers a valuable avenue of

continued research with the advancement of nanoscience allowing for a unique space for the continuation of this research.

REFERENCES

- [1] "Syngas composition". National Energy Technology Laboratory, U.S. Department of Energy. <https://www.netl.doe.gov/research/coal/energy-systems/gasification/gasifipedia/syngas-composition>
- [2] Lavoie, J. M. "Review on dry reforming of methane, a potentially more environmentally-friendly approach to the increasing natural gas exploitation." *Frontiers in Chemistry* 2 (2014): 81.
- [3] Jain, I. P. "Hydrogen the fuel for 21st century." *International journal of hydrogen energy* 34, no. 17 (2009): 7368-7378.
- [4] Galloway, J. N., and E. B. Cowling. "Reactive nitrogen and the world: 200 years of change." *AMBIO: A Journal of the Human Environment* 31, no. 2 (2002): 64-71.
- [5] Rostrup-Nielsen, J. R. "Production of synthesis gas." *Catalysis today* 18, no. 4 (1993): 305-324.
- [6] Leckel, D. "Diesel production from Fischer–Tropsch: the past, the present, and new concepts." *Energy & Fuels* 23, no. 5 (2009): 2342-2358.
- [7] Rostrup-Nielsen, J. R. "Catalytic steam reforming." In *Catalysis*, pp. 1-117. Springer, Berlin, Heidelberg, 1984.
- [8] Ashcroft, A. T., A. K. Cheetham, and M. L. H. Green. "Partial oxidation of methane to synthesis gas using carbon dioxide." *Nature* 352, no. 6332 (1991): 225-226.
- [9] Gangadharan, P., K. C. Kanchi, and H. H. Lou. "Evaluation of the economic and environmental impact of combining dry reforming with steam reforming of methane." *Chemical Engineering Research and Design* 90, no. 11 (2012): 1956-1968.
- [10] Wang, S., G. Q. Lu, and G. J. Millar. "Carbon dioxide reforming of methane to produce synthesis gas over metal-supported catalysts: state of the art." *Energy & fuels* 10, no. 4 (1996): 896-904.
- [11] Houghton, J. T., J. G. Ding, D. J. Griggs, M. N. Paul, J. van der Linden, X. Dai, K. Maskell, and C. A. Johnson. "Climate change 2001: the scientific basis." The Press Syndicate of the University of Cambridge, 2001.

- [12] US Energy Information Administration, Ed. Annual Energy Outlook 2011: With Projections to 2035. Government Printing Office, 2011.
- [13] EIA, US. "Energy Information Administration: Annual Energy Outlook 2018 with projections to 2050." US Energy Information Administration, Office of Integrated and International Energy Analysis, US Department of Energy, Washington, DC 20585 (2018).
- [14] Intergovernmental Panel on Climate Change. Climate Change 2014—Impacts, Adaptation and Vulnerability: Regional Aspects. Cambridge University Press, 2014.
- [15] Courson, C., L. Udron, D. Świerczyński, C. Petit, and A. Kiennemann. "Hydrogen production from biomass gasification on nickel catalysts: tests for dry reforming of methane." *Catalysis Today* 76, no. 1 (2002): 75-86.
- [16] Richardson, J. T., and S. A. Paripatyadar. "Carbon dioxide reforming of methane with supported rhodium." *Applied Catalysis* 61, no. 1 (1990): 293-309.
- [17] Greene, D., J. Hopson, and J. Li. "Running out of and into oil: analyzing global oil depletion and transition through 2050." *Transportation Research Record: Journal of the Transportation Research Board* 1880 (2004): 1-9.
- [18] San-José-Alonso, D., J. Juan-Juan, M. J. Illán-Gómez, and M. C. Román-Martínez. "Ni, Co and bimetallic Ni–Co catalysts for the dry reforming of methane." *Applied Catalysis A: General* 371, no. 1-2 (2009): 54-59.
- [19] Bharadwaj, S. S., and L. D. Schmidt. "Catalytic partial oxidation of natural gas to syngas." *Fuel processing technology* 42, no. 2-3 (1995): 109-127.
- [20] Aasberg-Petersen, K., T. S. Christensen, C. S. Nielsen, and I. Dybkjær. "Recent developments in autothermal reforming and pre-reforming for synthesis gas production in GTL applications." *Fuel Processing Technology* 83, no. 1-3 (2003): 253-261.
- [21] Wei, J.M., and E. Iglesia, "Isotopic and kinetic assessment of the mechanism of methane reforming and decomposition reactions on supported iridium catalysts." *Physical Chemistry Chemical Physics*, 6 (2004) 3754-3759.
- [22] Wei, J.M., and E. Iglesia, "Isotopic and kinetic assessment of the mechanism of reactions of CH₄ with CO₂ or H₂O to form synthesis gas and carbon on nickel catalysts." *Journal of Catalysis*, 224 (2004) 370-383.
- [23] Wei, J.M., and E. Iglesia, "Structural requirements and reaction pathways in methane activation and chemical conversion catalyzed by rhodium, *Journal of Catalysis*." 225 (2004) 116-127.
- [24] Chen, D., R. Lødeng, A. Anundskås, O. Olsvik, and A. Holmen. "Deactivation during carbon dioxide reforming of methane over Ni catalyst: microkinetic analysis." *Chemical Engineering Science* 56, no. 4 (2001): 1371-1379.

- [25] Nandini, A., K. K. Pant, and S. C. Dhingra. "Kinetic study of the catalytic carbon dioxide reforming of methane to synthesis gas over Ni-K/CeO₂-Al₂O₃ catalyst." *Applied Catalysis A: General* 308 (2006): 119-127.
- [26] Wei, J.M, and E. Iglesia. "Structural requirements and activation pathways in reactions of methane catalyzed by supported metals." In *Abstracts of Papers of the American Chemical Society*, vol. 227, pp. U1072-U1072. Amer Chem Soc, 2004.
- [27] Maestri, M., D. G. Vlachos, A. Beretta, G. Groppi, and E. Tronconi. "A C1 microkinetic model for methane conversion to syngas on Rh/Al₂O₃." *AIChE Journal* 55, no. 4 (2009): 993-1008.
- [28] Erdöhelyi, A., J. Cserényi, E. Papp, and F. Solymosi. "Catalytic reaction of methane with carbon dioxide over supported palladium." *Applied Catalysis A: General* 108, no. 2 (1994): 205-219.
- [29] Wang, S.G., Y. W. Li, J. X. Lu, M.Y. He, and H. Jiao. "A detailed mechanism of thermal CO₂ reforming of CH₄." *Journal of Molecular Structure: THEOCHEM* 673, no. 1-3 (2004): 181-189.
- [30] Ginsburg, J. M., J. Piña, T. E. Solh, and H. I. De Lasa. "Coke formation over a nickel catalyst under methane dry reforming conditions: thermodynamic and kinetic models." *Industrial & engineering chemistry research* 44, no. 14 (2005): 4846-4854.
- [31] Cui, Y., H. Zhang, H. Xu, and W. Li. "Kinetic study of the catalytic reforming of CH₄ with CO₂ to syngas over Ni/ α -Al₂O₃ catalyst: the effect of temperature on the reforming mechanism." *Applied Catalysis A: General* 318 (2007): 79-88.
- [32] Abreu, C. A. M., D. A. Santos, J. A. Pacífico, and N. M. L. Filho. "Kinetic evaluation of Methane– Carbon dioxide reforming process based on the reaction steps." *Industrial & Engineering Chemistry Research* 47, no. 14 (2008): 4617-4622.
- [33] Solymosi, F., G. Kutsan, and A. Erdöhelyi. "Catalytic reaction of CH₄ with CO₂ over alumina-supported Pt metals." *Catalysis Letters* 11, no. 2 (1991): 149-156.
- [34] Sakai, Y., H. Saito, T. Sodesawa, and F. Nozaki. "Catalytic reactions of hydrocarbon with carbon dioxide over metallic catalysts." *Reaction Kinetics and Catalysis Letters* 24, no. 3-4 (1984): 253-257.
- [35] Tokunaga, O., and S. Ogasawara. "Reduction of carbon dioxide with methane over Ni-catalyst." *Reaction Kinetics and Catalysis Letters* 39, no. 1 (1989): 69-74.
- [36] Richardson, J. T., and S. A. Paripatyadar. "Carbon dioxide reforming of methane with supported rhodium." *Applied Catalysis* 61, no. 1 (1990): 293-309.
- [37] Qin, D., and J. Lapszewicz. "Study of mixed steam and CO₂ reforming of CH₄ to syngas on MgO-supported metals." *Catalysis Today* 21, no. 2-3 (1994): 551-560.

- [38] Knözinger, H., and P. Ratnasamy. "Catalytic aluminas: surface models and characterization of surface sites." *Catalysis Reviews Science and Engineering* 17, no. 1 (1978): 31-70.
- [39] Year, C. G. N., "Bayer's process for alumina production: a historical perspective." *Bull. Hist. Chem* 17, no. 18 (1995): 15.
- [40] Verhaak, M. J. F. M., A. J. Van Dillen, and J. W. Geus. "Measuring the acid-base properties of supported nickel catalysts using temperature-programmed desorption of ammonia." *Applied Catalysis A: General* 105, no. 2 (1993): 251-269.
- [41] Al-Ubaid, A., and E. E. Wolf. "Activity, FTIR studies and catalyst characterization during methane steam reforming on Ni/Y-zeolite catalysts." *Applied catalysis* 34 (1987): 119-134.
- [42] Kim, G. J., D. S. Cho, K. H. Kim, and J. H. Kim. "The reaction of CO₂ with CH₄ to synthesize H₂ and CO over nickel-loaded Y-zeolites." *Catalysis letters* 28, no. 1 (1994): 41-52.
- [43] Nakamura, J. "Methane reforming with carbon dioxide." *Syokubai (Catalysts)* 35 (1993): 478-484
- [44] Takayasu, O., E. Hirose, N. Matsuda, and I. Matsuura. "Partial oxidation of methane by metal catalysts supported on ultrafine single-crystal magnesium oxide." *Chem Express* 6 (1991): 447-450.
- [45] Nakamura, J., K. Aikawa, K. Sato, and T. Uchijima. "Role of support in reforming of CH₄ with CO₂ over Rh catalysts." *Catalysis letters* 25, no. 3-4 (1994): 265-270.'
- [46] Perera, J. S. H. Q., J. W. Couves, G. Sankar, and J. M. Thomas. "The catalytic activity of Ru and Ir supported on Eu₂O₃ for the reaction, CO₂ + CH₄ ⇌ 2 H₂ + 2 CO: a viable solar-thermal energy system." *Catalysis letters* 11, no. 2 (1991): 219-225.
- [47] Guerrero-Ruiz, A., I. Rodriguez-Ramos, and A. Sepúlveda-Escribano. "Effect of the basic function in Co, MgO/C catalysts on the selective oxidation of methane by carbon dioxide." *Journal of the Chemical Society, Chemical Communications* 5 (1993): 487-488.
- [48] Fujimoto, K., K. Omata, T. Nozaki, O. Yamazaki, and Y. Han. "Selective synthesis of liquid hydrocarbons from carbon dioxide and methane." *Energy Conversion and Management* 33, no. 5-8 (1992): 529-536.
- [49] Gadalla, A. M., and B. Bower. "The role of catalyst support on the activity of nickel for reforming methane with CO₂." *Chemical Engineering Science* 43, no. 11 (1988): 3049-3062.
- [50] Gaddalla, A. M., and M. E. Sommer. "Carbon dioxide reforming of methane on nickel catalysts." *Chemical Engineering Science* 44, no. 12 (1989): 2825-2829.

- [51] Ananikov, V. P. "Nickel: the "spirited horse" of transition metal catalysis." (2015): 1964-1971.
- [52] Dahal, A., and M. Batzill. "Graphene–nickel interfaces: a review." *Nanoscale* 6, no. 5 (2014): 2548-2562.
- [53] Rostrup-Nielsen, J. R. "Equilibria of decomposition reactions of carbon monoxide and methane over nickel catalysts." *Journal of Catalysis* 27, no. 3 (1972): 343-356.
- [54] de Sousa, F. F., H. S. de Sousa, A. C. Oliveira, M. C. C. Junior, A. P. Ayala, E. B. Barros, B. C. Viana, M. J. Filho, and A. C. Oliveira. "Nanostructured Ni-containing spinel oxides for the dry reforming of methane: effect of the presence of cobalt and nickel on the deactivation behaviour of catalysts." *international journal of hydrogen energy* 37, no. 4 (2012): 3201-3212.
- [55] Takenaka, S., S. Kobayashi, H. Ogihara, and K. Otsuka. "Ni/SiO₂ catalyst effective for methane decomposition into hydrogen and carbon nanofiber." *Journal of catalysis* 217, no. 1 (2003): 79-87.
- [56] Newnham, J., K. Mantri, M. H. Amin, J. Tardio, and S. K. Bhargava. "Highly stable and active Ni-mesoporous alumina catalysts for dry reforming of methane." *international journal of hydrogen energy* 37, no. 2 (2012): 1454-1464.
- [57] Kim, Y., C. Kim, P. Kim, and J. Yi. "Effect of preparation conditions on the phase transformation of mesoporous alumina." *Journal of non-crystalline solids* 351, no. 6-7 (2005): 550-556.
- [58] Mette, K., S. Kühn, H. Düdder, K. Kähler, A. Tarasov, M. Muhler, and M. Behrens. "Stable performance of Ni catalysts in the dry reforming of methane at high temperatures for the efficient conversion of CO₂ into syngas." *ChemCatChem* 6, no. 1 (2014): 100-104.
- [59] González, A. R., Y. J.O. Asencios, E. M. Assaf, and J. M. Assaf. "Dry reforming of methane on Ni–Mg–Al nano-spheroid oxide catalysts prepared by the sol–gel method from hydrotalcite-like precursors." *Applied Surface Science* 280 (2013): 876-887.
- [60] Zhang, Z., J. Li, W. Gao, Y. Ma, and Y. Qu. "Pt/porous nanorods of ceria as efficient high temperature catalysts with remarkable catalytic stability for carbon dioxide reforming of methane." *Journal of Materials Chemistry A* 3, no. 35 (2015): 18074-18082.
- [61] Khavarian, M., S. P. Chai, and A. R. Mohamed. "Direct use of as-synthesized multi-walled carbon nanotubes for carbon dioxide reforming of methane for producing synthesis gas." *Chemical Engineering Journal* 257 (2014): 200-208.
- [62] Dong, D., X. Shao, Z. Wang, C. Lievens, J. Yao, H. Wang, and C. Z. Li. "Fibrous NiO/CeO₂ nanocatalysts for the partial oxidation of methane at microsecond contact times." *RSC Advances* 3, no. 5 (2013): 1341-1345.

- [63] Wen, S., M. Liang, J. Zou, S. Wang, X. Zhu, L. Liu, and Z. J. Wang. "Synthesis of a SiO₂ nanofibre confined Ni catalyst by electrospinning for the CO₂ reforming of methane." *Journal of Materials Chemistry A* 3, no. 25 (2015): 13299-13307.
- [64] Barakat, N. AM, B. Kim, and H. Y. Kim. "Production of smooth and pure nickel metal nanofibers by the electrospinning technique: nanofibers possess splendid magnetic properties." *The Journal of Physical Chemistry C* 113, no. 2 (2008): 531-536.
- [65] Frusteri, F., L. Spadaro, F. Arena, and A. T. E. M. Chuvilin. "TEM evidence for factors affecting the genesis of carbon species on bare and K-promoted Ni/MgO catalysts during the dry reforming of methane." *Carbon* 40, no. 7 (2002): 1063-1070.
- [66] Chen, D., K. O. Christensen, E. Ochoa-Fernández, Z. Yu, B. Tøtdal, N. Latorre, A. Monzón, and A. Holmen. "Synthesis of carbon nanofibers: effects of Ni crystal size during methane decomposition." *Journal of Catalysis* 229, no. 1 (2005): 82-96.
- [67] Rad, S. J. H., M. Haghighi, A. A. Eslami, F. Rahmani, and N. Rahemi. "Sol-gel vs. impregnation preparation of MgO and CeO₂ doped Ni/Al₂O₃ nanocatalysts used in dry reforming of methane: Effect of process conditions, synthesis method and support composition." *International Journal of Hydrogen Energy* 41, no. 11 (2016): 5335-5350.
- [68] Huang, Z. M., Y-Z. Zhang, M. Kotaki, and S. Ramakrishna. "A review on polymer nanofibers by electrospinning and their applications in nanocomposites." *Composites science and technology* 63, no. 15 (2003): 2223-2253.
- [69] Pham, Q. P., U. Sharma, and A. G. Mikos. "Electrospinning of polymeric nanofibers for tissue engineering applications: a review." *Tissue engineering* 12, no. 5 (2006): 1197-1211.
- [70] Ramakrishna, S., K. Fujihara, W.-E. Teo, T. Yong, Z. Ma, and R. Ramaseshan. "Electrospun nanofibers: solving global issues." *Materials today* 9, no. 3 (2006): 40-50.
- [71] Wu, H., L. Hu, M. W. Rowell, D. Kong, J. J. Cha, J. R. McDonough, J. Zhu, Y. Yang, M. D. McGehee, and Y. Cui. "Electrospun metal nanofiber webs as high-performance transparent electrode." *Nano letters* 10, no. 10 (2010): 4242-4248.
- [72] Kim, I.-D., A. Rothschild, B. H. Lee, D. Y. Kim, S. M. Jo, and H. L. Tuller. "Ultrasensitive chemiresistors based on electrospun TiO₂ nanofibers." *Nano letters* 6, no. 9 (2006): 2009-2013.
- [73] Fang, J., H. T. Niu, T. Lin, and X. G. Wang. "Applications of electrospun nanofibers." *Chinese science bulletin* 53, no. 15 (2008): 2265.
- [74] Zhang, L., A. Aboagye, A. Kelkar, C. Lai, and H. Fong. "A review: carbon nanofibers from electrospun polyacrylonitrile and their applications." *Journal of Materials Science* 49, no. 2 (2014): 463-480.

- [75] Persano, L., A. Camposeo, C. Tekmen, and D. Pisignano. "Industrial upscaling of electrospinning and applications of polymer nanofibers: a review." *Macromolecular Materials and Engineering* 298, no. 5 (2013): 504-520.
- [76] Burger, C., B. S. Hsiao, and B. Chu. "Nanofibrous materials and their applications." *Annu. Rev. Mater. Res.* 36 (2006): 333-368.
- [77] Taylor, G. "Disintegration of water drops in an electric field." *Proceedings of the Royal Society of London. Series A. Mathematical and Physical Sciences* 280, no. 1382 (1964): 383-397.
- [78] Taylor, G. "Electrically driven jets." *Proc. R. Soc. London, Ser. A* 313, no. 1515 (1969): 453-475.
- [79] Angamma, C. J., and S. H. Jayaram. "A theoretical understanding of the physical mechanisms of electrospinning." In *Proc. ESA Annual Meeting on Electrostatics*, pp. 14-16. 2011.
- [80] Subbiah, T., G. S. Bhat, R. W. Tock, S. Parameswaran, and S. S. Ramkumar. "Electrospinning of nanofibers." *Journal of Applied Polymer Science* 96, no. 2 (2005): 557-569.
- [81] Thompson, C. J., G. G. Chase, A. L. Yarin, and D. H. Reneker. "Effects of parameters on nanofiber diameter determined from electrospinning model." *Polymer* 48, no. 23 (2007): 6913-6922.
- [82] Bhattacharjee, P. K., T. M. Schneider, M. P. Brenner, G. H. McKinley, and G. C. Rutledge. "On the measured current in electrospinning." *Journal of Applied Physics* 107, no. 4 (2010): 044306.
- [83] Gibson, P., H. Schreuder-Gibson, and D. Rivin. "Transport properties of porous membranes based on electrospun nanofibers." *Colloids and Surfaces A: Physicochemical and Engineering Aspects* 187 (2001): 469-481.
- [84] Kim, S. M., P. M. Abdala, T. Margossian, D. Hosseini, L. Foppa, A. Armutlulu, W. van Beek, A. Comas-Vives, C. Copéret, and C. Müller. "Cooperativity and dynamics increase the performance of NiFe dry reforming catalysts." *Journal of the American Chemical Society* 139, no. 5 (2017): 1937-1949.
- [85] Guo, J., H. Lou, H. Zhao, D. Chai, and X. Zheng. "Dry reforming of methane over nickel catalysts supported on magnesium aluminate spinels." *Applied Catalysis A: General* 273, no. 1-2 (2004): 75-82.
- [86] Shishido, T., M. Sukenobu, H. Morioka, R. Furukawa, H. Shirahase, and K. Takehira. "CO₂ reforming of CH₄ over Ni/Mg–Al oxide catalysts prepared by solid phase crystallization method from Mg–Al hydrotalcite-like precursors." *Catalysis letters* 73, no. 1 (2001): 21-26.

- [87] Fan, M. S., A. Z. Abdullah, and S. Bhatia. "Utilization of Greenhouse Gases through Dry Reforming: Screening of Nickel-Based Bimetallic Catalysts and Kinetic Studies." *ChemSusChem* 4, no. 11 (2011): 1643-1653.
- [88] Allen, M. J., V. C. Tung, and R. B. Kaner. "Honeycomb carbon: a review of graphene." *Chemical reviews* 110, no. 1 (2009): 132-145.
- [89] Zhu, Y., S. Murali, W. Cai, X. Li, J. W. Suk, J. R. Potts, and R. S. Ruoff. "Graphene and graphene oxide: synthesis, properties, and applications." *Advanced materials* 22, no. 35 (2010): 3906-3924.
- [90] Choi, W., I. Lahiri, R. Seelaboyina, and Y. S. Kang. "Synthesis of graphene and its applications: a review." *Critical Reviews in Solid State and Materials Sciences* 35, no. 1 (2010): 52-71.
- [91] Soldano, C., A. Mahmood, and E. Dujardin. "Production, properties and potential of graphene." *Carbon* 48, no. 8 (2010): 2127-2150.
- [92] Zhang, Y. I., L. Zhang, and C. Zhou. "Review of chemical vapor deposition of graphene and related applications." *Accounts of chemical research* 46, no. 10 (2013): 2329-2339.
- [93] Huang, X., Z. Y., S. Wu, X. Qi, Q. He, Q. Zhang, Q. Yan, F. Boey, and H. Zhang. "Graphene-based materials: synthesis, characterization, properties, and applications." *small* 7, no. 14 (2011): 1876-1902.
- [94] Otsuji, T., S. A. B. Tombet, A. Satou, H. Fukidome, M. Suemitsu, E. Sano, V. Popov, M. Ryzhii, and V. Ryzhii. "Graphene-based devices in terahertz science and technology." *Journal of Physics D: Applied Physics* 45, no. 30 (2012): 303001.
- [95] Docherty, C. J., and M. B. Johnston. "Terahertz properties of graphene." *Journal of Infrared, Millimeter, and Terahertz Waves* 33, no. 8 (2012): 797-815.
- [96] Geim, A. K. "Graphene: status and prospects." *science* 324, no. 5934 (2009): 1530-1534.
- [97] Geim, A. K., and K. S. Novoselov. "The rise of graphene." *Nature materials* 6.3 (2007): 183-191.
- [98] Diaz-Pinto, C., D. De, V. G. Hadjiev, and H. Peng. "AB-stacked multilayer graphene synthesized via chemical vapor deposition: a characterization by hot carrier transport." *Acs Nano* 6, no. 2 (2012): 1142-1148.
- [99] Nakajima, T., and K. Shintani. "Molecular dynamics study of energetics of graphene flakes." *Journal of Applied Physics* 106, no. 11 (2009): 114305.
- [100] Rao, C. N. R., K. S. Subrahmanyam, H.S.S. R. Matte, B. Abdulkhakeem, A. Govindaraj, B. Das, P. Kumar, A. Ghosh, and D. J. Late. "A study of the synthetic methods and properties of graphenes." *Science and Technology of Advanced Materials* 11, no. 5 (2010): 054502.

- [101] Lui, C. H., L. Liu, K. F. Mak, G. W. Flynn, and T. F. Heinz. "Ultraflat graphene." *Nature* 462, no. 7271 (2009): 339.
- [102] Yang, L., M. L. Cohen, and S. G. Louie. "Magnetic edge-state excitons in zigzag graphene nanoribbons." *Physical review letters* 101, no. 18 (2008): 186401.
- [103] Lee, C., X. Wei, J. W. Kysar, and J. Hone. "Measurement of the elastic properties and intrinsic strength of monolayer graphene." *Science* 321, no. 5887 (2008): 385-388.
- [104] Stoller, M. D., S. Park, Y. Zhu, J. An, and R. S. Ruoff. "Graphene-based ultracapacitors." *Nano letters* 8, no. 10 (2008): 3498-3502.
- [105] Song, W., X. Ji, W. Deng, Q. Chen, C. Shen, and C. E. Banks. "Graphene ultracapacitors: structural impacts." *Physical Chemistry Chemical Physics* 15, no. 13 (2013): 4799-4803.
- [106] Falkovsky, L. A., and S. S. Pershoguba. "Optical far-infrared properties of a graphene monolayer and multilayer." *Physical Review B* 76, no. 15 (2007): 153410.
- [107] Novoselov, K. S., Z. Jiang, Y. Zhang, S. V. Morozov, H. L. Stormer, U. Zeitler, J. C. Maan, G. S. Boebinger, P. Kim, and A. K. Geim. "Room-temperature quantum Hall effect in graphene." *Science* 315, no. 5817 (2007): 1379-1379.
- [108] Nair, R. R., P. Blake, A. N. Grigorenko, K. S. Novoselov, T. J. Booth, T. Stauber, N. M. R. Peres, and A. K. Geim. "Fine structure constant defines visual transparency of graphene." *Science* 320, no. 5881 (2008): 1308-1308.
- [109] Son, Y.-W., M. L. Cohen, and S. G. Louie. "Half-metallic graphene nanoribbons." *Nature* 444, no. 7117 (2006): 347.
- [110] Gómez-Navarro, C., R. T. Weitz, A. M. Bittner, M. Scolari, A. Mews, M. Burghard, and K. Kern. "Electronic transport properties of individual chemically reduced graphene oxide sheets." *Nano letters* 7, no. 11 (2007): 3499-3503.
- [111] Rozhkov, A. V., S. Savel'ev, and F. Nori, "Electronic Properties of Armchair Graphene Nanoribbons" *Physical Review B*, 79 (2009): 125420.
- [112] Nakada, K., M. Fujita, G. Dresselhaus, and M.S. Dresselhaus, "Edge State in Graphene Ribbons: Nanometer Size Effect and Edge Shape Dependence," *Physical Review B*, 54 (1996): 17954-17959.
- [113] Banhart, F., J. Kotakoski, and A.V. Krasheninnikov, "Structural defects in graphene," *ACS Nano*, 5 (2011): 26-41.
- [114] Freitag, M., M. Steiner, Y. Martin, V. Perebeinos, Z. Chen, J.C. Tsang, and P. Avouris, "Energy dissipation in graphene field-effect transistors," *Nano Letters*, 9 (2009): 1883-1888.

- [115] Cooper, D. R., B. D'Anjou, N. Ghattamaneni, B. Harack, M. Hilke, A. Horth, N. Majlis, M. Massicotte, L. Vandsburger, E. Whiteway and V. Yu. "Experimental review of graphene." *ISRN Condensed Matter Physics* 2012 (2012).
- [116] Yi, M., and Z. Shen. "A review on mechanical exfoliation for the scalable production of graphene." *Journal of Materials Chemistry A*, 3(22) (2015): 11700-11715.
- [117] Hofmann, M., W.Y. Chiang, T. D. Nguyễn, and Y. P. Hsieh. "Controlling the properties of graphene produced by electrochemical exfoliation." *Nanotechnology* 26, no. 33 (2015): 335607.
- [118] Abdelkader, A. M., A. J. Cooper, R. A. W. Dryfe, and I. A. Kinloch. "How to get between the sheets: a review of recent works on the electrochemical exfoliation of graphene materials from bulk graphite." *Nanoscale* 7, no. 16 (2015): 6944-6956.
- [119] Clower, W., N. Groden, and C. G. Wilson. "Graphene nanoscrolls fabricated by ultrasonication of electrochemically exfoliated graphene." *Nano-Structures & Nano-Objects* 12 (2017): 77-83.
- [120] Mattevi, C., H. Kim and M. Chowalla, "A review of chemical vapor deposition of graphene on copper" *J. Mater. Chem.*, 21 (2011): 3324-3334.
- [121] Mpourmpakis, G., E. Tylianakis, and G. E. Froudakis. "Carbon nanoscrolls: a promising material for hydrogen storage." *Nano Letters* 7, no. 7 (2007): 1893-1897.
- [122] Braga, S. F., V. R. Coluci, S. B. Legoas, R. Giro, D. S. Galvão, and R. H. Baughman. "Structure and dynamics of carbon nanoscrolls." *Nano Letters* 4, no. 5 (2004): 881-884.
- [123] Shi, X., N. M. Pugno, and H. Gao. "Mechanics of carbon nanoscrolls: a review." *Acta Mechanica Solida Sinica* 23, no. 6 (2010): 484-497.
- [124] Rurali, R., V. R. Coluci, and D. S. Galvao. "Prediction of giant electroactuation for papyruslike carbon nanoscroll structures: first-principles calculations." *Physical Review B* 74, no. 8 (2006): 085414.
- [125] Hassanzadazar, M., M. T. Ahmadi, R. Ismail, and H. Goudarzi. "Electrical Property Analytical Prediction on Archimedes Chiral Carbon Nanoscrolls." *Journal of Electronic Materials* 45, no. 10 (2016): 5404-5411.
- [126] Coluci, V. R., S. F. Braga, R. H. Baughman, and D. S. Galvao. "Prediction of the hydrogen storage capacity of carbon nanoscrolls." *Physical Review B* 75, no. 12 (2007): 125404.
- [127] Braga, S. F., V. R. Coluci, R. H. Baughman, and D. S. Galvao. "Hydrogen storage in carbon nanoscrolls: An atomistic molecular dynamics study." *Chemical Physics Letters* 441, no. 1 (2007): 78-82.

- [128] Huang, Y., and T. Li. "Molecular mass transportation via carbon nanoscrolls." *Journal of Applied Mechanics* 80, no. 4 (2013): 040903.
- [129] Peigney, A., C. Laurent, E. Flahaut, R. R. Bacsa, and A. Rousset. "Specific surface area of carbon nanotubes and bundles of carbon nanotubes." *Carbon* 39, no. 4 (2001): 507-514.
- [130] Javey, A., J. Guo, Q. Wang, M. Lundstrom, and H. Dai. "Ballistic carbon nanotube field-effect transistors." *Nature* 424, no. 6949 (2003): 654-657.
- [131] Zhang, Z., and T. Li. "Ultrafast nano-oscillators based on interlayer-bridged carbon nanoscrolls." *Nanoscale Research Letters* 6, no. 1 (2011): 470.
- [132] Liu, Z., S. Tabakman, K. Welsher, and H. Dai. "Carbon nanotubes in biology and medicine: in vitro and in vivo detection, imaging and drug delivery." *Nano Research* 2, no. 2 (2009): 85-120.
- [133] Xie, X., L. Ju, X. Feng, Y. Sun, R. Zhou, K. Liu, S. Fan, Q. Li, and K. Jiang. "Controlled fabrication of high-quality carbon nanoscrolls from monolayer graphene." *Nano Letters* 9, no. 7 (2009): 2565-2570.
- [134] Carotenuto, G., A. Longo, S. De Nicola, C. Camerlingo, and L. Nicolais. "A simple mechanical technique to obtain carbon nanoscrolls from graphite nanoplatelets." *Nanoscale Research Letters* 8, no. 1 (2013): 403.
- [135] Zheng, J., H. Liu, B. Wu, Y. Guo, T. Wu, G. Yu, Y. Liu, and D. Zhu. "Production of High-Quality Carbon Nanoscrolls with Microwave Spark Assistance in Liquid Nitrogen." *Advanced Materials* 23, no. 21 (2011): 2460-2463.
- [136] Zhu, S., and T. Li. "Hydrogenation enabled scrolling of graphene." *Journal of Physics D: Applied Physics* 46, no. 7 (2013): 075301.
- [137] Xu, Z., B. Zheng, J. Chen, and C. Gao. "Highly efficient synthesis of neat graphene nanoscrolls from graphene oxide by well-controlled lyophilization." *Chemistry of Materials* 26, no. 23 (2014): 6811-6818.
- [138] Zeng, F., Y. Kuang, Y. Wang, Z. Huang, C. Fu, and H. Zhou. "Facile Preparation of High-Quality Graphene Scrolls from Graphite Oxide by a Microexplosion Method." *Advanced Materials* 23, no. 42 (2011): 4929-4932.
- [139] Sharifi, T., E. Gracia-Espino, H. R. Barzegar, X. Jia, F. Nitze, G. Hu, P. Nordblad, C. W. Tai, and T. Wågberg. "Formation of nitrogen-doped graphene nanoscrolls by adsorption of magnetic γ -Fe₂O₃ nanoparticles." *Nature Communications* 4 (2013).
- [140] Cheng, G., I. Calizo, X. Liang, B. A. Sperling, A. C. Johnston-Peck, W. Li, J. E. Maslar, C. A. Richter, and A. R. H. Walker. "Carbon scrolls from chemical vapor deposition grown graphene." *Carbon* 76 (2014): 257-265.

- [141] Chuvilin, A., U. Kaiser, E. Bichoutskaia, N. A. Besley, and A. N. Khlobystov. "Direct transformation of graphene to fullerene." *Nature Chemistry* 2, no. 6 (2010): 450-453.
- [142] Viculis, L. M., J. J. Mack, and R. B. Kaner. "A chemical route to carbon nanoscrolls." *Science* 299, no. 5611 (2003): 1361-1361.
- [143] Zhao, J., B. Yang, Z. Yang, P. Zhang, Z. Zheng, W. Ren, and X. Yan. "Facile preparation of large-scale graphene nanoscrolls from graphene oxide sheets by cold quenching in liquid nitrogen." *Carbon* 79 (2014): 470-477.
- [144] Schaper, A. K., M. S. Wang, Z. Xu, Y. Bando, and D. Golberg. "Comparative studies on the electrical and mechanical behavior of catalytically grown multiwalled carbon nanotubes and scrolled graphene." *Nano Letters* 11, no. 8 (2011): 3295-3300.
- [145] Savoskin, M. V., V. N. Mochalin, A. P. Yaroshenko, N. I. Lazareva, T. E. Konstantinova, I. V. Barsukov, and I. G. Prokofiev. "Carbon nanoscrolls produced from acceptor-type graphite intercalation compounds." *Carbon* 45, no. 14 (2007): 2797-2800.
- [146] Chen, X., L. Li, X. Sun, H. G. Kia, and H. Peng. "A novel synthesis of graphene nanoscrolls with tunable dimension at a large scale." *Nanotechnology* 23, no. 5 (2012): 055603.
- [147] Bondi, C. A., J. L. Marks, L. B. Wroblewski, H. S. Raatikainen, S. R. Lenox, and K. E. Gebhardt. "Human and Environmental Toxicity of Sodium Lauryl Sulfate (SLS): Evidence for Safe Use in Household Cleaning Products." *Environmental Health Insights* 9 (2014): 27-32.
- [148] Alanyalıoğlu, M., J. J. Segura, J. Oró-Solè, and N. Casañ-Pastor. "The synthesis of graphene sheets with controlled thickness and order using surfactant-assisted electrochemical processes." *Carbon* 50, no. 1 (2012): 142-152.
- [149] Patil, M. N., and A. B. Pandit. "Cavitation—a novel technique for making stable nano-suspensions." *Ultrasonics Sonochemistry* 14, no. 5 (2007): 519-530.
- [150] Lorimer, J. P., and T. J. Mason. "Sonochemistry. Part 1—the physical aspects." *Chemical Society Reviews* 16 (1987): 239-274.
- [151] Pérez, E. M., and N. Martín. " π - π interactions in carbon nanostructures." *Chemical Society Reviews* 44, no. 18 (2015): 6425-6433.
- [152] Fewster, P. F. "X-ray analysis of thin films and multilayers." *Reports on Progress in Physics* 59, no. 11 (1996): 1339.
- [153] Li, D., F. Tian, B. Chu, D. Duan, X. Sha, Y. Lv, H. Zhang, N. Lu, B. Liu, and T. Cui. "Ab initio structure determination of n-diamond." *Scientific Reports* 5 (2015): 13447.

- [154] Ferrari, A. C., J. C. Meyer, V. Scardaci, C. Casiraghi, M. Lazzeri, F. Mauri, S. Piscanec, D. Jiang, K. S. Novoselov, S. Roth, and A. K. Geim. "Raman spectrum of graphene and graphene layers." *Physical review letters* 97, no. 18 (2006): 187401.
- [155] Childres, I., L. A. Jauregui, W. Park, H. Cao, and Y. P. Chen. "Raman spectroscopy of graphene and related materials." *New developments in photon and materials research* 1 (2013).
- [156] Costa, S., E. Borowiak-Palen, M. Kruszynska, A. Bachmatiuk, and R. J. Kalenczuk. "Characterization of carbon nanotubes by Raman spectroscopy." *Materials Science-Poland* 26, no. 2 (2008): 433-441.
- [157] Ma, Q., D. Wang, M. Wu, T. Zhao, Y. Yoneyama, and N. Tsubaki. "Effect of catalytic site position: Nickel nanocatalyst selectively loaded inside or outside carbon nanotubes for methane dry reforming." *Fuel* 108 (2013): 430-438.
- [158] Bradford, M. C. J., and M. A. Vannice. "CO₂ reforming of CH₄." *Catalysis Reviews* 41, no. 1 (1999): 1-42.
- [159] Su, M., J. Wang, H. Du, P. Yao, Y. Zheng, and X. Li. "Characterization and humidity sensitivity of electrospun ZrO₂: TiO₂ hetero-nanofibers with double jets." *Sensors and Actuators B: Chemical* 161, no. 1 (2012): 1038-1045.
- [160] Li, D., Y. Wang, and Y. Xia. "Electrospinning of polymeric and ceramic nanofibers as uniaxially aligned arrays." *Nano letters*, 3(8) (2003): 1167-1171.
- [161] Ding, B., M. Wang, J. Yu, and G. Sun. "Gas sensors based on electrospun nanofibers." *Sensors* 9, no. 3 (2009): 1609-1624.
- [162] Sill, T. J., and H. A. von Recum. "Electrospinning: applications in drug delivery and tissue engineering." *Biomaterials* 29, no. 13 (2008): 1989-2006.
- [163] Wang, X., C. Drew, S. H. Lee, K. J. Senecal, J. Kumar, and L. A. Samuelson. "Electrospun nanofibrous membranes for highly sensitive optical sensors." *Nano letters* 2, no. 11 (2002): 1273-1275.
- [164] Wang, C., L. Yin, L. Zhang, D. Xiang, and R. Gao. "Metal oxide gas sensors: sensitivity and influencing factors." *Sensors* 10, no. 3 (2010): 2088-2106.
- [165] Lowell, S., J. E. Shields, M. A. Thomas, and M. Thommes. "Characterization of porous solids and powders: surface area, pore size and density." Vol. 16. Springer Science & Business Media, 2012.
- [166] Huang, J., and Q. Wan. "Gas sensors based on semiconducting metal oxide one-dimensional nanostructures." *Sensors* 9, no. 12 (2009): 9903-9924.
- [167] Korotcenkov, G. "Metal oxides for solid-state gas sensors: What determines our choice?" *Materials Science and Engineering: B* 139, no. 1 (2007): 1-23.

- [168] Aronniemi, M., J. Saino, and J. Lahtinen. "Characterization and gas-sensing behavior of an iron oxide thin film prepared by atomic layer deposition." *Thin Solid Films* 516, no. 18 (2008): 6110-6115.
- [169] Suri, K., S. Annapoorni, A. K. Sarkar, and R. P. Tandon. "Gas and humidity sensors based on iron oxide–polypyrrole nanocomposites." *Sensors and Actuators B: Chemical* 81, no. 2-3 (2002): 277-282.
- [170] Yang, X., Y. Liu, J. Li, and X. Zhang. "Influence of thermal decomposition on morphologies and magnetic properties of iron nanofibres via electrospinning." *Micro & Nano Letters* 6, no. 11 (2011): 967-970.
- [171] Mousavi, S., K. Kang, J. Park, and I. Park. "Polyaniline-polystyrene nanofibers directly written on cheap flexible substrates by electrospinning, a low-cost and sensitive hydrogen sulfide gas sensor." In *Micro Electro Mechanical Systems (MEMS), 2016 IEEE 29th International Conference on*, pp. 917-919. IEEE, 2016.
- [172] Groden, N., W. Clower, and C. G. Wilson. "Electrospun Iron-Based Fibers for Use in MEMS Sensors." *Journal of Microelectromechanical Systems* 26, no. 5 (2017): 987-989.
- [173] Virji, S., J. Huang, R. B. Kaner, and B. H. Weiller. "Polyaniline nanofiber gas sensors: examination of response mechanisms." *Nano letters* 4, no. 3 (2004): 491-496.
- [174] Tudoract, F., and M. Grtgora. "Study of polyaniline-iron oxides composites using for gas detection." *Optoelectron. Adv. Mater.* 4 (2010): 43-47.
- [175] Wu, Z., X. Chen, S. Zhu, Z. Zhou, Y. Yao, W. Quan, and B. Liu. "Room temperature methane sensor based on graphene nanosheets/polyaniline nanocomposite thin film." *IEEE Sensors Journal* 13, no. 2 (2013): 777-782.